

**MICROSTRUCTURAL ANALYSIS OF LINEAR FRICTION
WELDED JOINT IN NICKEL-BASE INCONEL 738
SUPERALLOY**

By

OYEDELE TEMITOPE OLA

A thesis submitted to the Faculty of Graduate Studies of

The University of Manitoba

in partial fulfillment of the requirements for the degree of

Master of Science

Department of Mechanical and Manufacturing Engineering

University of Manitoba

Winnipeg

Copyright © December 2010 by Oyedele Temitope Ola

Acknowledgement

I appreciate my supervisor, Dr. M.C. Chaturvedi, for giving me an opportunity to work on this attractive project and for making all necessary research facilities available for me. I am grateful for his contributions to the success of the research. I sincerely thank my co-supervisor, Dr. O.A. Ojo, for coaching and guiding me all the way. I am grateful to him for his timely advice, continual intellectual support and close supervision. I recognize the contributions and technical advice of Dr. R.K. Sidhu.

I am grateful to the University of Manitoba for the Award of the University of Manitoba Graduate Fellowship and to NSERC for their financial support. I thank Dr. Priti Wanjara for making the Linear Friction Welding facilities available to me and for contributing to the project. I acknowledge the expertise of M. Guérin and E. Dalgaard of the Aerospace Manufacturing Technology Centre of The Institute for Aerospace Research, National Research Council (NRC), Montréal, Canada. I am grateful to Don Mardis, Mike Boswick and John Vandorp for their technical assistance. I thank Dr. K. Vishwakarma for her assistance. I also thank Elenor Friesen. I thank my colleagues – Richard Buckson, Lawrence Osoba, Jinal Sanghvi, and Jonathan Dohie. I appreciate my friends – Dr and Dr Mrs Opapeju, Mr and Mrs Adegunju, Tolulope Sajobi, Dr. and Mrs. Seun Idowu, Dr. and Mrs. Dotun Akinlade, Seyi Idowu, Dr. Damola Adedapo and his family, Mr. and Mrs. Akinbola George.

I appreciate my dad and mum for giving me the right parenthood at the right times of my life. I thank my siblings – Oyewole, Oyefunke and Oyekunle Ola, for understanding why I had to depart from them when I did. I appreciate my daughter, Inioluwa, for her understanding and patience with me throughout my studies. I express my profound

gratitude to my wife, Olaitan (my jewel), for her love and support. I give the entire honor to the giver of life, the Almighty God, for wisdom, knowledge and understanding.

Abstract

Inconel 738 (IN 738), like other precipitation-hardened nickel-base superalloys that contain a substantial amount of Al and Ti, is very difficult to weld due to its high susceptibility to heat-affected zone (HAZ) cracking during conventional fusion welding processes. The cause of this cracking, which is usually intergranular in nature, has been attributed to the liquation of various phases in the alloy, subsequent wetting of the grain boundaries by the liquid and decohesion along one of the solid-liquid interfaces due to on-cooling tensile stresses. To address the problem of liquation cracking in weldments, recent developments in welding research have resulted in supposedly exclusive solid-state friction joining processes, such as linear friction welding (LFW), for joining crack susceptible structural alloys. The objective of this work was therefore to investigate the weldability of the difficult-to-weld IN 738 superalloy by LFW and to analyze the resulting microstructural changes in the alloy due to the welding process.

LFW was performed on Linear Friction Welding Process Development System (PDS) at the Aerospace Manufacturing Technology Centre of the Institute for Aerospace Research, National Research Council (NRC) of Canada. In order to study and decouple the effect of non-equilibrium thermal cycle and imposed compressive stress during the joining, physical simulation of the LFW process was performed by using Gleeble 1500-D Thermo-Mechanical Simulation System at the University of Manitoba. Detailed microstructural study of welded and Gleeble-simulated materials was carried out. Correlation between the simulated microstructure and that of the weldments was obtained, in that, a significant grain boundary liquation was observed in both the simulated specimens and actual weldments due to non-equilibrium reaction of second

phase particles, including the strengthening gamma prime phase. These results show that in contrast to the general assumption of LFW being an exclusively solid-state joining process, intergranular liquation, caused by non-equilibrium phase reaction(s), occurred during the process. However, despite a significant occurrence of liquation in the alloy, no HAZ cracking was observed. Nevertheless, the result showed that crack-free welding by linear friction welding is not due to preclusion of grain boundary liquation as has been commonly assumed and reported. Instead, resistance to cracking can be related to the counter-crack-formation effect of the imposed strain and to a concept observed and reported for the first time in this work, which is strain-induced rapid solidification. Furthermore, microstructural evolution during joining cannot be understood without considering the concept of non-equilibrium liquation reaction and strain-induced rapid solidification of the metastable liquid, which are carefully elucidated in this thesis.

Table of Contents

Acknowledgement	ii
Abstract.....	iv
Table of Contents	vi
List of Figures.....	ix
List of Tables.....	xiii
Copyright Permissions.....	xiv
Chapter 1.....	1
Chapter 2.....	4
2.1 Introduction	4
2.2 Physical Metallurgy of IN 738	4
2.2.1 Alloying Elements and their Effects on Microstructure.....	5
2.2.2 Microstructure of the Cast Alloy.....	7
2.2.2.1 The Gamma (γ) Matrix.....	7
2.2.2.2 The Gamma Prime (γ') phase.....	8
2.2.2.3 Gamma-Gamma Prime (γ - γ') Eutectic.....	10
2.2.2.4 Carbides.....	10
2.2.2.5 Borides and Sulphocarbides	12
2.3 Welding Processes.....	13
2.3.1 Conventional Fusion Welding Techniques	13
2.3.1.1 Oxyacetylene welding.....	15
2.3.1.2 Arc Welding Processes.....	15
2.3.1.3 Electron Beam Welding	19
2.3.1.4 Laser Beam Welding.....	21
2.4 On-Cooling Tensile Stresses in HAZ of Fusion Welds	23

2.5 Weld Defects Associated with Fusion Welding Processes	25
2.6 Cracking During Fusion Welding Processes.....	27
2.6.1 Solidification Cracking	27
2.6.1.1. Factors Affecting Solidification Cracking Susceptibility	29
2.6.1.2. Mechanism of Solidification cracking	31
2.6.2 Heat-Affected Zone Liquation Cracking.....	31
2.6.2.1 Constitutional Liquation.....	34
2.6.2.1.1 Constitutional Liquation Theory	35
2.6.2.1.1 Constitutional Liquation of Phases in IN 738	40
2.6.2.2 Grain boundary Segregation.....	40
2.7 A More Recent Development – Friction Welding	42
2.7.1 The Development of Friction Welding Processes.....	44
2.8 Friction Welding Processes.....	45
2.8.1 Inertia Friction Welding.....	45
2.8.2 Continuous-Drive Friction Welding.....	49
2.8.3 Linear Friction Welding.....	54
2.8.4 Friction Stir Welding.....	59
2.9 Attractiveness of Friction Welding Processes.....	62
2.10 Scope and Objectives of the Present Study.....	65
Chapter 3.....	67
3.1 Materials Preparation	67
3.2 Linear Friction Welding (LFW) of IN 738	69
3.3 Gleeble Thermomechanical Simulations	69
3.4 Micro-hardness Measurement.....	70
3.5 Microscopy.....	70

Chapter 4.....	72
4.1 General Microstructural Analysis of Pre-Weld and Linear Friction Welded Specimens.....	72
4.1.1 Introduction.....	72
4.1.2 Pre-weld Microstructure.....	72
4.1.3 Microstructure of the Welded Material.....	74
4.1.3.1 Weld Zone (WZ) Microstructure.....	74
4.1.3.2 Thermo-mechanically Affected Zone (TMAZ) Microstructure.....	78
4.1.3.3 Heat Affected Zone (HAZ) Microstructure.....	81
4.1.4 Intergranular and Intragranular Liquation in the Welded Material.....	85
4.2 Gamma Prime (γ') Precipitate Dissolution Behaviour.....	88
4.2.1. Introduction.....	88
4.2.2 Non-Equilibrium γ' Particle Dissolution under Rapid Thermal Cycle.....	89
4.2.3 Strain-Assisted Dissolution of γ' Precipitates.....	95
4.3 Preclusion of Intergranular Liquation Cracking.....	105
4.3.1 The Counter-Crack-Formation Effect of the Imposed Compressive Stress...	105
4.3.2 Strain-Induced Rapid Solidification and Enhanced Resistance to Cracking .	108
4.3.3 Comparison of Hot Ductility Behaviour under Compression and Tension ...	122
4.4 Other Weld Microstructural Characteristics.....	124
Chapter 5.....	139
Chapter 6.....	141
References	142

List of Figures

Figure 2 - 1: Unit cell illustrating $L1_2$ ordered FCC lattice of γ' phase.....	9
Figure 2 - 2: Chronological development of welding processes and their applications. ..	14
Figure 2 - 3: Oxyacetylene welding: a) overall process, b) welding area enlarged	16
Figure 2 - 4: Gas Tungsten Arc Welding: a) overall process, b) welding area enlarged ..	18
Figure 2 - 5: Electron Beam Welding: a) process; b) keyhole	20
Figure 2 - 6: Laser beam welding with solid-state laser: a) process, b) energy absorption and emission during laser action	22
Figure 2 - 7: Schematic representation of changes in temperature and stresses during welding: (a) Weld (b) Temperature changes (c) Stress distribution	24
Figure 2 - 8: Typical arc welding defects.....	28
Figure 2 - 9: Schematic illustration of the mechanism of solidification cracking.	32
Figure 2 - 10: Schematic diagram illustrating liquation cracking.....	33
Figure 2 - 11: Schematic diagram of a portion of a hypothetical constitutional diagram for an alloy system exhibiting the behaviour necessary for constitutional liquation.....	36
Figure 2 - 12: Schematic representation of the concentration gradients at various temperatures during formation of constitutional liquation.....	38
Figure 2 - 13: Some characteristics of flywheel friction welding process	46
Figure 2 - 14: A schematic of an inertia welder	47
Figure 2 - 15: Layout of continuous drive friction welding.....	50
Figure 2 - 16: The variation of speed, torque, force and axial shortening during the welding cycle.....	52
Figure 2 - 17: Basic principle of linear friction welding.....	56
Figure 2 - 18: The four phases that characterize linear friction welding	57
Figure 2 - 19: Metallurgical Processing Zones Developed During Friction Stir Joining.	61

Figure 4 - 1: SEM micrograph of solution heat treated IN 738 showing primary and secondary γ' precipitates, MC Carbides and γ - γ' eutectic	73
Figure 4 - 2: Optical micrograph of the linear friction welded joint.....	75
Figure 4 - 3: SEM micrograph of the linear friction welded joint	76
Figure 4 - 4: Optical micrograph showing an overview of three regions characterizing the joint microstructure	77
Figure 4 - 5: Higher magnification SEM micrograph of the weld zone, region 1	79
Figure 4 - 6: Optical micrograph showing recrystallization across the joint	80
Figure 4 - 7: Auger SEM micrograph taken around 300 μ m to the weld line.....	82
Figure 4 - 8: Micro-hardness values across the welded joint, which are average of values within a distance of 0 to 0.9 mm, 1.0 to 1.9 mm and 4.0 to 4.9 mm from the weld line. The region within the 4.0 to 4.9 mm was the base material.....	83
Figure 4 - 9: SEM micrograph of HAZ, region 3.....	84
Figure 4 - 10: SEM micrograph showing liquation along grain boundaries of the linear friction welded material	86
Figure 4 - 11: SEM micrograph of the TMAZ showing intragranular liquation	87
Figure 4 - 12: γ' precipitate dissolution under rapid thermal cycle (heating rate of 150 ⁰ C/sec): 0.5sec holding time at peak temperatures of (a) 1170 ⁰ C, (b) 1200 ⁰ C and (c) 1250 ⁰ C, and (d) 1.5sec holding time at 1170 ⁰ C (e) 3.5sec holding time at 1170 ⁰ C, followed by air cooling	91
Figure 4 - 13: SEM micrographs showing grain boundary liquation in Gleeble-simulated specimens heated at 150 ⁰ C/sec and held for 0.5sec at (a) 1170 ⁰ C (b) 1200 ⁰ C and (c) 1180 ⁰ C (cast material), followed by air cooling.....	94
Figure 4 - 14: Specimens heated to 1110 ⁰ C at 150 ⁰ C/s and held for 20.5 seconds, followed by air cooling, (a) thermal cycle alone, (b) strained to 20% length reduction at peak temperature	100
Figure 4 - 15: Gleeble-simulated specimens heated to 1150 ⁰ C at 150 ⁰ C/s and held for 10.5 seconds, followed by air cooling, (a) thermal cycle alone, (b) strained to 20% length reduction at peak temperature	101
Figure 4 - 16: Gleeble-simulated specimens heated to 1170 ⁰ C at 150 ⁰ C/s and held for 1.5 seconds, followed by air cooling, (a) thermal cycle alone, (b) strained to 20% length reduction at peak temperature	102

Figure 4 - 17: Gleeble-simulated specimens heated to 1170 ⁰ C at 150 ⁰ C/s and held for 3.5 seconds, followed by air cooling, (a) thermal cycle alone, (b) strained to 20% length reduction at peak temperature	104
Figure 4 - 18: Optical micrograph of the extruded flash material, with an inset showing cracks in the material where tensile stresses are present.....	107
Figure 4 - 19: Gleeble simulated materials heated at 150 ⁰ C/sec and held for 2.5 sec at 1230 ⁰ C followed by air cooling; showing (a) intragranular resolidified products under thermal cycle alone (b) absence of resolidified products when 25% length reduction was imposed	110
Figure 4 - 20: Gleeble simulated materials heated at 150 ⁰ C/sec and held for 10.5 sec at 1230 ⁰ C followed by air cooling; showing (a) intragranular resolidified products under thermal cycle alone (b) absence of resolidified products when 25% length reduction was imposed	112
Figure 4 - 21: Gleeble-simulated specimens heated at 150 ⁰ C/sec to 1230 ⁰ C, held for 0.5sec and air-cooled, showing (a) intragranular resolidified products and (b) liquated eutectic area and liquated grain boundary.....	113
Figure 4 - 22: Schematic diagram showing liquid film between two grains of different orientation-dependent elastic modulus, Y, and the corresponding free energy curves...	117
Figure 4 - 23: Liquid film migration (LFM) in Gleeble-simulated specimens heated at 150 ⁰ C/sec and held at 1170 ⁰ C for 1.5sec, followed by air cooling – thermal cycle alone	118
Figure 4 - 24: Figure 4.21: Liquid film migration (LFM) in Gleeble-simulated specimens heated at 150 ⁰ C/sec and held at 1170 ⁰ C for 1.5sec, followed by air cooling – strained to 20% length reduction at peak temperature	119
Figure 4 - 25: Weld zone microstructure	127
Figure 4 - 26: Gleeble-simulated materials heated at 150 ⁰ C/sec to 1230 ⁰ C, held for 0.5sec, strained to 25% length reduction in 10sec and air-cooled, showing boundary-like features (a) lower magnification (b) higher magnification.	128
Figure 4 - 27: Gleeble-simulated materials heated at 150 ⁰ C/sec to the peak temperature of 1200 ⁰ C and held for (a) 3.5sec (b) 10.5sec, followed by air cooling.....	130
Figure 4 - 28: Optical micrograph showing recrystallization in the weld zone	133
Figure 4 - 29: OIM images showing (a) the distribution of unique recrystallized grains across the weld centerline, and (b) the character of the recrystallized grains.....	135

Figure 4 - 30: OIM images showing (a) the distribution of unique recrystallized grains at the transition region between the weld zone and TMAZ, and (b) the character of the recrystallized grains at the transition region 136

List of Tables

Table 2 - 1: Nominal composition of cast IN 738C and IN 738LC	6
Table 2 - 2: Materials combinations that can be joined by inertia welding	63
Table 3 - 1: Nominal composition of cast IN 738LC used in this study.....	68

Copyright Permissions

Figure 2-2: Source – Encyclopedia of Materials Science and Engineering. Reprinted with permission from Elsevier (17 November, 2010) and the Author (30 November, 2010).

Figure 2-3: Source – “Welding Metallurgy” (2nd Ed) by Sindo Kuo. Reprinted with permission from Global Rights Department, John Wiley & Sons, Inc. (2 December, 2010)

Figure 2-4: Source – “Welding Metallurgy” (2nd Ed) by Sindo Kuo. Reprinted with permission from Global Rights Department, John Wiley & Sons, Inc. (2 December, 2010)

Figure 2-5: Source – “Welding Metallurgy” (2nd Ed) by Sindo Kuo. Reprinted with permission from Global Rights Department, John Wiley & Sons, Inc. (2 December, 2010)

Figure 2-6: Source – “Welding Metallurgy” (2nd Ed) by Sindo Kuo. Reprinted with permission from Global Rights Department, John Wiley & Sons, Inc. (2 December, 2010)

Figure 2-7: Source – “Analysis of Welded Structures” by K. Masubuchi. Reprinted with permission from Elsevier (29 November, 2010) and the Author (30 November, 2010).

Figure 2-9: Source – Philosophical Transactions of the Royal Society of London. Reprinted with permission from The Royal Society (22 November, 2010).

Figure 2-10: Source – Philosophical Transactions of the Royal Society of London. Reprinted with permission from The Royal Society (22 November, 2010).

Figure 2-11: Source – Welding Journal. Reprinted with permission.

Figure 2-12: Source – Welding Journal. Reprinted with permission.

Figure 2-13: Source – Welding Journal. Reprinted with permission.

Figure 2-14: Source – “Inertia Friction Welding”. Reprinted with permission. Courtesy of Manufacturing Technology, Inc. (15 December, 2010)

Figure 2-15: Source – Journal of Materials Processing Technology. Reprinted from M. Sahin, J. Mater. Processing Technol., Vols. 153-154, 2004, p.1011, with permission from Elsevier (25 November, 2010).

Figure 2-16: Source – Wear. Reprinted from F. Duffin and A.S. Bahrani, Wear, Vol 26, 1973, p.53, with permission from Elsevier (8 December, 2010)

Figure 2-18: Source – Materials Science and Engineering A. Reprinted from A. Vairis and M. Frost, Mater. Sci. Eng. A, Vol. 217, 1999, p.477, with permission from Elsevier (29 November, 2010).

Figure 2-19: Source – Hot Deformation of Aluminum Alloys III. Reprinted with permission from The Minerals, Metals and Materials Society (1 December, 2010).

Chapter 1

Introduction

Superalloys were, and continue to be, developed for elevated temperature service. They are utilized at a higher proportion of their actual melting point than any other class of broadly commercial metallic material. They are divided into three classes, namely nickel-base superalloys, cobalt-base superalloys and iron-base superalloys. Superalloys have found applications in aircraft, marine and industrial gas turbines, as well as in rocket engines, nuclear reactors and petrochemical equipments [1]. Inconel 738 is a nickel-base superalloy with a significant volume fraction of an ordered intermetallic $\text{Ni}_3(\text{Al,Ti})$, γ' , phase and it possesses an excellent high-temperature strength and remarkable corrosion resistance. This makes it useful in the production of hot-section components in aero and land-based gas turbine applications.

The service environment for IN 738 components in turbines is extremely hostile and results in a rapid degradation and damage of components. Apart from the challenges of degradation and damage, process efficiency and cost consideration require that manufacturing companies deploy the best techniques for the fabrication of components in order to gain an advantage position over competitors. Two alternatives are available to address the degradation and damage situation. The components are either replaced or repaired. However, in economic terms, the cost of replacement is often exorbitant compared to the cost of repair. The competitiveness and profitability drive within the aerospace and power industries necessitate the achievement of both fabrication and repair of these components at the minimum possible cost without necessarily jeopardizing the required quality. Therefore, the repair of damaged components is more economically

justifiable over replacement. Fabrication and repair of service components often involve various joining methods.

Welding has proven to be an economical way of fabricating components and repairing service-damaged turbine parts. Unfortunately, IN 738, like other precipitation-hardened nickel-base superalloys that contain a substantial amount of Al and Ti, is very difficult to weld due to its high susceptibility to heat-affected zone (HAZ) cracking during conventional fusion welding processes and strain age cracking during post-weld heat treatment (PWHT) [2]. The cause of this cracking, which is usually intergranular in nature, has been attributed to the liquation of various phases in the alloy, subsequent wetting of the grain boundaries by the liquid and de-cohesion along one of the solid-liquid interfaces due to on-cooling tensile stresses. This mechanism of cracking is usually referred to as heat-affected zone (HAZ) grain boundary liquation cracking.

In order to avoid liquation and liquation cracking in superalloys, the state-of-the-art trend in joining difficult-to-weld structural materials involves the use of solid-state joining techniques. The main drive is that the avoidance of heat-affected zone (HAZ) grain boundary liquation cracking will be possible if a major necessary condition, which is grain boundary liquation, can be completely eliminated. Friction welding has been regarded as a solid-state joining process that has great potentials in the aerospace industry for the joining of superalloys, especially for the fabrication of blade-disk assembly and the repair of aero-engine parts. The process has produced successful joints in some structural alloys and current research efforts are now being geared towards its application for the fabrication and repair of turbine parts made of nickel-base superalloys. The present work was initiated in order to investigate the weldability of the difficult-to-weld

IN 738 superalloy by a variant of the friction welding processes (linear friction welding) and to analyze the resulting microstructural changes in the alloy due to the welding process. The results of the study are presented and discussed in chapter 4 of this thesis, which is preceded by a review of relevant and background literature in chapter 2 and the description of various research techniques used in chapter 3.

Chapter 2

Literature Review

2.1 Introduction

In this chapter, a brief overview of the physical metallurgy of IN 738 is presented first, followed by the various conventional joining techniques and the associated joining-related problems. Solid-state friction welding techniques are subsequently presented as the state-of-the-art to address a major problem usually encountered during conventional welding processes. The reasons for the attractiveness of joining nickel-base superalloys by friction welding methods are identified. This review of literature is followed by the scope and objectives of the present study.

2.2 Physical Metallurgy of IN 738

IN 738 is a remarkable nickel-base superalloy, which is both solid solution and precipitation strengthened, and usually selected for applications that require good high temperature mechanical, corrosion and oxidation properties. It has a face-centered cubic (fcc) austenitic solid-solution as the matrix with an intermetallic compound phase, usually known as gamma prime (γ') particles [3]. The alloy was designed to combine the strength of IN 713C, which possess an excellent high temperature strength, with the oxidation and sulfidation resistance of Udimet 500. Like IN 713C, IN 738 also derives its high temperature strength mainly from the precipitation of the ordered $L1_2$ intermetallic $Ni_3(Al, Ti)$, γ' , phase. Its excellent corrosion and creep resistance allow it to be used at temperatures up to approximately $980^{\circ}C$. Two different types of the alloy exist in the cast form depending on the carbon content. The low carbon version ($C \approx 0.09 - 0.13$ wt%) is designated as IN 738LC which also has a lower Zr content to improve the alloy's

castability in large sections, while the high carbon ($C \approx 0.15 - 0.20\text{wt}\%$) is designated as IN 738C [4].

IN 738 is vacuum melted and investment cast as developed at the Paul D. Merica research laboratory [5]. To partially eliminate the microporosity formed during ingot solidification and its detrimental effect, hot isostatic pressure (HIP), which usually involves the application of isostatic pressure, is usually applied to the cast alloy in an argon atmosphere at high temperature. After casting, the alloy is usually subjected to a standard solution heat treatment (SHT) at 1120°C for 2hrs, air-cooled, followed by a standard aging treatment at 845°C for 24hrs, then air-cooled. The alloying elements and their compositions in IN 738 play significant roles in the alloy's microstructure and strength. The alloying elements and their effects on the microstructure of IN 738 will be discussed next.

2.2.1 Alloying Elements and their Effects on Microstructure

The nominal compositions of both IN 738LC and IN 738C are given in table 2.1 [4]. The atomic diameter of nickel is about 0.2491 nm [6] and the diameters of the alloying elements differ from this by about 0 to 18%, with the atomic diameter of niobium being the highest (18%). Co, Cr, Fe, Mo, W and Ta are solid solution strengtheners, W, Ta, Ti, Mo, Nb and Cr are carbide formers and Al and Ti are the main formers of the $\text{Ni}_3(\text{Al}, \text{Ti})$, γ' , phase. Co raises the solvus temperature of γ' while Cr lowers it and the addition of Al, Cr and Ta provides resistance to high temperature oxidation. Enhancement of creep rupture properties is achieved by the presence of B and Zr [3]. Apart from the γ' phase in IN 738, several second phase particles are also present in the alloy as a result of its multi-component nature and the metallurgical reactions that are possible in the alloy, depending

Table 2 - 1: Nominal composition of cast IN 738C and IN 738LC

Element	IN 738C (wt%)	IN 738LC (wt%)
Carbon	0.17	0.11
Cobalt	8.5	8.5
Chromium	16.00	16.00
Molybdenum	1.75	1.75
Tungsten	2.60	2.60
Tantalum	1.75	1.75
Niobium	0.90	0.90
Aluminum	3.40	3.40
Titanium	3.40	3.40
Boron	0.01	0.01
Zirconium	0.1	0.05
Iron	LAP*	LAP*
Manganese	LAP	LAP
Silicon	LAP	LAP
Sulphur	LAP	LAP
Nickel	Balance (61)	Balance (61)

*Low as possible

on the processing route and the actual composition [7]. Such phases include carbides, sulphocarbides and borides, and other solidification products [8]. The microstructure of the cast alloy will be discussed next.

2.2.2 Microstructure of the Cast Alloy

Cast IN 738 consists of: the gamma (γ) matrix, the gamma prime (γ') phase, carbides, sulphocarbides and borides, and other solidification products.

2.2.2.1 The Gamma (γ) Matrix

The γ phase is a continuous matrix of nickel-base austenite [6]. It has an fcc crystal structure [9] and contains a significant amount of solid-solution elements such as Co, Cr, Mo, W, Al and Ti, which differ from Ni by 1 – 18% and normally occupy substitutional atomic positions in Ni crystal producing a distorted lattice with spherical symmetrical strain field. This strain field can interact with the strain field around a dislocation, producing an elastic dislocation-solute atom interaction and provide solid-solution strengthening. Al, in addition to being a precipitation strengthener, is a potential solid-solution strengthener. W, Mo and Cr also are strong solid-solution strengtheners. Above $0.6T_m$ (T_m is the melting temperature of the alloy in Kelvin scale), which is the range of high temperature creep, creep strength is diffusion dependent and the slow-diffusing elements Mo and W are the most beneficial for reducing high-temperature creep. Also, Co, by decreasing stacking fault energy of nickel, which causes dissociation of dislocations into partial dislocations, makes cross-slip more difficult and thereby increases high-temperature stability [6]. The matrix has a high endurance for severe temperatures as a result of the high tolerance of nickel for alloying without phase instability owing to its nearly filled third electron shell [10]. Depending on Cr additions,

Cr in the γ matrix forms Cr_2O_3 -rich protective scales having low cation vacancy content, thereby restricting the diffusion rate of metallic elements outward, and oxygen, nitrogen, sulphur and other aggressive atmospheric elements inward. There is also an additional tendency to form Al_2O_3 -rich scales with exceptional resistance to oxidation [10].

2.2.2.2 The Gamma Prime (γ') phase

The γ' phase is an intermetallic fcc phase having a basic composition $\text{Ni}_3(\text{Al}, \text{Ti})$. It is the principal high-temperature strengthening phase of precipitation-hardened superalloys and it is usually coherent with the austenitic γ matrix. γ' phase generally forms by the reaction of Al and Ti with Ni. It displays the primitive cubic, $L1_2$, crystal structure with Al (and/or Ti) atoms at the cube corners and Ni atoms at the centres of the faces [9]. A typical unit cell of the $L1_2$ crystal structure of the γ' phase is shown in figure 2-1 [11]. Other elements, such as Nb, Ta and Cr, also enter γ' [12]. It has been suggested that the composition of γ' in IN 738 is [13]:



The mismatch between γ and γ' unit cells determines the γ' morphology. γ' occurs as spheres at 0-0.2% lattice mismatch, becomes cubic at mismatches around 0.5-1.0% and then becomes plate shape at mismatches above 1.25%[14]. The γ' phase, which nucleates homogeneously with low surface energy and has extraordinary long-term stability, can be precipitated in the austenitic γ matrix by precipitation hardening heat-treatments [6]. Due to the long range order exhibited by γ' , anti-phase boundary (APB) faults occur generally in γ' -strengthened nickel-base alloys whenever shear strain is applied to the alloy, consequently resulting in APB strengthening by dislocation- γ' precipitate interaction.

⊙ **Nickel**

○ **Aluminum, Titanium, Niobium**

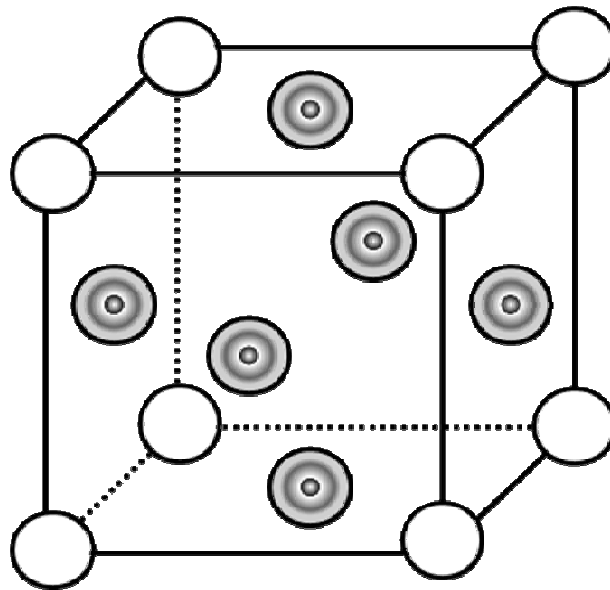


Figure 2 - 1: Unit cell illustrating L1₂ ordered FCC lattice of γ' phase

Also, the degree of order in $\text{Ni}_3(\text{Al}, \text{Ti})$ increases with temperature [6], therefore, IN 738 with a high volume fraction of γ' possesses a higher strength at higher temperatures compared to γ' -lean alloys.

2.2.2.3 Gamma-Gamma Prime (γ - γ') Eutectic

γ - γ' eutectics form as a result of supersaturation of interdendritic liquid with γ' -forming elements, caused by continual solute enrichment, at temperatures approaching the equilibrium solidus. The eutectics mainly consist of γ' phase separated by thin lamellae of γ phase. In IN 738, the temperature of γ - γ' eutectic reaction occurring towards the end of solidification process has been reported to be around 1230°C [15] and 1198°C [16]. Metallographic examination of directionally solidified IN 738 from above the liquidus temperature to different on-cooling temperatures, followed by water quenching, has shown that γ - γ' eutectic reaction in the alloy occurs over a range of temperatures. This has also been observed by others in other nickel-base superalloys [17].

2.2.2.4 Carbides

MC , M_{23}C_6 and M_6C are the common nickel-base alloy carbides [1]. The most common carbide in IN 738 is the MC type carbide. MC carbides usually form during solidification, when the level of carbon concentration is above 0.05% [18], by the reaction of carbon with elements such as Ti, Ta and Nb. They are monocarbides with the general formula “ MC ”, where “ M ” stands for metallic elements such as Ti, Ta, Nb or W [6]. MC carbides usually take a coarse random cubic or irregular morphology. They occur as discrete particles distributed heterogeneously throughout the alloy, both in intergranular and intragranular positions, usually interdendritically, with little or no orientation relationship with the matrix [1]. Primary MC carbides are dense and have fcc crystal structure with

relatively high thermal stability and strength. The chemical formula of MC carbides has been suggested to be: $(\text{Ti}_{.5}\text{Ta}_{.2}\text{Nb}_{.2}\text{W}_{.04}\text{Mo}_{.03}\text{Cr}_{.02})\text{C}$ [13] and their sizes can range from 1 to $100\mu\text{m}$.

During heat treatment and service, MC carbides tend to decompose to produce other carbides such as M_{23}C_6 and/or M_6C through reactions such as: $\text{MC} + \gamma \leftrightarrow \text{M}_{23}\text{C}_6 + \gamma'$ and $\text{MC} + \gamma \leftrightarrow \text{M}_6\text{C} + \gamma'$. In M_{23}C_6 carbides, “M” is usually Cr, but it can be replaced by Fe, and to a smaller extent by W, Mo or Co. They form during lower-temperature heat treatments and during service in the temperature range 760 to 980°C and precipitate on the grain boundaries with a complex cubic structure [6]. They are usually irregular discontinuous blocky particles, although plates and regular geometric forms have been also observed [1]. M_{23}C_6 carbides can also precipitate from soluble carbon residual in the matrix when cast ingot cools through its solvus range ($1000^\circ\text{C} - 1050^\circ\text{C}$). M_6C carbides form at temperatures in the range 815 to 980°C and have a complex cubic structure. They are similar to the M_{23}C_6 carbides and form when the Mo and/or W content are more than 6 to 8 at %.

Grain boundary carbides, when properly formed, have positive influence on the grain boundary properties. A chain of discrete globular M_{23}C_6 carbides optimizes creep rupture life by preventing grain boundary sliding at higher temperatures while concurrently providing sufficient ductility for stress relaxation to occur without premature failure [3]. Contrarily, carbides precipitation as a continuous grain-boundary film severely degrades mechanical properties. Also, carbides can tie up certain elements that would otherwise promote phase instability during service.

2.2.2.5 Borides and Sulphocarbides

Other secondary solidification constituents, apart from MC type carbides and γ - γ' eutectic, found in IN 738 include; borides and sulphocarbides. Borides are hard refractory particles that are observed at grain boundaries but not in the volume with which carbides exist. Boron, generally present to the extent of 50 to 500 ppm, segregates to grain boundaries to form borides. Borides commonly found in superalloys are of the type M_3B_2 , with a tetragonal unit cell [12]. It has been found recently that, under certain heat-treatment conditions, M_5B_3 borides are also formed in superalloys [19]. Though sulphur is usually present in nickel-base superalloys in trace amounts, it has been found to strongly segregate to grain boundaries resulting in severe grain boundary segregation [20-24]. However, the presence of elements such as Ti, Zr, Nb, Hf, and La which have low solubilities in the matrix and high affinity for sulphur has been found to mitigate this effect through the formation of a variety of sulphur-rich intermetallic phases [23] referred to as sulphocarbides.

Hoffelner et al [8], by X-ray diffraction analysis, identified M_3B_2 type borides and M_2SC sulphocarbides in IN 738 after heat treatments. Ojo et al [25] identified some intermetallic phases precipitated very close to γ - γ' eutectic islands during solidification of cast IN 738. These phases, which were first observed by Ojo et al and termed as terminal solidification products, were identified by EDS analysis as Cr-Mo rich particles, Ni-Zr rich particles and Ni-Ti rich particles. TEM diffraction pattern analysis suggested that the Cr-Mo rich particles were M_3B_2 type borides with tetragonal crystal structure. The Ni-Zr rich and Ni-Ti rich particles were suggested to be based on Ni_5Zr and Ni_3Ti respectively.

Egbewande et al [7] also observed the formation of sulphur and carbon rich Ti-Zr-Nb phase close to γ - γ' eutectic, and other terminal solidification constituents.

2.3 Welding Processes

Joining is important in the fabrication and repair of appliances, buildings, machines, automotive and aerospace components/assemblies, and other objects composed of two or more parts joined in some way. Welding processes have been described as processes for joining metals and other materials by applying heat, pressure or both, with or without filler metals to produce a localized union through fusion or recrystallization across the interface [26]. The development of joining technologies dates back to thousands of years ago when copper-gold and lead-tin alloys were being soldered before 3000 BC and iron was being welded into composite tools and weapons as early as 1000 BC. The development of modern welding technologies began in the latter half of the nineteenth century when electricity became readily available, with many of the important discoveries leading to modern welding processes developed between 1880 and 1900. Figure 2-2 [26] lists some chronological developments of welding processes. Welding can be generally classified as fusion welding (which is a conventional joining technique) and solid-state joining processes. The various conventional fusion welding processes will be discussed next.

2.3.1 Conventional Fusion Welding Techniques

Fusion welding is a technique that produces a metallurgical bond/joint between/among components through melting and resolidification of either base alloys of the components to be joined or base alloys plus filler [12]. In cases where a filler material is required, the filler could have either the same nominal composition with the base alloy (assuming the

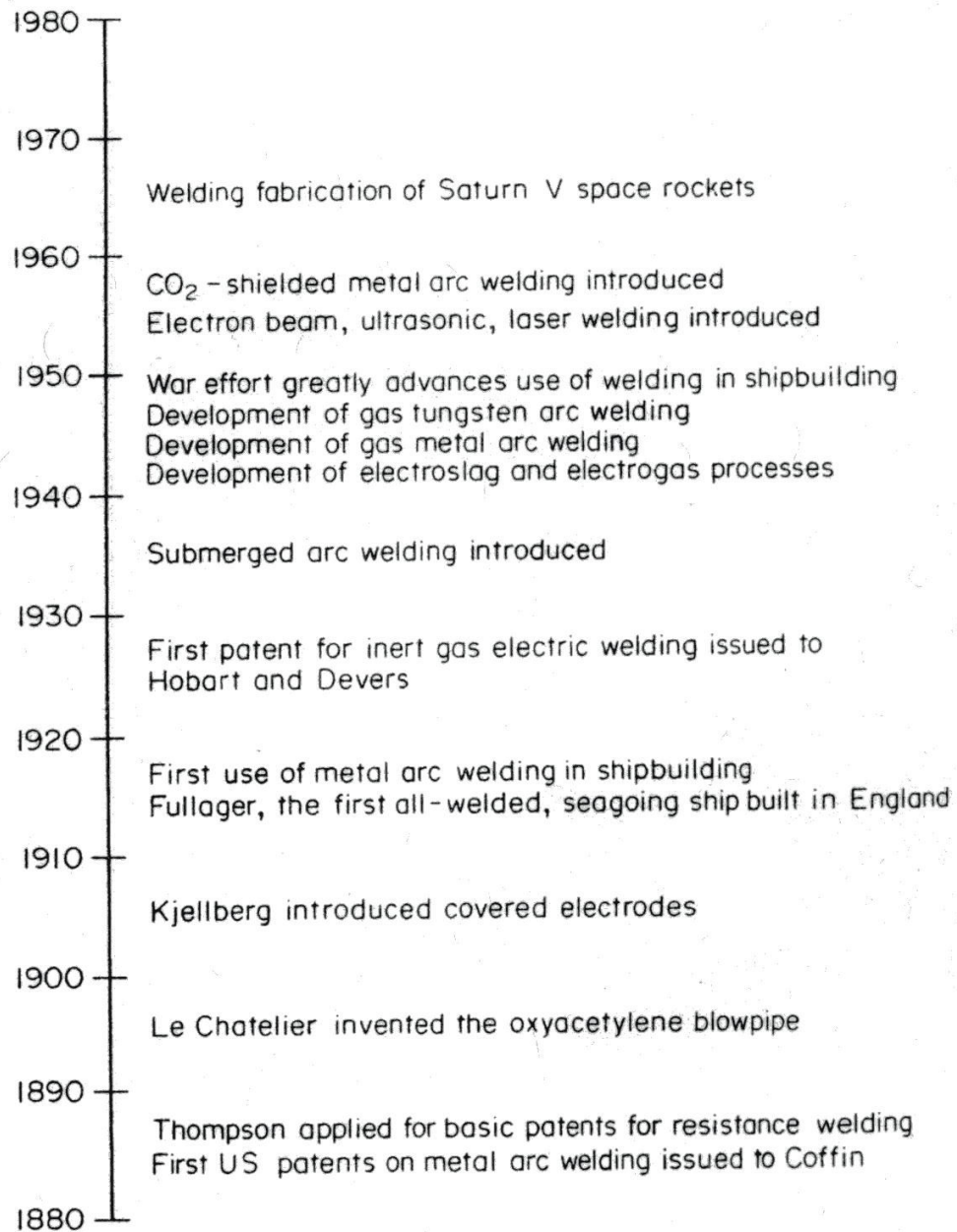


Figure 2 - 2: Chronological development of welding processes and their applications.

Source: Encyclopedia of Materials Science and Engineering [26]. Reprinted with permission from Elsevier (17 November, 2010) and the Author (30 November, 2010).

joining is of components of the same composition) or a composition compatible with the chemistry of the components being joined both environmentally and mechanically. Melting during fusion welding is achieved by the use of a heat source which may be provided by a chemical flame, an arc, a laser or an electron beam. The classification of the various fusion welding processes is based on the type of heat source [27], and these processes are discussed next.

2.3.1.1 Oxyacetylene welding

Oxyacetylene (OAW) welding is a gas welding process that melts and joins metals by heating them with a flame caused by the reaction between a fuel gas and oxygen. It is the most commonly used gas welding process because of its high flame temperature. A schematic diagram of the process is provided in figure 2-3 [28]. The oxyacetylene welding process equipment is simple, portable and inexpensive, making it convenient for maintenance and repair applications. However, the very low welding speed and the rather high total heat input per unit length of the weld result in large heat-affected zones (HAZ) and severe distortion. The oxyacetylene welding process is not recommended for welding reactive metals such as titanium and zirconium because of its limited protection power.

2.3.1.2 Arc Welding Processes

Arc welding uses an arc, struck between an electrode and the workpiece, to generate heat that melts the filler (which could sometimes be the electrode) and the base metal. A molten pool is produced under the protection of an inert gas blanket. The pool solidifies as the heat source retreats from the area, and a solidified weld nugget is formed along with a heat-affected zone (HAZ). The HAZ extends from the interface of the previously molten metal to a distance in the metal being joined where the temperature reached in the

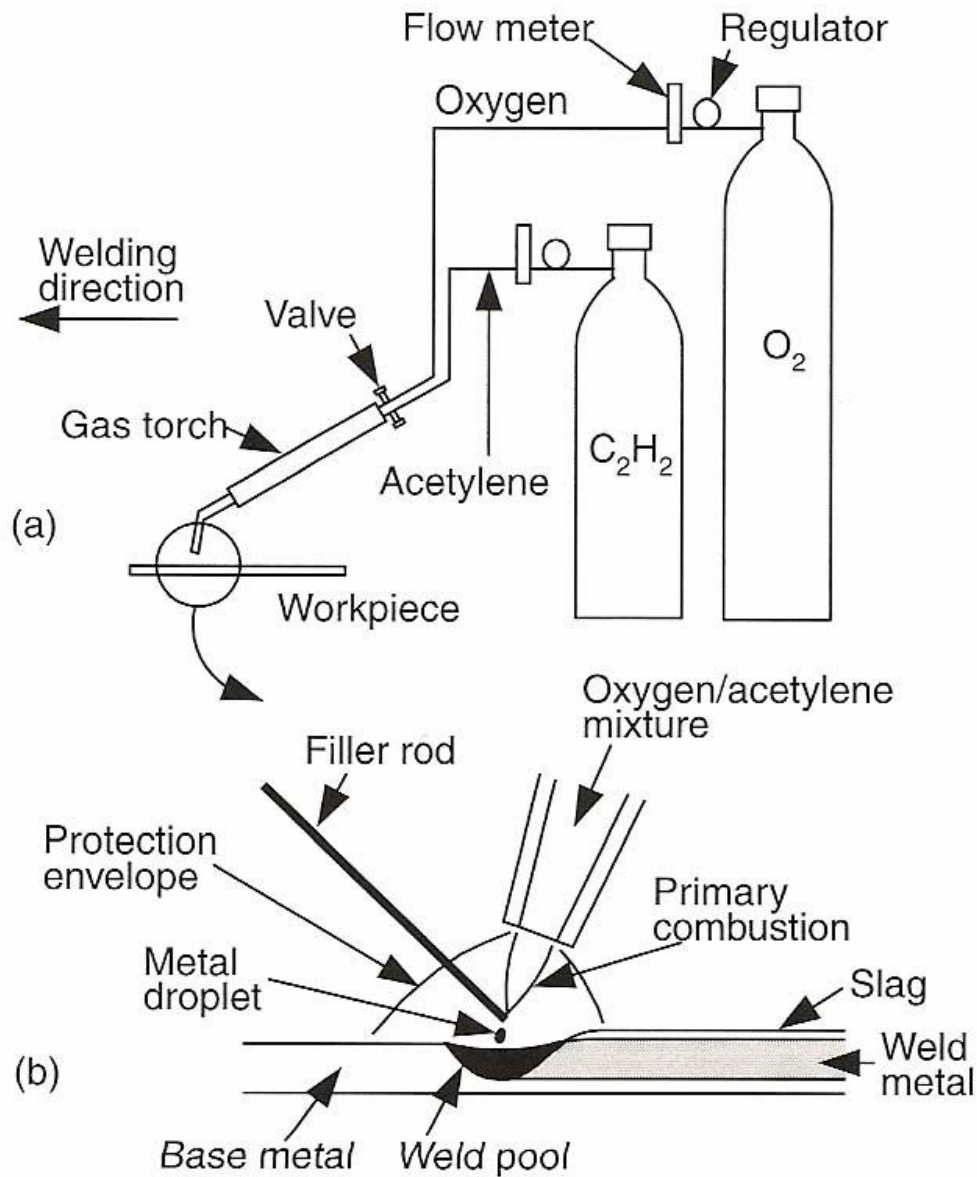


Figure 2 - 3: Oxyacetylene welding: a) overall process, b) welding area enlarged

Source: "Welding Metallurgy" (2nd Ed) by Sindo Kuo [28]. Reprinted with permission from the Global Rights Department, John Wiley & Sons, Inc. (2 December, 2010)

welding process becomes sufficiently low that no metallurgical changes occur. Arc welding processes that can be used to join superalloys include [28]: shielded metal arc welding (SMAW), gas tungsten arc welding (GTAW), plasma arc welding (PAW), gas metal arc welding (GMAW), flux cored arc welding (FCAW), submerged arc welding (SAW), and electroslag welding (ESW).

Gas tungsten arc welding (GTAW), also usually called tungsten inert gas welding (TIG) welding, is the most widely used arc welding process for joining superalloys. In TIG welding, the heat is produced between non-consumable tungsten electrode and the metal workpiece. The electrode, weld pool, arc and adjacent heated work areas of the workpiece are protected from atmospheric contamination by a gaseous shield, which is provided by a stream of gas (usually an inert gas) or a mixture of gases. The torch holding the tungsten electrode is connected to the shielding gas cylinder as well as one terminal of the power source, with the tungsten electrode in contact with a water-cooled copper tube. A schematic diagram of the process is provided in figure 2-4 [28]. TIG welding is an all-position process and is especially well-adapted to the welding of thin metals, often as thin as 0.15mm (0.005in). A number of nickel-base superalloys are readily weldable by TIG [3]. Unlike the oxyacetylene welding process, TIG is a very clean welding process that can be used to weld reactive metals such as titanium and zirconium, aluminum and magnesium. However, the deposition rate is low and excessive welding currents can cause melting of the tungsten electrode and result in brittle tungsten inclusions in the weld metal. Pre-heated filler metals can be used to improve the deposition rate.

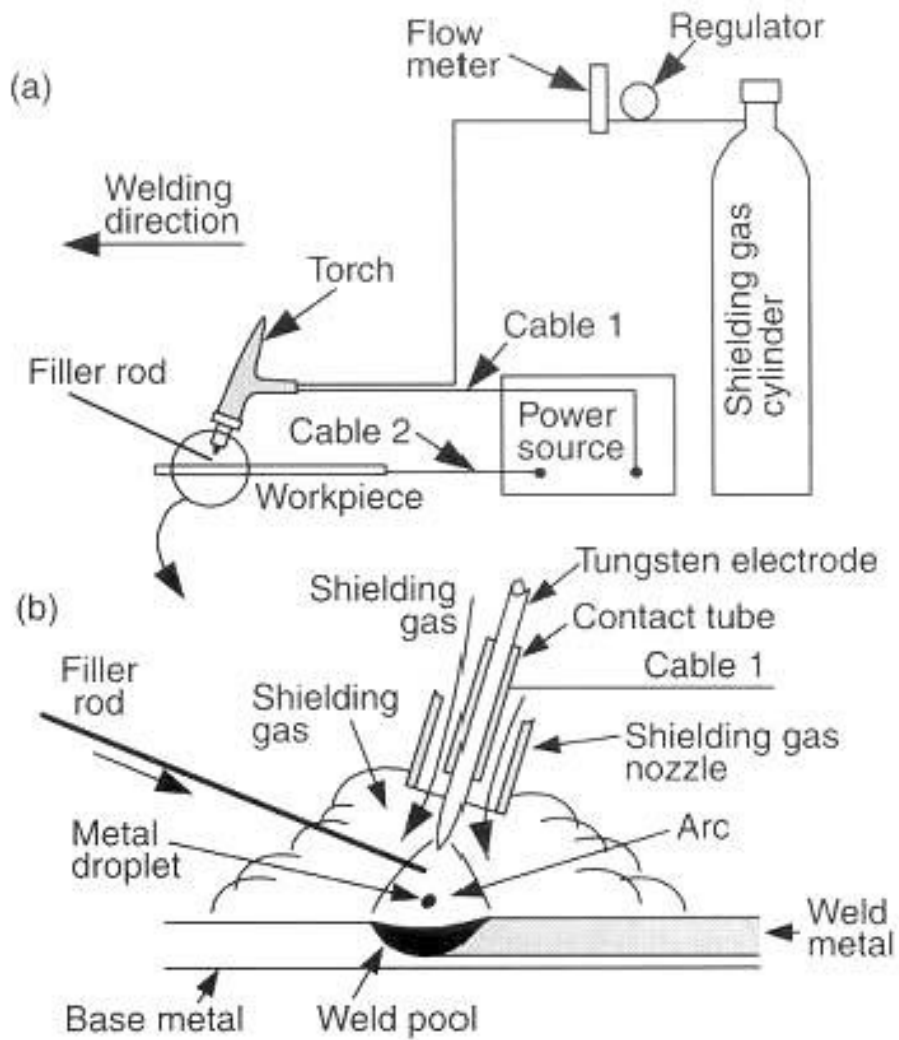


Figure 2 - 4: Gas Tungsten Arc Welding: a) overall process, b) welding area enlarged

Source: "Welding Metallurgy" (2nd Ed) by Sindo Kuo [28]. Reprinted with permission from the Global Rights Department, John Wiley & Sons, Inc. (2 December, 2010)

2.3.1.3 Electron Beam Welding

Electron beam welding is a process that melts and joins metals by bombarding the joint to be welded with an intense beam of high-voltage electrons. The process converts electron energy to thermal energy as the electrons impact and penetrate into the workpiece, which causes the weld-seam interface surfaces to melt and produce the desired weld joint coalescence. Figure 2-5 [28] shows a schematic of the electron beam welding process. The cathode of the electron beam gun is a negatively charged filament, which emits electrons when heated up to its thermionic emission temperature. The electrons are accelerated by the electric field between a negatively charged bias and the anode, passing through the hole in the anode, and then focused by an electromagnetic coil to a point at the workpiece surface. Typical beam currents and accelerating voltage vary over the ranges 50-1000mA and 30-175kV, respectively. A vapour hole (referred to as key hole) can form when a metal is vaporized by an electron beam of very high intensity. The electron beam can be focused to diameters in the range 0.3-0.8mm, resulting in power density as high as 10^{10}W/m^2 [29]. This very high power density makes it possible to vaporize the material and produce deep penetrating keyhole and hence weld, which is a notable advantage in welding thick workpieces. The total heat input per unit length of the weld in electron beam welding is much lower than that of arc welding due to the fact that joints that require multiple-pass arc welding can be welded in a single pass at a higher welding speed. This results in a very narrow heat-affected zone and little distortion. Electron beam welding can also be used for joining reactive and refractory metals in vacuum, and also some dissimilar metals. A limitation of the process is the high installation and operation cost due to the requirements of high vacuum (10^{-3} - 10^{-6} torr) and

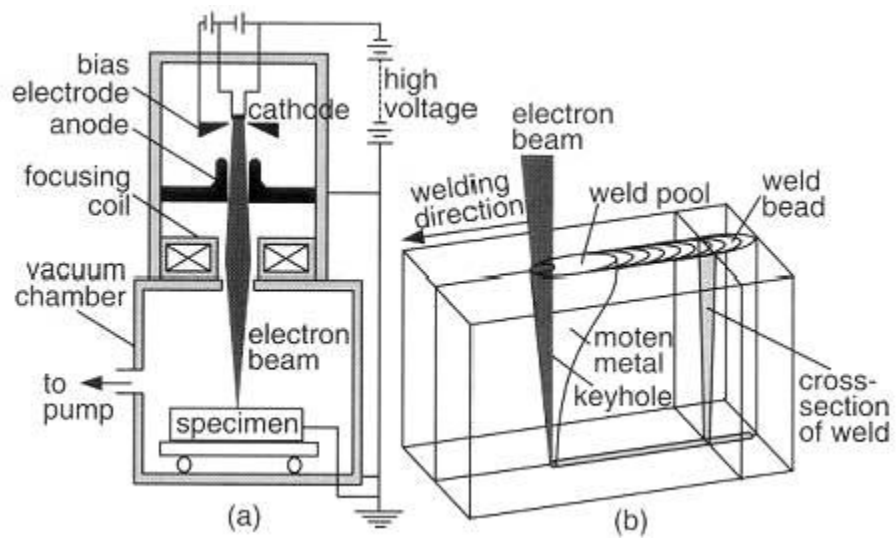


Figure 2 - 5: Electron Beam Welding: a) process; b) keyhole

Source: "Welding Metallurgy" (2nd Ed) by Sindo Kuo [28]. Reprinted with permission from the Global Rights Department, John Wiley & Sons, Inc. (2 December, 2010)

X-ray shielding. The process is also time-consuming due to the long set-up and evacuation time.

2.3.1.4 Laser Beam Welding

“Laser” is an acronym for “Light Amplification by Stimulated Emission of Radiation”. Laser beam welding produces coalescence of materials with the heat obtained from the amplification of concentrated coherent light beam impinging on the surfaces to be welded [12]. The beam, which can be produced either by a solid-state laser or a gas laser, is usually focused by optical elements (mirrors or lenses) to a small spot size to produce a controlled high power density, which melts the metal and, in case of deep penetration welds, vaporizes some of it. A fusion zone forms which on solidification results in a weld joint. In a solid-state laser, a single crystal such as yttrium-aluminum-garnet (YAG) is doped with small concentrations of transition elements or rare earth elements like neodymium. Selective excitation of the electrons of the dopant element can occur upon exposure to high-intensity flash lamps, which subsequently produces laser beams when the excited electrons return to their normal energy states. A schematic diagram of the solid-state laser is provided in figure 2-6 [28]. CO₂ laser, which produces higher power than solid-state laser, is a gas laser produced from the mixture of CO₂, N₂ and He. The gas mixture is continuously excited by electrodes connected to the power supply, producing a laser beam. Laser beam welding can produce deep and narrow welds at high welding speeds, with narrow heat-affected zone and little distortion of the workpiece, and can be used for welding dissimilar parts that vary greatly in mass and size. Vacuum and X-ray shielding are generally not required. A major drawback in the use of laser beam

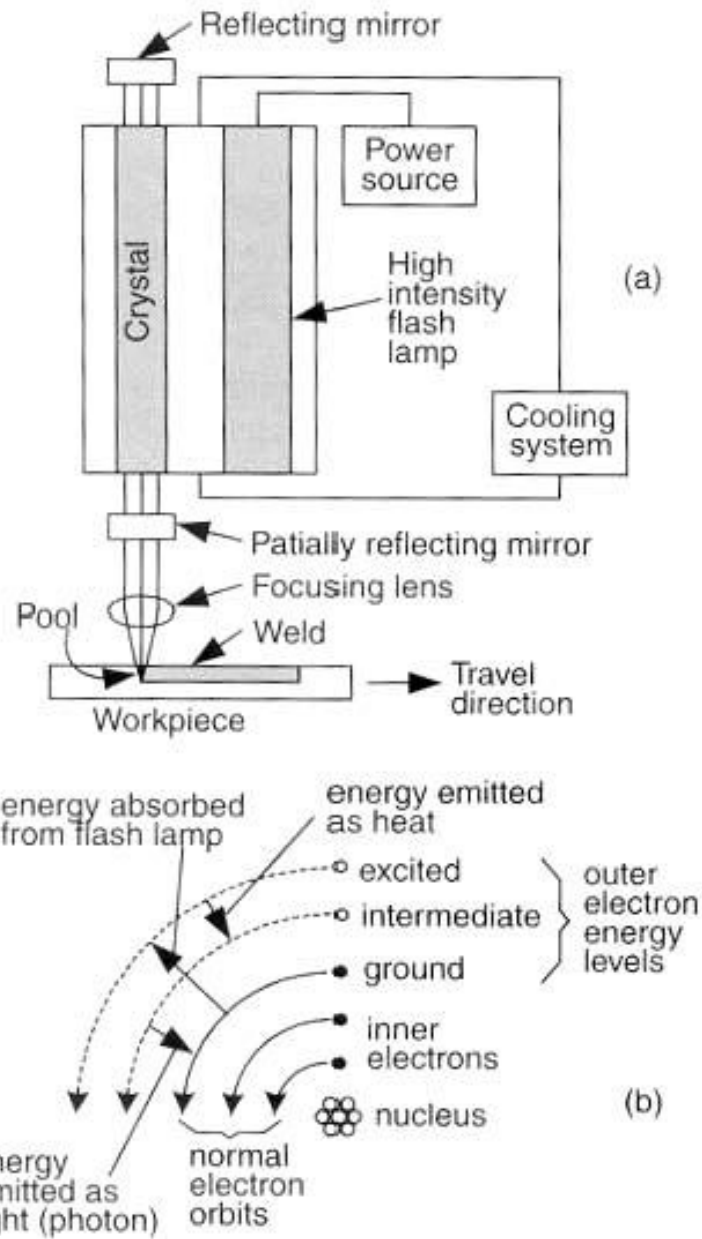


Figure 2 - 6: Laser beam welding with solid-state laser: a) process, b) energy absorption and emission during laser action

Source: "Welding Metallurgy" (2nd Ed) by Sindo Kuo [28]. Reprinted with permission from the Global Rights Department, John Wiley & Sons, Inc. (2 December, 2010)

welding is the very high reflectivity of a laser beam by the metal surface, which reduces the amount of penetrating beam. The equipment cost is also very high.

2.4 On-Cooling Tensile Stresses in HAZ of Fusion Welds

A relationship exists between the temperature reached during welding and the mechanical behaviour of different regions of the welded joint. The dependency of mechanical behaviour on welding temperature usually results in thermal stresses being generated within both the fusion and heat-affected (HAZ) zones of fusion welds. Consequently, residual stresses and distortions of different magnitudes are experienced by different regions in the vicinity of the weld. This can be traced to the fact that different sections of the material in a weld experience different rates of expansion and contraction due to the temperature dependence of the section's elastic modulus and yield strength [30].

The changes in temperature and the resulting stresses during a bead-on-plate weld of a thin plate, made along the x-axis, are schematically represented by figure 2-7 [31, 32]. Figure 2-7 (b) shows the temperature gradients along several sections (A-A, B-B, C-C and D-D) through the weld bead path. Figure 2-7 (c) shows the distribution of normal stress in the x-direction. Ahead of the welding arc (section A-A), the slope of the temperature gradient across the weld (along y) is almost zero, and the corresponding stresses are also almost zero. Along section B-B, where the metal is molten as indicated by the ellipse near O, the slope of the temperature gradient becomes very steep. Away from the arc (in the HAZ), the stress is compressive because the expansion of the metal surrounding the weld pool is restrained by the base metal. Due to high temperatures in these areas, a situation occurs in which stresses in these areas are as high as the yield stress of the base metal at the corresponding temperature. Therefore, the magnitude of

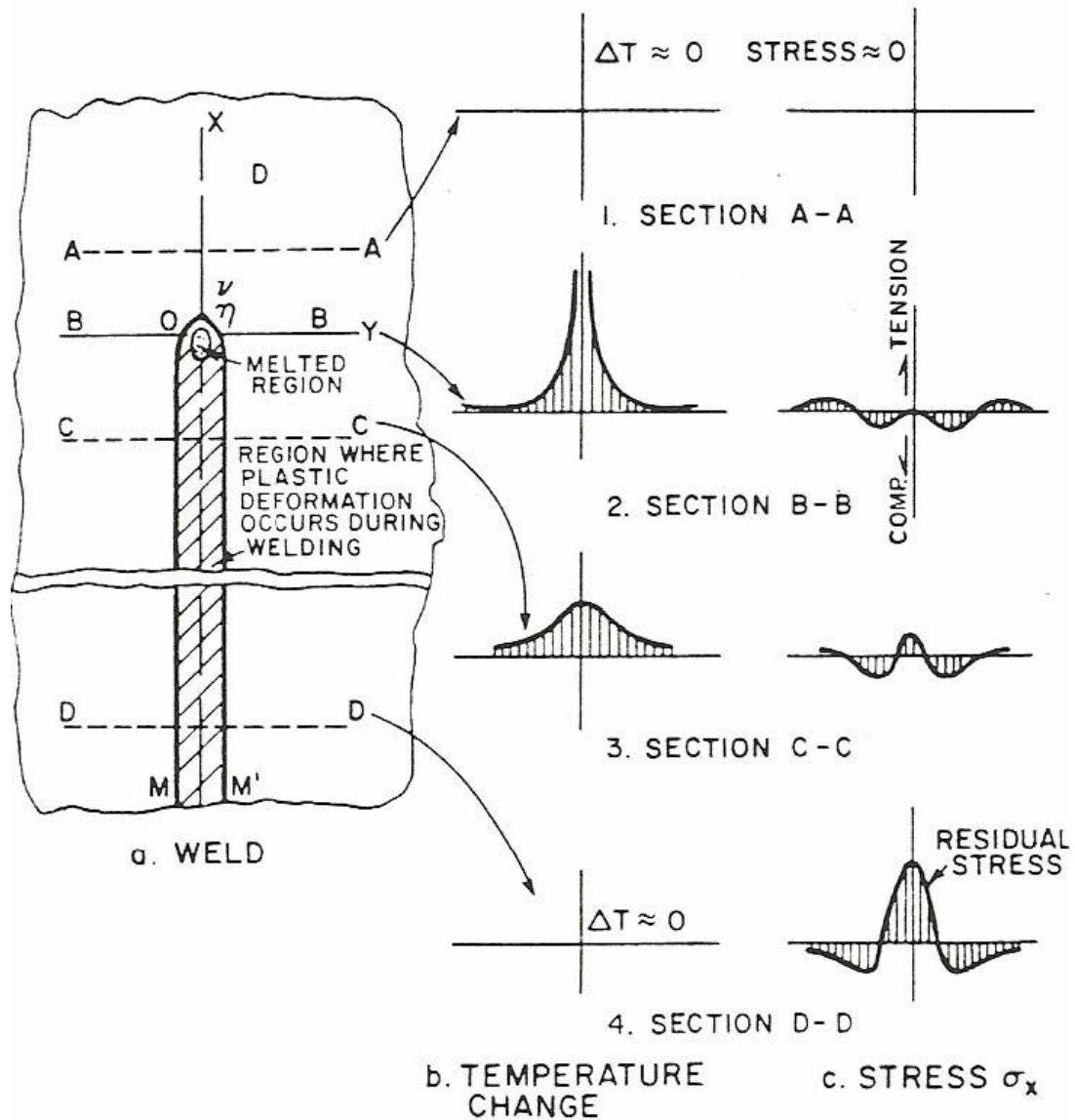


Figure 2 - 7: Schematic representation of changes in temperature and stresses during welding: (a) Weld (b) Temperature changes (c) Stress distribution

Source: "Analysis of Welded Structures" by K. Masubuchi [32]. Reprinted with permission from Elsevier (29 November, 2010) and the Author (30 November, 2010).

compressive stress passes through a maximum with increasing distance or with decreasing temperature from the weld. However, tensile stresses occur in regions far away from the welding arc. Somewhat behind the welding arc (C-C), the temperature gradient slope becomes less steep since the weld-metal and the base-metal have cooled. As they shrink during cooling, tensile stresses are generated in regions in, and adjacent to, the weld while the stresses become compressive as the distance from the weld increases. Along section D-D, some longer distance behind the welding arc, the temperature gradient slope approaches zero again and high tensile stresses exist in, and adjacent to, the weld while compressive stresses exist in areas away from the weld.

The development of tensile stresses in the fusion and heat-affected (HAZ) zones of fusion welds during weld cooling plays an important role in weld cracking. This is a major mechanical factor that contributes significantly to cracking during conventional fusion welding of superalloys. Apart from on-cooling tensile stresses, other metallurgical factors necessary for cracking are equally important. The different weld defects associated with conventional fusion welding processes will be discussed in the next section.

2.5 Weld Defects Associated with Fusion Welding Processes

Fusion welding processes are usually characterized by a number of weld defects. These include cracks and fissures, gas porosities, inclusions, incomplete fusion and others. Cracks and fissures refer to discontinuities that are produced by local rupture. The general types of cracks include: (a) transverse cracks in the base metal perpendicular to the welding direction; (b) longitudinal cracks in the base metal parallel to the welding direction; (c) microcracks (microfissures) or macrocracks in the weld metal; (d) centreline longitudinal weld-metal cracks; (e) crater cracks; and (f) start cracks or

bridging cracks. Transverse cracks usually result from external contamination or a base metal with poor weldability. Longitudinal cracks are caused by the combination of a strong weld metal and weak, low-ductility base metal. Weld-metal microfissuring can result from contamination or impurities in the weld metal that lower weldability of the metal. Centreline longitudinal cracking is caused by concave beads or a very deep, narrow weld bead. Crater cracking occurs when the arc is extinguished over a relatively large weld pool; and the resulting concave crater is prone to shrinkage cracking. Bridging cracks occur in highly stressed joints where good penetration is not achieved at the arc initiation point. Reduction in base-metal cracking can be achieved by reducing heat input and depositing small beads, which result in lower residual stresses.

Gas porosities describe gas pockets or voids in the weld metal. Typical causes of gas porosity include improper shielding, moisture, incorrect amperage or a long arc length. Inclusions are usually slag, oxides, or other non-metallic solids entrapped in the weld metal between adjacent beads or between the weld and the parent metal. Gas-metal and slag-metal reactions can produce gas porosity and inclusions, respectively, in the weld metal and affect the weld metal properties.

Incomplete fusion can be caused by incomplete coalescence of some portion of the filler metal with the base metal. It can also feature between weld beads in case of multi-pass welds. It is a two dimensional flaw that occurs when insufficient heat is absorbed by the underlying metal from the weld, causing incomplete melting at the interfaces of the weld and the base metal after successive passes. Incomplete fusion is characterized by discontinuities which are usually elongated in the direction of welding with either sharp or rounded edges, depending on the conditions of formation. Lack of penetration is also a


weld defect, caused by incorrect welding technique or by improper root gap, which occurs when the weld metal has not penetrated to the bottom of the weld joint. Other weld defects include (i) undercut: a groove melted into the base metal adjacent to the toe, cap or root of the weld metal and left unfilled by the weld metal, which act as a stress raiser and cause fatigue problems; (ii) Overlap: a protrusion of the weld metal beyond the toe, face or root of the weld; (iii) shrinkage voids: a cavity-type imperfection that forms by shrinkage during solidification; (iv) Arc Strikes: imperfections resulting from localized remelting of metal surface, caused by inadvertent contact between an electrode and the metal surface; (v) underfill: a depression on the face of the weld or root surface extending below the surface of the adjacent base metal. Examples of few typical arc welding defects in superalloys are presented in figure 2-8 [3].

2.6 Cracking During Fusion Welding Processes

Cracking in welds can occur in the fusion zone, which is referred to as solidification cracking, and/or in the heat-affected zone. These are discussed next.

2.6.1 Solidification Cracking

Solidification cracking, which is observed frequently in castings and ingots, can also occur in weld deposits of fusion welds during cooling. It occurs predominantly at the weld centerline or between columnar grains that form on solidification of the weld metal. Solidification cracking is a type of cracking that occurs during the terminal stage of solidification, when the tensile stresses developed across adjacent grains exceed the strength of the almost completely solidified weld metal [33-35]. During solidification, the weld metal tends to contract because of both solidification shrinkage and thermal contraction. Though the base metal also contracts, it does not contract as much as the



This item has been removed due to copyright issues. To view it, refer to its source.

Figure 2 - 8: Typical arc welding defects

Source: Superalloys: A technical Guide [3]

weld metal because it is neither melted nor heated as much as the weld metal on the average. The contraction of the solidifying metal can therefore be hindered by the base metal, especially if the workpiece is constrained and cannot contract freely. Consequently, tensile stresses develop in the solidifying weld metal. A point is reached when the semi-solid material can no longer accommodate the thermal shrinkage strains associated with weld solidification and cooling. In order to relieve the accumulating strains, cracks form at susceptible sites such as solidification grain boundaries and interdendritic regions, which are at least partially wetted [36].

2.6.1.1. Factors Affecting Solidification Cracking Susceptibility

The factors affecting solidification cracking susceptibility of weld metals can be either metallurgical or mechanical. Some of the metallurgical factors include:

- A. The solidification temperature range: the wider the solidification (freezing) temperature range, the larger the S+L region in the weld metal or mushy zone and thus the larger the area that is weak and susceptible to solidification cracking. The larger S+L region can result from the presence of undesirable impurities such as sulphur and phosphorus, or intentionally added alloying elements
- B. The amount and distribution of liquid at the terminal stage of solidification: maximum crack susceptibility occurs somewhere between the composition of a pure metal and the composition of a highly alloyed metal. A pure metal is not susceptible to cracking because there is no low-melting-point eutectic present at the grain boundary to cause solidification cracking. In highly alloyed material, on the other hand, the eutectic liquid between the grains can be abundant enough to heal incipient cracks. Somewhere in between these composition levels, however,

the amount of liquid between grains can be just large enough to form a thin, continuous intergranular film to make the materials susceptible to solidification cracking but without extra liquid for healing the cracks.

- C. The ductility of the solidifying weld metal: the less ductile a solidifying weld metal is, the more likely it will crack during solidification

- D. The grain morphology of weld metal: Fine equiaxed grains are often less susceptible to solidification cracking than coarse columnar grains [37]. This has been attributed to the fact that fine equiaxed grains can deform to accommodate contraction strains more easily, that is, it is more ductile, than columnar grains. Liquid feeding and healing of incipient cracks can also be more effective in fine-grained material, and the grain boundary area is greater, which reduces the concentration of low-melting-point segregates at the grain boundaries.

The mechanical factors affecting solidification cracking include residual stresses and joint geometry. Though the metallurgical factors described earlier are very important for the occurrence of solidification cracking, no cracking can occur without the presence of tensile stresses acting on adjacent grains during solidification. The thermal cycle of the welding process always results in residual stresses in the weld metal. These stresses can be due to thermal contraction or solidification shrinkage or both. The severity of the stresses depends on the degree of restraint offered by the welded joint. Generally, the thicker or stronger the plates being welded, the higher is the restraint. The higher is the restraint; greater is the magnitude of the residual stress.

2.6.1.2. Mechanism of Solidification cracking

The mechanism of solidification cracking can be illustrated with figure 2-9 [38]. It is generally understood that the partition and rejection of alloying elements at the columnar grain boundaries and ahead of the advancing solid-liquid interface causes marked segregation. The segregants subsequently form low-melting phases or eutectics with the metal to produce highly wetting films at grain boundaries as illustrated. The alloying elements that are most-likely to segregate this way have characteristics including: low partition coefficients, ready formation of low-melting-point compounds or eutectics with the base alloy, and low wetting angle with the metal and thus possess the ability to spread along grain boundaries. As a result of these, the boundaries are weakened and cracks form under the influence of the tensile residual stresses that are generated during cooling of welds [30].

2.6.2 Heat-Affected Zone Liquation Cracking

Liquid formed on grain boundaries in the heat-affected zone (HAZ) during fusion welding can wet the grain boundaries and spread along them to form a continuous film. When this formation of continuous intergranular film is accompanied by sufficient tensile thermal stresses, cracks can form along the grain boundaries and extend into the fusion zone. Such cracking can be referred to as liquation cracking, hot cracking or microfissuring in the HAZ. Figure 2-10 [38] illustrates the formation of liquation cracks in a typical alloy. While the weld deposit is still liquid, compressive stresses tend to close up liquation cracks. However, the stresses (or strains) in the HAZ become tensile as the melt solidifies and these open up cracks [30].

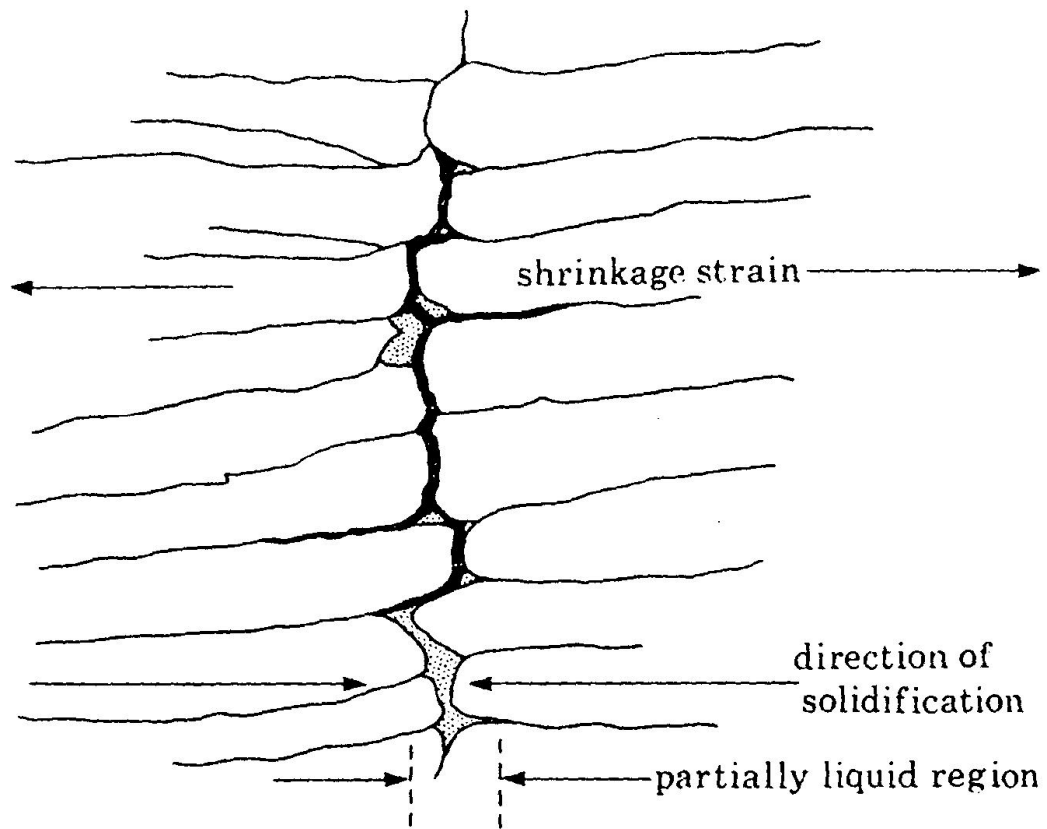


Figure 2 - 9: Schematic illustration of the mechanism of solidification cracking.

Source: Philosophical Transactions of the Royal Society of London [38]. Reprinted with permission from The Royal Society (22 November, 2010).

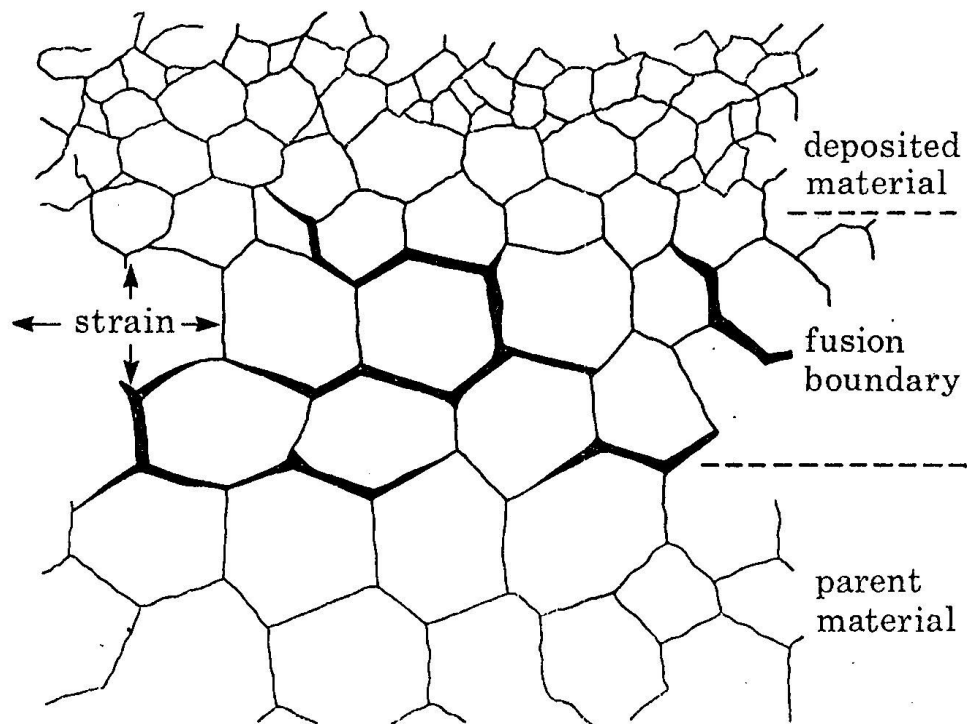


Figure 2 - 10: Schematic diagram illustrating liquation cracking

Source: Philosophical Transactions of the Royal Society of London [38]. Reprinted with permission from The Royal Society (22 November, 2010).

It is known that grain boundary liquation can occur by either supersolidus melting or by non-equilibrium sub-solidus melting. Non-equilibrium sub-solidus melting is particularly more harmful due to its ability to widen the temperature range over which a weldment remains liquid and thus increase the material's susceptibility to HAZ liquation cracking [39]. The sub-solidus melting can occur by two main mechanisms, namely:

1. Constitutional liquation of second phase particles.
2. Segregation of melting point suppressing elements on the grain boundaries during solidification and thermal processing and during pre-weld heat treatment.

2.6.2.1 Constitutional Liquation

Constitutional liquation theory was first proposed and explained in the literature by Pepe and Savage in 1967, when they observed liquation of titanium sulphide particles in 18-Ni maraging steels [40]. This theory has been subsequently used to explain non-equilibrium sub-solidus melting of second phases in different alloys during fusion welding, which is generally known to cause HAZ liquation cracking. Examples, as observed by different researchers, include the constitutional liquation of: M_3B_2 in Udimet 700 [41], Cr_7C_3 and $Ti(CN)$ in Inconel 600 [42], TiS in 18-Ni maraging steel [40], TiC in austenitic alloy A286 [43], M_6C in Hasteloy X [41], MC Carbide and MNP Phosphides in Incoloy 903 [44], NbC and Laves phase in Inconel 718 [45], and MC Carbide in Allvac 718Plus® [46]. The theory of constitutional liquation proposed by Pepe and Savage will be presented next. This will be followed by a review of constitutional liquation of second phases in IN 738.

2.6.2.1.1 Constitutional Liquation Theory

The behaviour of a hypothetical binary alloy system can be illustrated by the constitutional phase diagram of figure 2-11 [40]. The alloy, of nominal composition C_0 , when heated progressively from T_1 to T_4 , exhibits different behavior for an infinitely slow heating rate and for an extremely rapid heating rate. At temperature T_1 , the alloy of composition C_0 consists of the intermetallic compound A_xB_y , distributed as a second-phase precipitate in the α solid solution. Under an equilibrium solidification condition corresponding to an infinitely slow heating rate, the solubility of B in the matrix increases as the temperature is increased. At T_2 , the last remaining A_xB_y dissolves, converting the alloy to a homogeneous single phase solid solution of composition C_0 . No further changes occur as the temperature further increases from T_2 to just below T_5 . At T_5 , which is the equilibrium solidus of the alloy, the first infinitesimal amount of liquid of composition corresponding to point c is formed. Therefore, under an equilibrium condition, the two phase alloy is gradually converted to a single phase alloy. It remains a single phase until the first melting occurs at the equilibrium solidus of the alloy.

The dissolution of A_xB_y under non-equilibrium solidification condition, which corresponds to an extremely rapid heating rate, significantly departs from that that occurs under equilibrium solidification. The disappearance of A_xB_y upon heating requires its dissociation and subsequently the accommodation of the excess component of B, which is liberated as additional solute in the surrounding matrix. The overall rate of dissolution of A_xB_y occurs at a finite rate, which may be limited by either or both of the dissociation or accommodation process step. As the heating rate is increased, a critical heating rate will be reached above which the time required to raise the temperature to the equilibrium

solidus temperature will be insufficient to achieve complete dissolution of A_xB_y . At this critical heating rate and all heating rates above it, the dissociation and diffusion process steps will occur at finite rates. The equilibrium structure of A_xB_y as a function of temperature is represented by the vertical line emanating from C_0 in figure 2-11. Since the system would be striving to maintain equilibrium, any departure from an equilibrium structure due to rapid heating results in solute redistribution. For a spherical A_xB_y precipitate and a heating rate above the critical heating rate, the changes expected in the vicinity of A_xB_y during heating to temperatures of T_3 , T_e and T_4 , respectively, can be illustrated by figures 2-12a to 2-12c. During heating to T_3 , A_xB_y dissociates since at T_3 , A_xB_y is unstable with respect to a single phase solid solution of composition C_0 . A_xB_y shrinks somewhat from its original volume to a smaller volume as represented by dashed and solid circles, respectively, in figure 2-12a. The B atoms liberated diffuse into the adjacent α matrix. However, figure 2-11 shows that A_xB_y must be in contact with the matrix of composition m if the two phases are to co-exist. It is therefore necessary that a concentration gradient exist in the α matrix, such that a maximum concentration value, m , exists at the A_xB_y phase interface, which decreases toward the original matrix composition, o , at the interior of the α phase. In order to maintain a material balance, the area of the double cross-hatched region of figure 2-12a must be equal to the area of the single cross-hatched region. The concentration gradient slope would be dependent on:

1. The heating rate: the faster the heating rate is, the steeper the concentration gradient
2. The diffusivity of solute: the faster the diffusivity of solutes, the shallower the concentration gradient

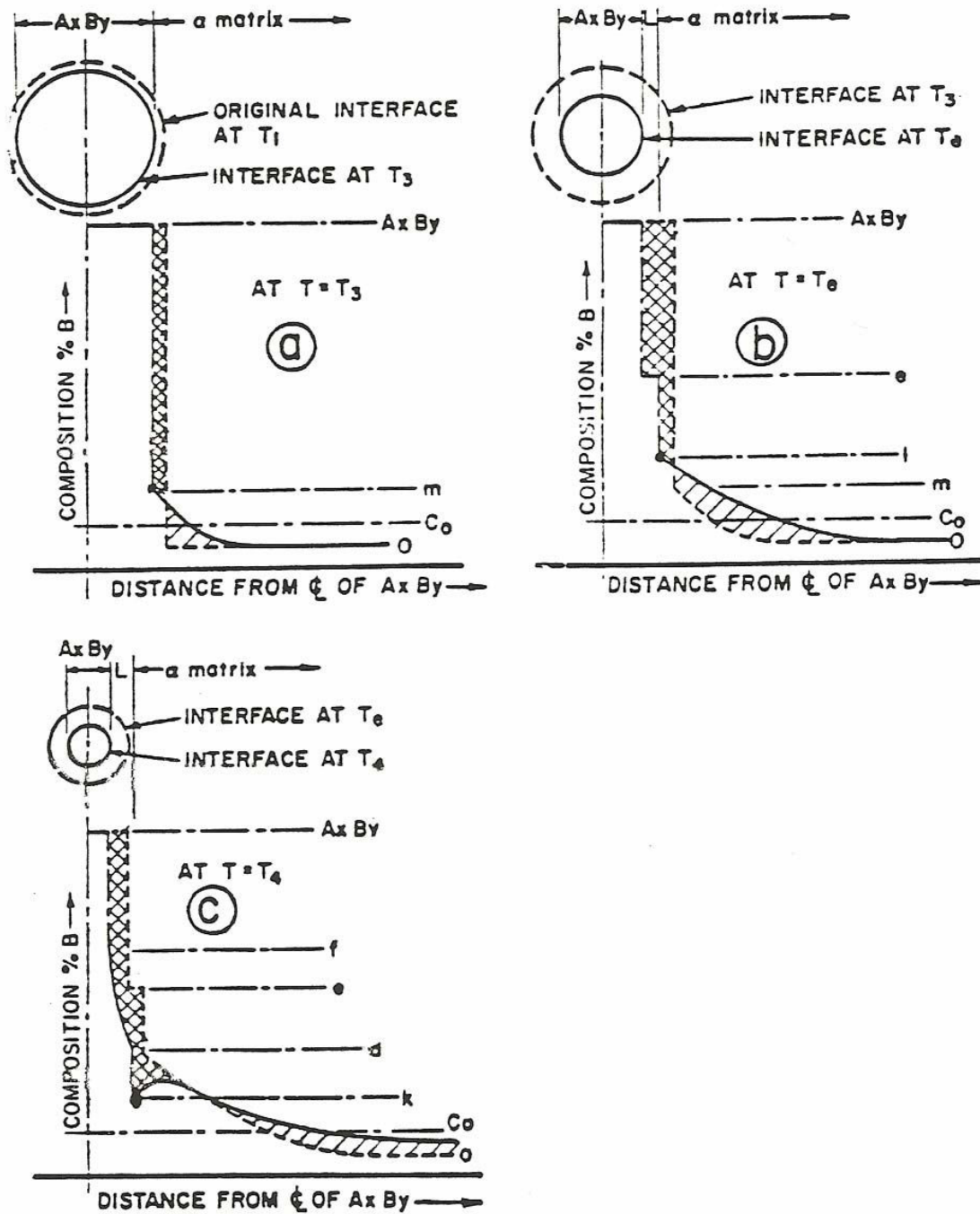


Figure 2 - 12: Schematic representation of the concentration gradients at various temperatures during formation of constitutional liquation

Source: *Welding Journal* [40]. Reprinted with permission

3. The relative ease with which the solute atoms are accommodated by each successive single phase region in the diffusion couple

A_xB_y continues to dissociate during heating from T_3 to T_e , the particle size continues to decrease as represented in figure 2-12b, where the dashed and solid circles represent the location of A_xB_y interface at T_3 and T_e , respectively. At the eutectic temperature, T_e , the composition corresponding to point e permits the formation of a single phase liquid at the A_xB_y interface, thus, the undissociated portion of A_xB_y is surrounded by a liquid phase of composition e, which, in turn, is surrounded by the α matrix. Figure 2-12b shows the solute distribution in the three phases co-existing at temperature T_e . On further heating to T_4 , additional time is allowed for the dissociation of A_xB_y . The expected solute distribution at T_4 is shown by figure 2-12c. Upon heating above T_e , the equilibrium solubility of α phase decreases along the solidus line “akl”. Therefore at T_4 , the concentration of the solute in solid solution and the liquid film in contact with one another correspond to k and d, respectively. Each particle of A_xB_y remaining undissolved at T_4 is surrounded by a liquid film of variable composition ranging from “f” at the A_xB_y interface to “d” at the matrix interface. This causes localized melting under non-equilibrium heating rates at temperatures between T_e and T_5 , a phenomenon termed as constitutional liquation. Therefore, constitutional liquation occurs under rapid heating and results in the formation of solute-rich liquid pools at temperatures well below the equilibrium solidus of the alloy [40]. Interactions between these liquated regions and the grain boundaries during fusion welding could establish a microstructure that is sensitive to intergranular liquation cracking.

2.6.2.1.1 Constitutional Liquation of Phases in IN 738

The micro-constituents present in cast IN 738 can be generally classified as: a) secondary solidification reaction products, which form as a result of solidification reaction during ingot casting of the alloy, and b) post-solidification solid-state reaction products [39]. Microstructural examination of the HAZ of IN 738 fusion welds has shown grain boundary liquation in the alloy, which resulted from the sub-solidus constitutional liquation of the various micro-constituents that were present in the alloy before welding. Ojo et al [47, 48] observed that apart from the super-solidus melting during fusion welding of IN 738, which is expected to occur in all weldments due to heating above equilibrium solidus temperature, constitutional liquation of solidification products and of γ' precipitates occurred. Constitutional liquation of γ' precipitates, the main strengthening phase of the alloy, was observed to have occurred in the HAZ. This γ' phase liquation was found to have contributed significantly to the HAZ microfissuring. Besides the γ' phase liquation, Cr- and Mo- rich M_3B_2 boride, Zr-Ti –rich M_2SC sulphocarbide particles and MC-type carbides, which are secondary solidification products in IN 738, were also observed to have liquated in the HAZ during welding. This contributed to HAZ liquation cracking in the alloy. Also, extensive cracking was observed when M_3B_2 , M_2SC or MC carbide particles coexisted in a γ - γ' eutectic colony, suggesting a synergistic effect between the phases.

2.6.2.2 Grain boundary Segregation

Grain boundary segregation is another mechanism for grain boundary liquation. It occurs by the segregation of melting point suppressant elements on grain boundaries, which reduces the melting temperatures of the grain boundary material relative to the

surrounding matrix. For grain boundary liquation cracking to occur by this mechanism, grain boundary segregation must take place first. Non-equilibrium sub-solidus grain boundary melting then occurs in the HAZ during welding at temperatures which are above the reduced melting temperature of the grain boundary material [39]. Segregation of impurities on grain boundaries before welding can be induced by either equilibrium segregation [49-52] or non equilibrium segregation [53-57]. Equilibrium grain boundary segregation occurs by the movement of solutes from the bulk of the alloy to grain boundaries when the material is held at a sufficiently high temperature that can promote an appreciable diffusion of solutes. The solute atoms are absorbed to reduce the interfacial free energy of the loosely packed grain boundary region. Impurity atoms can also segregate from the bulk alloy to other loosely packed sites such as free surfaces, phase boundaries, stacking faults and precipitate/matrix interfaces. The driving force for equilibrium grain boundary segregation is a reduction in the grain boundary free energy. As the temperature of the isothermal heat treatments increases, the level of segregation decreases. Equilibrium grain boundary segregation is restricted to a few atoms layers of the grain boundary and the total amount is usually of the order of a few monolayers.

Non-equilibrium segregation occurs during cooling from the thermal treatment temperature. In addition to the equilibrium concentration of vacancies generated and distributed during elevated temperature heat treatment, some vacancy-solute complexes can also form as a result of positive binding energy between the solute atom and vacancy. The diffusion coefficient of the solute-vacancy complex exceeds that of the solute alone. During cooling to lower temperatures, supersaturation of vacancy concentration occurs in the matrix, and the grain boundaries can act as sinks for vacancies. A concentration

gradient of vacancies develops near the grain boundaries and vacancies within diffusion range of the grain tend to migrate to the grain boundaries. Vacancy diffusion towards the grain boundaries tends to drag solute-vacancy complexes towards the boundaries, producing a solute-rich grain boundary region. This process is thermodynamically driven by the decrease in free energy associated with the annihilation of excess vacancies at the grain boundary sinks [58]. The degree of non-equilibrium segregation has been found to depend on the starting temperature, cooling rate, bulk concentration of solutes and the binding energy between solute atoms and vacancies [59-61]. An increase in thermal treatment temperature increases equilibrium concentration of vacancies and the degree of segregation increases. If sufficient time is not available for the diffusion of complexes to grain boundaries to occur when the cooling rate is high, the degree of segregation will be reduced. On the other hand, if the cooling rate is very slow, causing a gradient in concentration of solute atoms between the grain boundary and the grain interior, the segregated solute atoms may diffuse back to the grain interiors, thereby eliminating segregation [62].

The effect of both equilibrium and non-equilibrium segregation of solutes and their close relationship to the weldability of nickel-based superalloys has been studied [62]. Segregation was found to alter the liquid wettability of grain boundaries. The presence of solutes in grain boundary liquid lowered the solidification range of the liquid and contributed to HAZ microfissuring.

2.7 A More Recent Development – Friction Welding

Earlier discussions on conventional fusion welding processes and the phenomena associated with them have clearly revealed that the processes are characterized by

melting and resolidification in both the fusion and heat-affected zones. This presence of melting and resolidification, coupled with the development of tensile stresses, result in both solidification cracking and heat-affected zone liquation cracking. Nickel-base superalloys, and particularly those with high volume fraction of the ordered intermetallic $\text{Ni}_3(\text{Al,Ti})$, γ' , phase (> 40%) such as IN 738, are highly susceptible to intergranular microfissuring in the HAZ during conventional fusion welding processes. The fundamental cause of the weldability problem, as discussed earlier, is the liquation of grain boundary region due to constitutional liquation of the various phases, which weakens and embrittles materials during joining. Developments in welding research have resulted in supposedly exclusive solid-state friction joining processes like inertia friction welding, continuous drive friction welding, linear friction welding (LFW) and friction stir welding, which are state-of-the-art in producing crack-free welds in difficult-to-weld structural alloys.

Friction welding can be described as a process in which the heat for welding is produced by direct conversion of mechanical energy to thermal energy at the interface of the workpieces without the application of electrical energy, or heat from other sources, to the workpieces [12]. It generally involves the rubbing together of two surfaces under the influence of an axial compressive pressure. This generates frictional heat at the interface, which rapidly raises the temperature of the workpieces, over a very short axial distance, to values approaching, but below, the equilibrium melting range. The friction-causing motion is stopped after a sufficiently plasticized heated zone is formed. Welding occurs under the influence of the compressive stress that is applied while the heated zone is still

in the plastic temperature range. Most nickel-base and cobalt-base superalloys are easily friction welded to themselves and to alloy steels.

2.7.1 The Development of Friction Welding Processes

The scientific study of friction welding started in 1956 with the successful demonstration of the possibility of achieving high quality butt welds between metal rods [63]. Since then, intensive research has been launched by Vill [64] and others in the U.S.S.R. in order to understand the process from scientific perspective. The process was later introduced to the U.S.A. in 1960. Hollander [65] and Cheng [66, 67] did some pioneering work on parametric analysis and thermal aspects of friction welding at the American Machine and Foundry Company. Later in 1962, Caterpillar Tractor Company developed the so-called inertia welding, a modified friction welding process employing a flywheel to store the energy required for welding [68]. The process is referred to as either inertia friction welding or flywheel friction welding. Since 1962, the names “conventional” or “continuous-drive” friction welding have been used specifically for the original Russian process, while “inertia” or “flywheel” friction welding have been commonly used for the Caterpillar process. The Welding Institute (TWI), Cambridge UK, also entered the friction welding technology in the early 1960s with the development of continuous-drive-type machines. TWI later developed the linear friction welding which enables non-rotationally symmetrical parts to be joined. In 1991, friction stir welding was developed and patented by TWI. Ever since these historical times, industries, federal laboratories, and universities have been investigating friction welding processes for joining plastics, aluminum, steel, titanium, metal matrix composites and superalloys. Subsequent discussions in the next section focus on the various friction welding processes.

2.8 Friction Welding Processes

2.8.1 Inertia Friction Welding

The main idea behind inertia friction welding is that a pre-determined amount of kinetic energy can be stored in a freely rotating flywheel, and completely converted into frictional welding heat without the use of clutches, brakes, time or distance [69]. Figure 2-13a [68] illustrates, schematically, the principle of the inertia friction welding process, showing the pre-weld, weld and post-weld conditions. One of the two workpieces is clamped in a non-rotating vise or fixture. The other part is held by a chuck. The chuck, along with a replaceable flywheel, is mounted on a rotating spindle. The drive motor accelerates the flywheel-spindle assembly and brings rotating part to a pre-determined speed of N rotations per minute. The speed corresponds to a specific energy level and is dialed into the machine. When the proper speed is reached, the drive motor is shut off, thereby establishing a free-wheeling system. The non-rotating part is then pushed against the rotating part under a pre-determined constant pressure, P . The kinetic energy of the freely rotating flywheel is rapidly converted to heat at the weld interface as the axial pressure is applied. The rotating part is rapidly brought down to stand-still by the interfacial friction that generates the heat, softening the material and causing plastic flow and upset (length reduction). The only external variable during the actual welding process is the axial pressure between the workpieces. All other characteristics such as weld time, weld torque between the pieces and upset are results of the welding process. Figure 2-14 [69] shows a labeled schematic of a typical inertia welder.

Figure 2-13b [68] shows the three-stage model used to characterize the mechanism of inertia friction welding based on the history of the frictional torque at the interface. The

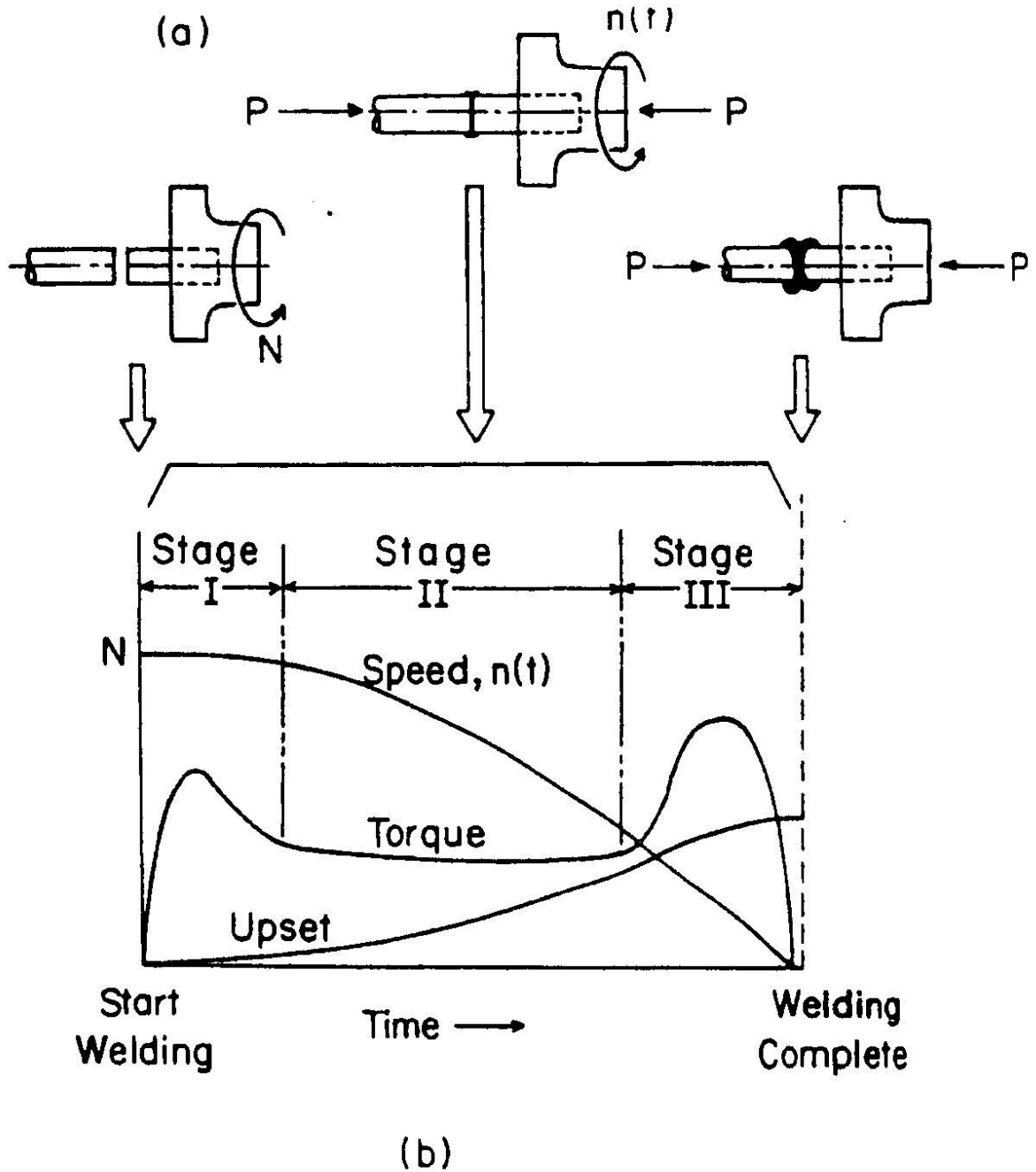


Figure 2 - 13: Some characteristics of flywheel friction welding process

Source: *Welding Journal* [68]. Reprinted with permission

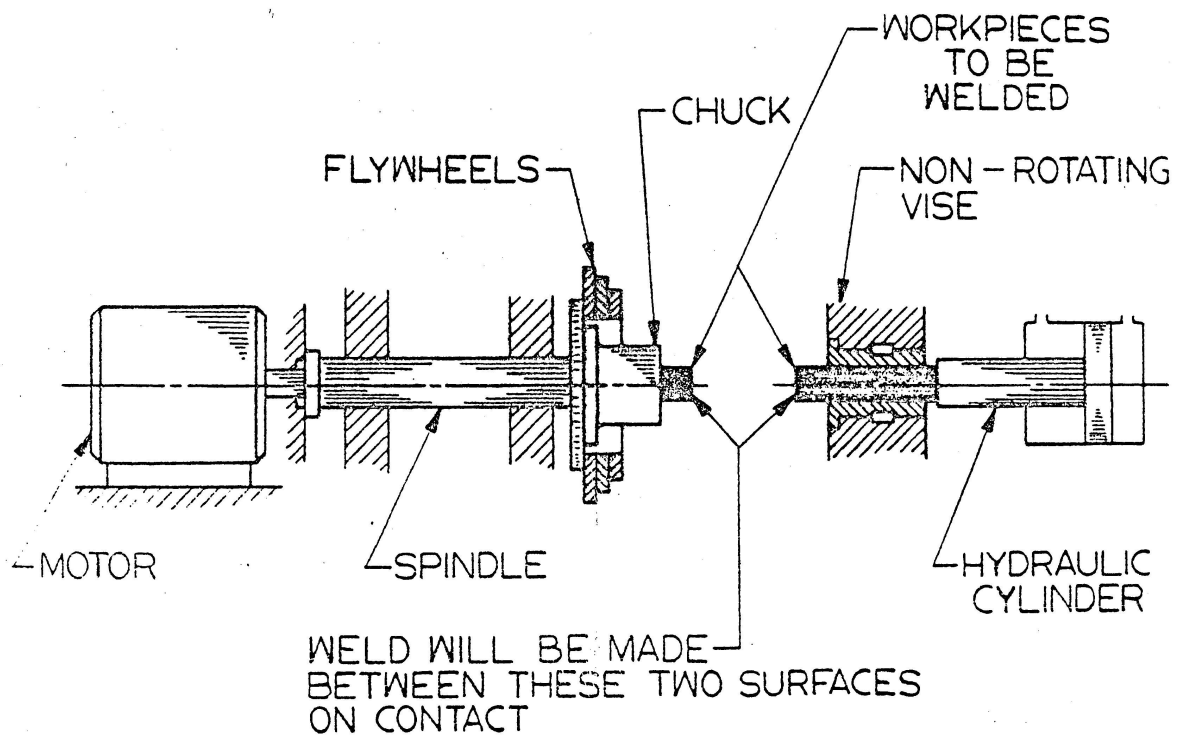


Figure 2 - 14: A schematic of an inertia welder

Source: "Inertia Friction Welding". Courtesy of Manufacturing Technology, Inc. [69]

three stages are distinct and include contact or pre-heat, heat, and forging, respectively. Wearing of the surfaces occurs during stage I during which interlocking and adhesion of surface particles result in rapid increase of torque. The torque reaches a peak and the whole area is brought into real contact. Surface layers are disrupted by a large portion of the stored kinetic energy dumped abruptly at the interface. This causes softening of the material on the surfaces and initiates thermoplastic flow. The value of power input is highest in stage I due to the large torque and high rubbing speed. Plastic flow during stage I is essentially confined to a very thin layer at the interface without significant spread into the bulk of the material. The torque curve drops in the later part of stage I because of the predominance of thermal softening over strain hardening.

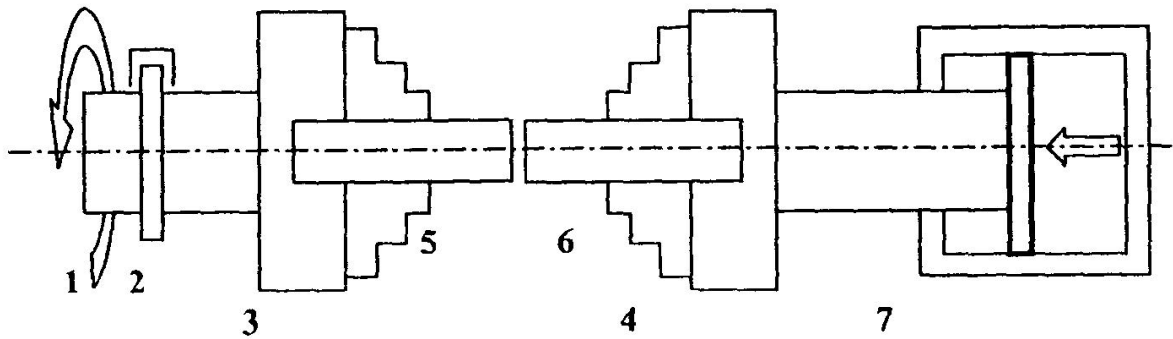
Transition from stage I to stage II indicates a balancing effect between strain hardening and thermal softening. The torque drops to a fairly steady state value. At stage II, the welding process is self-adjusting and torque curve remains practically unchanged, as shown in figure 2-13, until the stage II to stage III transition occurs. The temperature gradient across the interface decreases and the narrow deformation zone widens rapidly. Stage III is dominated by torsional forging and gradual stiffening of the material at the weld, which causes the torque to reach another peak. The amount of upset continues to increase while the material flushes out of the widening heat-affected zone, from the centre of the interface, through a spiral path to the outside of the periphery. Apart from the temperature, torque and upset changes, another characteristic of the process is the continuously decreasing surface velocity of the workpiece. The surface velocity begins at the start of stage I at some initial value as needed for the particular workpiece, and decreases along a parabolic curve to zero, at which time the weld is complete. Stage III

terminates after the rotation is completely stopped and the weld material becomes completely rigid.

The majority of inertia welders in production today are located in the automotive and earthmoving industry [70], with requirements for high production, consistent part quality, low part costs and maintenance. Applications include: axle shaft / flange, steel shafting welded to a turbine rotor, starter pinion gear to hollow shaft. Pratt and Whitney Aircraft (PWA) used inertia welding for aircraft parts as far back as the 80s [71]. PWA first used inertia friction welding to join aircraft engine gear clusters of low alloy steels. These were finished machined before friction welding, which produced gear clusters with high tolerances. Welding of jet engine shafts to discs by inertia friction welding has become standard procedure, with only removal of the weld flash, a minor job, after the joint is completed [71]. The application of inertia friction welding is becoming increasingly attractive in the aerospace industry. Several researchers [72-75] have reported its use in producing successful welds in nickel-base superalloys.

2.8.2 Continuous-Drive Friction Welding

In continuous drive friction welding, one of the components is held stationary while the other component is rotated at a constant speed as shown in figure 2-15 [76]. The two workpieces are then pushed against each other under an axial pressure for a certain amount of time (frictioning time). During frictioning, as the two surfaces continue to rub against each other, heat is generated at the interface and the material on both sides of the interface softens. This softening causes a radial outflow of an upset collar. The rubbing usually continues at the interface until a certain axial shortening (or upset or burn-off) of the specimens has been produced or a certain weld time has elapsed [77]. The clutch is



1. Motor
2. Brake
3. Rotating Chuck
4. Non Rotating Chuck
5. Rotating Workpiece
6. Non Rotating Workpiece
7. Hydraulic Cylinder

Figure 2 - 15: Layout of continuous drive friction welding.

Source: Journal of Materials Processing Technology. Reprinted from [76] with permission from Elsevier (25 November, 2010).

then separated from the drive, and the rotating workpiece is stopped rapidly within a certain braking time. The axial pressure is usually increased to a higher value (forging pressure) for a short period of time after rotation has stopped and the weld metal cools under pressure. In another case, the axial pressure can be kept at the same value as the frictional pressure.

Duffin and Bahrani [78, 79] proposed a theory for the mechanics of continuous drive friction welding and they identified the different stages and phases involved in the process. The speed of rotation, torque, axial force and axial shortening vary with time as illustrated in figure 2-16 [79]. The welding cycle is divided into two main stages, namely: the frictioning stage and the forging stage. The frictioning phase is further divided into four phases and these will be described next.

Phase I: Sliding takes place between the unlubricated surfaces of the workpieces when the rotating workpiece makes contact with the stationary one. Strong adhesion junctions are formed at the areas of real contact, leading to the formation of metallic wedges [80]. The adhesion between the surfaces at some of the junctions is stronger than the metal on both sides and shearing takes place at a short distance from the interface. Fragments of metals are transferred from one surface to the other and vice versa. Since the rubbing speed is not uniform across the interface but increases linearly from zero at the centre to a maximum at the periphery, the size of the transferred fragments will not be uniform. The size will vary with the local rubbing speed, depending on the radius at which the fragments are formed, and also vary

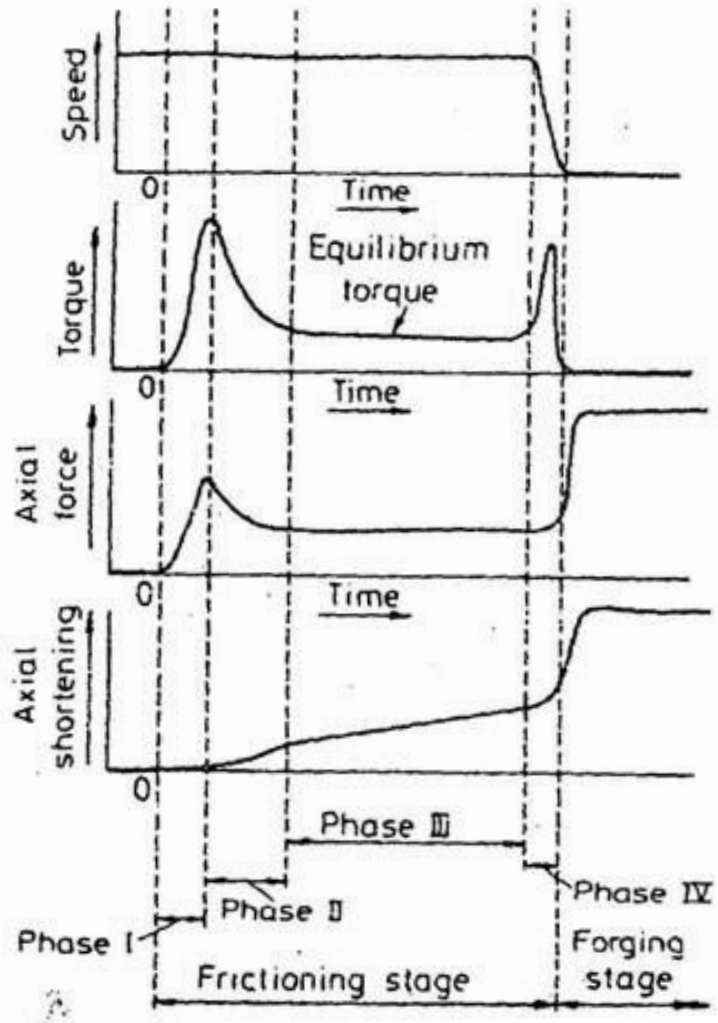


Figure 2 - 16: The variation of speed, torque, force and axial shortening during the welding cycle.

Source: *Wear* [79]. Reprinted from [79] with permission from Elsevier (8 December, 2010)

with the interfacial pressure. The resisting torque increases as a result of the interaction of surfaces. The process of rubbing, formation of wedges and transfer of fragments continue and, as a result, the temperature at the interface rises. The wedges and transferred fragments eventually coalesce with each other at high temperatures to form a continuous layer of hot severely plasticized material referred to as the plasticized layer. The formation of the plasticized layer results in decrease in the resisting torque, which ends phase I.

Phase II: This is the transition phase during which the metallic wedges and the transferred fragments at the interface transform into the plasticized layer. The plasticized layer gradually spreads across the interface and the resisting torque drops to an equilibrium value. It has been suggested that the temperature in the plasticized layer is high, and of the order of about 100-300⁰C below the bulk melting temperature of the material [77]. The material adjacent to the plasticized layer is heated by conduction. Phase II marks the commencement of axial shortening and formation of the weld collar (or flash).

Phase III: The interface is fully plasticized at the beginning of phase III, with the thickness of the plasticized layer being non-uniform across the section and varying depending on the applied pressure and the rubbing speed. The torque and the rate of axial shortening remain substantially constant. Also, the shape, location and dimension of the plasticized layer depend on the properties of the material being welded.

Phase IV: Deceleration takes place in phase IV. The plasticized region moves outward, radially, as the rotation speed decreases. The resisting torque rises until it reaches the terminal peak torque value, after which it decreases to zero as the speed also decreases to zero. At the end of phase IV, the material at the interface is ready for consolidation of the weld.

In the forging stage of continuous-drive friction welding, it is possible to choose welding conditions that would produce good welds using the same value of forging pressure as the frictioning pressure. However, situations arise where a continuous plasticized layer would not be produced by the selected choice of frictioning pressure and other parameters. A forging pressure, higher than the value of the frictioning pressure, is often required to produce joints of very high strength. The effect of the forging pressure is such that the plasticized layer spreads across the interface, closing any voids and also deforming the material in the heat-affected zone. This bonding mechanism has been suggested to be a “hot pressure welding” [77]. Continuous-drive friction welding of steels [81-83], titanium alloys [84], dissimilar aluminum alloys to steels [85, 86], and dissimilar nickel-base superalloys [87] have been reported in literature.

2.8.3 Linear Friction Welding

Linear friction welding is a relatively new friction welding process that was aimed at extending the existing applications of friction welding to non-axisymmetric components [88], which could be of similar or dissimilar materials. The major difference between this process and the two processes presented earlier is that, while inertia friction and continuous-drive friction welding processes involve heat generation under rotational-type motion, linear friction welding makes use of heat generated under a reciprocating linear

translational motion. In linear friction welding, one of the workpieces is held in a fixed position while the other workpiece reciprocates. The interfaces become softened by the frictional heat. The motion is subsequently stopped by aligning the moving workpiece with the stationary workpiece and a forging force is applied to fuse the workpieces together. Important parameters during linear friction welding includes: frequency and amplitude of oscillation, burn-off (or upset or axial shortening), and friction and forging pressures (or forces). Figure 2-17 is a schematic illustration of the basic principles of linear friction welding, which has been also described elsewhere [89]. Vairis and Frost [88] proposed four different stages in linear friction welding, similar to those that were suggested by Duffin and Bahrani [78]. According to Vairis and Frost, linear friction welding process involves four distinct phases represented by the schematic illustration shown in figure 2-18 [90].

Phase I; the initial phase: The two workpieces are brought into contact with each other under pressure. The surfaces begin to wear and the surface area of real contact increases. Heat is generated from solid friction as the parts rub against each other. There is no weld penetration or any noticeable axial shortening at this stage. If the rubbing speed is too low for a given axial force, the frictional heat generated will be insufficient to compensate for the conduction and radiation losses. This will eventually lead to insufficient thermal softening, which will prevent the next phase from occurring. However, if the parameters are chosen such that sufficient heat is generated at the interface, the real contact area approaches 100% and a plasticized layer begins to develop at the interface.

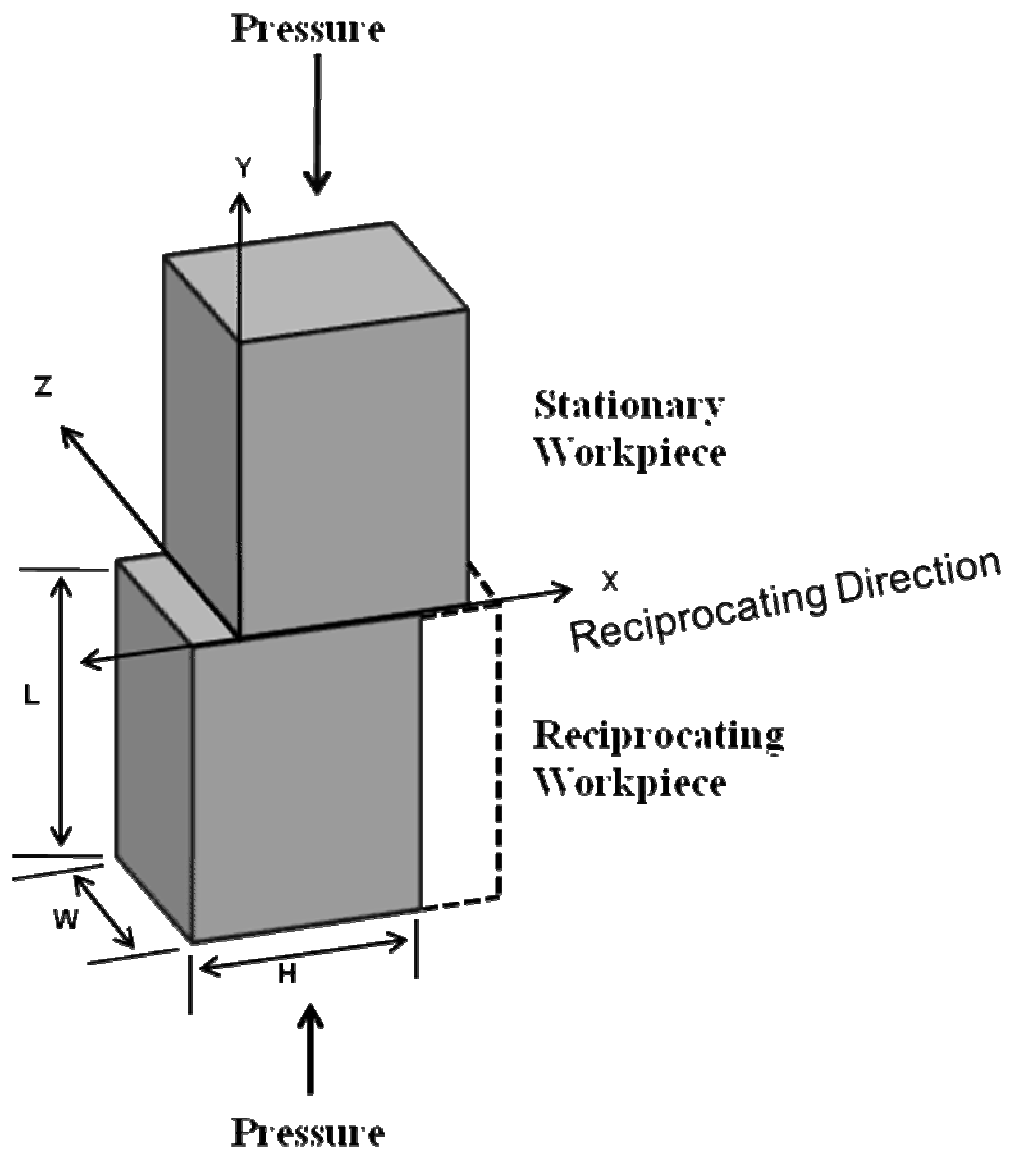


Figure 2 - 17: Basic principle of linear friction welding

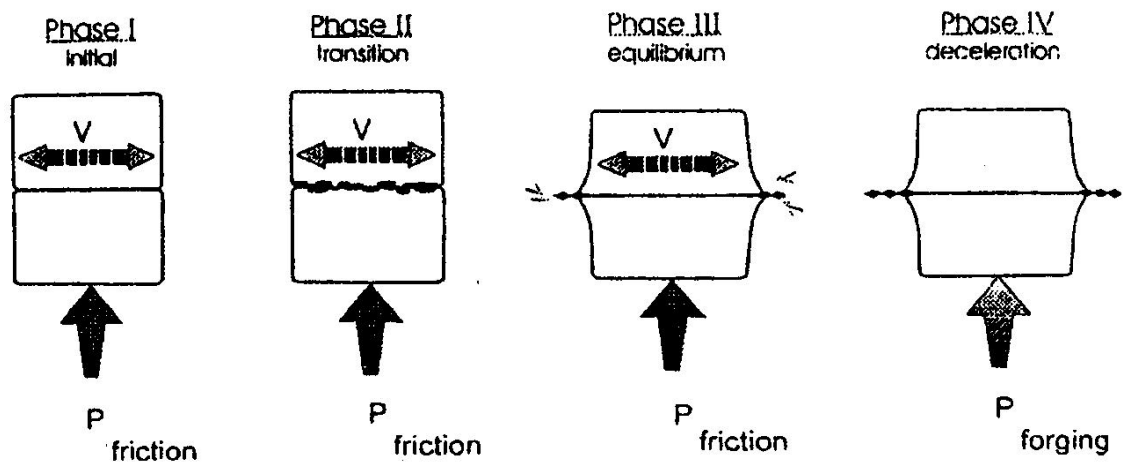


Figure 2 - 18: The four phases that characterize linear friction welding

Source: *Materials Science and Engineering A*. Reprinted from [90] with permission from Elsevier (29 November, 2010).

Phase II; the transition phase: As the sufficient heat softens the interface material and a sufficiently plasticized layer is being established, wear particles begin to get expelled from the interface. The real contact area is 100% at stage II, and the heat-affected zone expands. The soft plasticized layer formed between the two materials is no longer able to support the axial load, leading to phase III.

Phase III; the equilibrium phase: Axial shortening begins noticeably as a result of materials being expelled from the interface. The axial shortening varies approximately linearly with time. Materials continue to be extruded from the interface into the flash under the influence of high local stresses in the plasticized layer, assisted by the oscillatory movement of the workpieces. If the workpieces are aligned properly at the beginning of the process, the temperature distribution at the interface will be reasonably uniform. However, if the temperature increases excessively in one part of the interface, away from the centreline of oscillation, the plasticized layer becomes thicker in that section causing more plastic material to be extruded [88]. This can result in the rotation of the original plane and has been attributed to an original misalignment of the workpieces.

Phase IV; the deceleration phase: As soon as the desired axial shortening (or upset) is achieved, the two workpieces are brought to rest rapidly and a forging pressure may be applied to consolidate the weld.

Linear friction welding has been successfully used for copper, aluminum, stainless steels and titanium [91], as well as many alloys. In particular, linear friction welding of Ti6Al4V [88, 90, 92, 93], Al-Fe-V-Si alloy 8009 [94], polycrystalline nickel-base IN 718

superalloy [89] and dissimilar nickel-base RR1000 to single crystal nickel-base CMSX-4 [95] have been reported in literature. A thorough review of previous research on the application of linear friction welding process in joining different materials suggests that the joining of titanium alloys has received more attention. Active research is now ongoing on the use of linear friction welding in joining nickel-base superalloys.

2.8.4 Friction Stir Welding

Friction Stir Welding was invented in 1991 by The Welding Institute (TWI) [96], and has been considered as a promising joining technique in the aerospace industry as a replacement for traditional mechanical joining techniques such as riveting [97]. Arbogast [98] described the friction stir joining (or welding) process in details. In friction stir welding, a non-consumable, cylindrical pin tool (specifically designed for a given alloy) is rotated and plunged into the butt or lap joint of the material to be welded [99], as shown in figure 2-19 [98]. As the pin tool plunges into the weld joint line, the material is frictionally heated and plasticized at a temperature below the solidus and within the hot working temperature range. When the critical temperature and flow stress is reached, the tool is traversed along the weld joint. Metal flows to the back of the pin tool where it is extruded or forged behind the tool, consolidating and cooling under hydrostatic pressure. Friction stir welding differs from the previously described friction welding processes in that the frictional heat is generated by the tool rotation and contact between the workpieces and the pin rather than the actual rubbing together of the workpieces. The essential variables (or parameters) of friction stir welding are: the spindle speed, the travel speed and the penetration depth.

Distinct metallurgical processing zones have been identified during friction stir joining [98, 100], as shown in figure 2-19. The “*pre-heat zone*” ahead of the pin tool shows a temperature rise from the frictional heating of the spinning pin tool and the plastic strain energy released by the material. The extent and rate of heating in this zone is dictated by the material’s thermal properties and the forward travel speed of the pin tool. As the pin tool moves forward, an “*initial deformation zone*” forms where the material is heated above a critical isotherm so that the state of stress exceeds the critical flow stress of the material and flow commences. This material is forced both upwards into the “*shoulder zone*” and downward into the “*extrusion zone*”. In the “*extrusion zone*”, material from the front flows around the pin to the rear. Following the “*extrusion zone*” is the “*forging zone*” where the material from the front of the pin is forced under hydrostatic conditions into the cavity left by the forward moving pin tool. The shoulder of the pin tool helps to constrain material in this cavity and also applies a downward forging force. Material from the “*shoulder zone*” is dragged across the joint from the retreating side towards the advancing side. The last zone is the “*post-heat zone*”, where the material cools under either passive or forced cooling conditions.

In comparison to fusion welding processes, friction stir joining has been reported to offer simplified processing, improved mechanical properties, diminished weld defect formation, equivalent corrosion resistance, and reduced distortion, shrinkage and residual stresses [98]. The process enables aluminum, lead, magnesium, steel and copper to be welded continuously, with a non-consumable pin tool [101-103]. It can also be used to process other materials [104, 105].

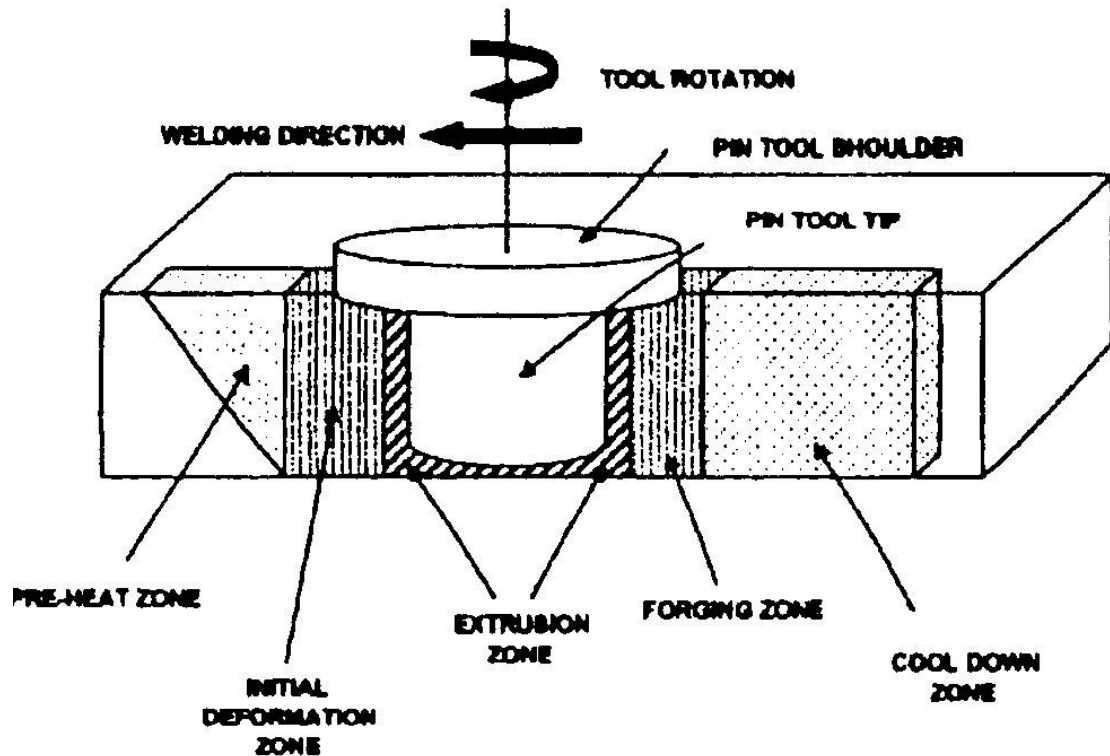


Figure 2 - 19: Metallurgical Processing Zones Developed During Friction Stir Joining.

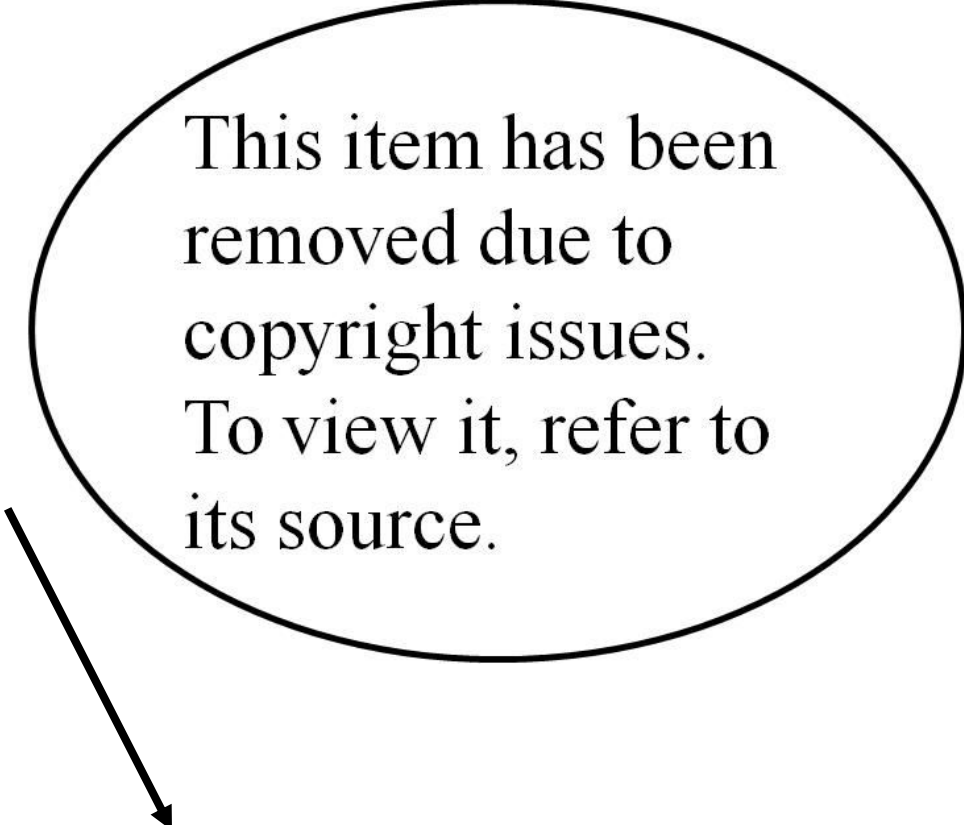
Source: Hot Deformation of Aluminum Alloys III [98]. Reprinted with permission from The Minerals, Metals and Materials Society (1 December, 2010).

2.9 Attractiveness of Friction Welding Processes

The attractiveness of friction welding can be viewed from both scientific and economic perspectives. Friction welding generally precludes the occurrence of some metallurgical phenomena associated with the fusion welding processes. Due to the fact that friction welding is believed to occur exclusively at sub-solidus temperatures, no fusion zone is associated with the process; therefore, the process avoids the usual weld fusion zone solidification cracking. Though a heat-affected zone (HAZ) is usually present in friction welds, with the choice of appropriate process parameters, HAZ cracking is usually avoided. Existing reports have suggested that none of the problems associated with fusion welding, such as microcracking and the presence of cast layers, are observed during friction welding [106]. The success of friction welding processes in producing crack-free welds has made the process attractive for joining crack-susceptible materials.

Studies have shown that metals of widely differing thermal and mechanical properties can be successfully joined by friction welding. Table 2.2 [70] contains different combinations of difficult-to-weld metals that can be successfully joined by inertia welding. It has been observed that combinations of materials that cannot be joined by other welding processes because of the formation of brittle phases that would make such joints unserviceable can be friction welded [70]. Also, joining at sub-solidus temperatures, coupled with relatively shorter weld times of friction welding, allows many combinations of metals to be joined. Friction welding processes have been used by Rolls-Royce to manufacture aero-engine components such as disc-to-disc, disc-to-shaft and shaft-to-flange combinations [106]. It is noteworthy that nickel-base alloys, specifically, which are known to be highly susceptible to HAZ liquation cracking are successfully

Table 2 - 2: Materials combinations that can be joined by inertia welding



This item has been removed due to copyright issues. To view it, refer to its source.

Source: Inertia Welding: Simple in Principle and Application [70]

weldable by friction welding as presented in table 2.2 [70]. Friction welding has been generally considered to be particularly well suited for joining nickel-base alloys and widely dissimilar metal combinations, producing crack-free welds with properties at, or approaching, 100% of parent material strength [106]. A report has been published by Pratt and Whitney [107] on the inertia friction welding of nickel-base superalloy, Waspaloy. Linear friction welding has also been reported to be of particular interest for aircraft engine applications, with potential to produce efficient joints in new components, such as, for the fabrication of aero-engine rings and bladed-integrated-disk (Blisk) assemblies, as well as for repair applications [88, 89, 95]. Currently, research is being carried out by several research groups on effective and efficient industrial utilization of linear friction welding in the manufacturing of aero-engine components that are not axially symmetrical, such as turbine disks and blades.

The basic reasons for the attractiveness of friction welding processes in aerospace industry applications for aero-engines are highlighted below:

1. Friction welding is a method that produces crack-free welds with good weld properties in difficult-to-weld alloys
2. The joint quality is more consistent than those of fusion welds [106]
3. Dissimilar metal combinations and the joining of non-axisymmetric parts are easily achieved
4. Lower cost owing to shorter weld time when compared with other processes, for example, electron-beam welding [106]

2.10 Scope and Objectives of the Present Study

The effectiveness of friction welding techniques in producing crack-free welds has been generally attributed to preclusion of grain boundary liquation in the HAZ during joining, since joining essentially occurs below the melting temperature of the bulk material. The process has been considered, like other friction welding processes, to be an exclusively solid state joining technology. S. V. Lalam et al [87] suggested that since the welding is performed in solid state, extensive migration of elements does not take place, and the welds are also free from segregation, porosity and liquation cracking that is common in conventional fusion welding. M. Karadge et al. [93] specifically mentioned that friction welding avoids melting and re-solidification processes, and gives rise to formation of a narrow HAZ due to extremely localized heat generation. Friction welding has also been regarded as a hot forging process in which local melting at the grain boundaries and microfissuring in the HAZ can be avoided [75].

The assumption of an exclusively solid-state process generally suggests crack-free joining of alloys by linear friction welding to be an exclusive solid-state phenomenon, where HAZ intergranular liquation cracking has become irrelevant. The occurrence of HAZ intergranular liquation cracking during fusion welding of IN 738 has been attributed to constitutional liquation of second phase particles, particularly the strengthening γ' phase, as discussed earlier. The liquid subsequently penetrates into the grain boundaries, forming a continuous liquid film. Tensile stresses generated during weld cooling cause decohesion along one of the solid-liquid interfaces, resulting in HAZ liquation cracking. However, researchers have claimed that crack-free welds are produced by friction welding because it is an exclusively solid state joining process.

Due to the success of friction welding processes in producing crack-free joints in some crack-susceptible aerospace alloys, the present work was initiated to investigate the weldability of the difficult-to-weld IN 738 superalloy by a variant of friction welding processes, linear friction welding (LFW), and to study the concomitant microstructural changes in the alloy due to the welding process.

The key objectives of the research were:

1. To determine if IN 738 can be successfully welded without cracking by Linear Friction Welding. This was to be done through a collaborative effort with the research personnel at the Aerospace Manufacturing Technology Centre of the Institute for Aerospace Research, National Research Council (NRC), Montréal, Canada.
2. To carry out a detailed study of the microstructural changes induced in the alloy by Linear Friction Welding.
3. To perform physical simulation of the welding process by using Gleeble thermo-mechanical simulation in order to adequately understand the microstructural development and resistance to cracking during joining.

The research to achieve the second and third objectives was to be done at the University of Manitoba by the author of this dissertation.

Chapter 3

Materials and Experimental Procedure

3.1 Materials Preparation

Cast IN 738, with a nominal composition given in table 3.1, was received from the Hitchiner Manufacturing Company in the form of plates having dimensions of 238 mm long \times 58 mm wide \times 14 mm thick. Specimens for linear friction welding (LFW), measuring 17.7 mm long \times 12.8 mm wide \times 11.1 mm thick, were machined from these plates by using a Hansvedt Model DS-2 travelling wire Electro-Discharge Machine. The linear friction welding specimens were given the standard solution heat treatment (SHT) at 1120°C for 2 hours in an argon-controlled atmosphere, followed by air-cooling. The surfaces of the solution heat-treated specimens were ground in order to remove surface oxides formed during heat treatment. The specimens were then welded at the Aerospace Manufacturing Technology Centre of the National Research Council of Canada's Institute for Aerospace Research in Montréal, as described in section 3.2. After welding, the welded specimens were sectioned in the axial direction perpendicular to the weld interface using the Hansvedt Model DS-2 travelling wire Electro-Discharge Machine and prepared for microscopy using standard metallographic techniques. The welded and machined specimens were electrolytically etched in 12mL H₃PO₄ + 40mL HNO₃ + 48mL H₂SO₄ solution at 6 volts for 5 seconds. In order to reveal the grain boundaries, sections of the welded specimen were etched with Kallings reagent (2 grams CuCl₂ + 33 mL HCl + 33 mL Methanol).

Cylindrical specimens, 10 mm in length by 6 mm in diameter, for Gleeble thermomechanical simulation, were cut from solution heat-treated plates using the

Table 3 - 1: Nominal composition of cast IN 738LC used in this study

Element	Weight Percent (wt%)
Carbon	0.11
Chromium	15.84
Cobalt	8.5
Tungsten	2.48
Molybdenum	1.88
Niobium	0.92
Iron	0.07
Aluminum	3.46
Titanium	3.47
Tantalum	1.69
Zirconium	0.04
Manganese	0.01
Silicon	0.01
Sulphur	0.001
Boron	0.012
Nickel	Balance

Electro-Discharge Machine. The surfaces of these specimens were also ground in order to remove surface oxides. Thermocouples were then spot-welded on each of these cylindrical specimens at the axial centre for temperature control and measurement during Gleeble simulation. All simulated materials were sectioned in the radial direction at the location of the thermocouples, using the Electro-Discharge Machine. These were then prepared using standard metallographic techniques and electrolytically etched in 12mL H_3PO_4 + 40mL HNO_3 + 48mL H_2SO_4 solution at 6 volts for 5 seconds.

3.2 Linear Friction Welding (LFW) of IN 738

The linear friction welding (LFW) of the solution heat treated materials were performed under the prevailing atmospheric conditions using a Linear Friction Welding Process Development System (PDS) located at the Aerospace Manufacturing Technology Centre of the Institute for Aerospace Research, National Research Council (NRC), Canada. The linear friction welder comprises of two hydraulic actuators, namely, the in-place actuator and the forge actuator. The in-plane actuator oscillates the lower workpiece in the horizontal direction and has a maximum capacity of 50kN frictional force, $\pm 10\text{mm}$ axial displacement, $\pm 5\text{mm}$ amplitude and 125Hz frequency. The forge actuator applies a downward load through the top stationary workpiece and has a maximum capacity of 90kN forging force and $\pm 6\text{mm}$ axial displacement. The PDS has a maximum weld time of 10 seconds. Other details on the technical specification of the equipment are described elsewhere [108].

3.3 Gleeble Thermomechanical Simulations

In order to study and decouple the effect of non-equilibrium thermal cycle and imposed compressive stress during the joining process, physical simulation of the LFW process

was performed by using Gleeble 1500-D Thermo-Mechanical Simulation System located at the University of Manitoba. All simulations were performed at a fast heating rate of $150^{\circ}\text{C}/\text{second}$ to temperatures ranging from 1100°C to 1250°C for different holding times followed by air cooling. The specimens simulated in order to study the effect of thermal cycle alone, without imposed stress, were heated to the peak temperatures and held for specific holding times ranging from 0.5 seconds to 30.5 seconds before air cooling. The specimens used to study the coupled effect of thermal cycle and imposed compressive stress were heated to the peak temperatures, while the holding times and the percent length reductions at the peak temperatures were varied.

3.4 Micro-hardness Measurement

Specimens were selected from the axially sectioned and polished linear friction welded materials for micro-hardness measurement. Micro-hardness profile from the weld interface to a distance of about 5mm into the base material was determined using a Buehler micro-hardness tester with a load of 300 grams.

3.5 Microscopy

Microstructures of the welded and Gleeble simulated specimens were examined and analyzed by a ZEISS Axiovert 25 inverted reflected-light optical microscope equipped with a CLEMEX vision 3.0 image analyzer (Clemex Technologies Inc., Longueuil, Canada), JEOL JSM-5900 scanning electron microscope (SEM) equipped with an Oxford (Oxford Instruments, Oxford, United Kingdom) ultrathin window energy-dispersive spectrometer (EDS) and Inca analyzing software, and JEOL JAMP-5900F Field Emission Scanning Auger Microprobe operating as a high resolution SEM. The characters and distribution of grain boundaries across the weld joint were examined by carrying out

electron backscatter diffraction (EBSD) based OIM scans (OIM is a trademark of TexSEM Laboratories Ltd), with the OIM attached to the JEOL JSM-5900 SEM. Special grain boundaries ($3 \leq \Sigma \leq 29$) were characterized based on the coincident site lattice (CSL) model. Random boundaries were those with rotation angles $> 10^\circ$ and CSL boundaries with $\Sigma > 29$.

Chapter 4

Results and Discussion

In this chapter, the results of an investigation of the weldability of IN 738 by LFW, and analysis of the microstructural changes induced by the welding process are presented and discussed. The chapter is divided into four major sections, which include

- 4.1 General microstructural analysis of pre-weld and linear friction welded specimens
- 4.2 Gamma prime (γ') precipitate dissolution behavior
- 4.3 Preclusion of intergranular liquation cracking
- 4.4 Other weld microstructural characteristics

4.1 General Microstructural Analysis of Pre-Weld and Linear Friction Welded Specimens

4.1.1 Introduction

The analysis of microstructural evolution during joining provides information about the response of the material to the joining process as well as the quality of joint obtained. In this section, a detailed analysis of the microstructural changes that occurred during the linear friction welding of IN 738 is presented. However, the starting microstructure of the base material is presented first as this plays a significant role in determining the microstructure of the welded material.

4.1.2 Pre-weld Microstructure

The SEM micrograph of pre-weld solution heat treated (SHT) material is presented in figure 4-1. These show a bimodal distribution of the strengthening γ' precipitates consisting of regular coarse primary γ' precipitates with sizes ranging from about 0.4 μm to 0.8 μm and fine spherical secondary γ' precipitates about 0.1 μm in diameter. The

solidification products that formed during casting [47, 48], namely MC carbides and γ - γ' eutectic were found to have persisted in the SHT material. Figure 4-1 shows MC carbides and γ - γ' eutectic, with the inset showing both the primary and secondary γ' precipitates. This type of constituents' distribution in SHT IN 738 has been observed by other researchers as well [109]. Significant changes in this pre-weld microstructure were found to occur during linear friction welding and this will be discussed next.

4.1.3 Microstructure of the Welded Material

Microscopic examination of the linear friction welded (LFWed) IN 738 using both optical microscopy and scanning electron microscopy (SEM) showed a sound and crack-free interfacial region, though IN 738 suffers cracking on welding by conventional fusion welding methods. Figure 4-2 is the optical micrographs of the joint while figure 4-3 is the SEM micrograph of the joint. Both figures show that no cracks were observed in the welded material. An overview of the linear friction welded joint revealed three different microstructural regions across the joint, shown in figure 4-4. These three regions, designated as regions 1, 2 and 3, correspond to the weld zone (WZ), the thermo-mechanically affected zone (TMAZ) and the heat affected zone (HAZ), respectively. They describe the microstructural changes that occurred in the welded material from the weld line region into the base material. Figure 4-4 also suggests that the microstructures obtained across the joint are symmetrical on both sides of the weld line.

4.1.3.1 Weld Zone (WZ) Microstructure

The weld zone (region 1), which formed at the interface between the two adjacent work pieces and extended to about 300 μ m into the material on either side of the joint, showed microstructural characteristics considerably different from that of the SHT specimen

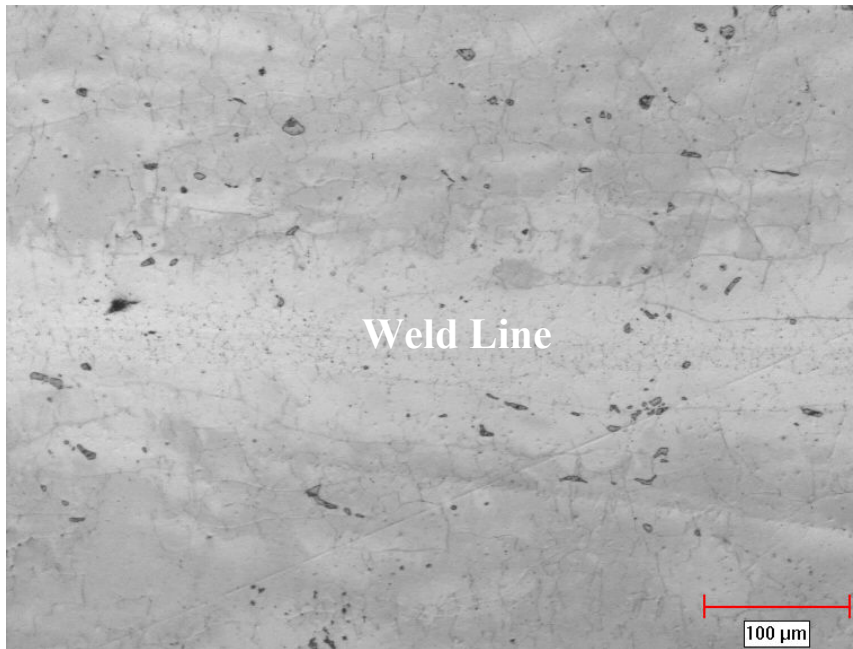


Figure 4 - 2: Optical micrograph of the linear friction welded joint

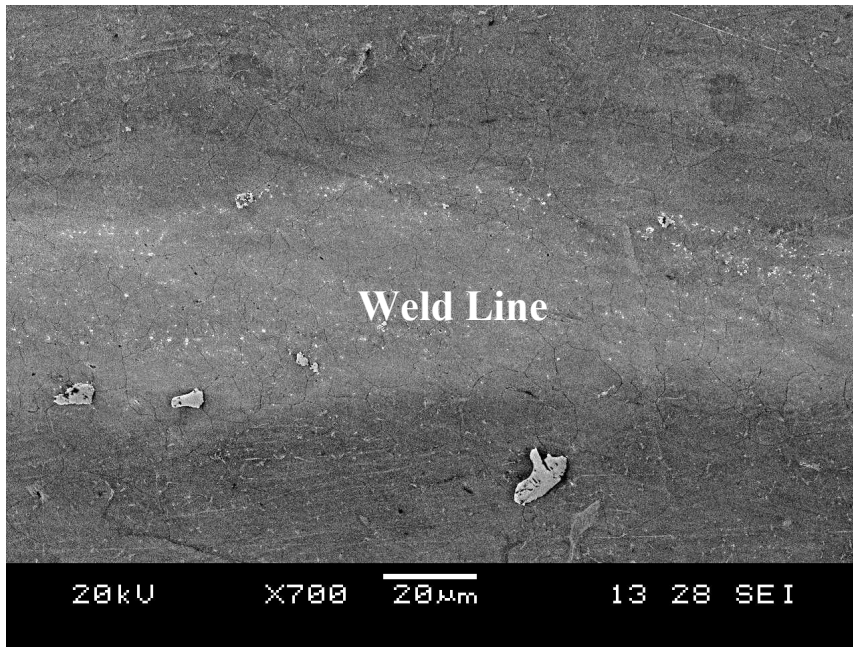


Figure 4 - 3: SEM micrograph of the linear friction welded joint

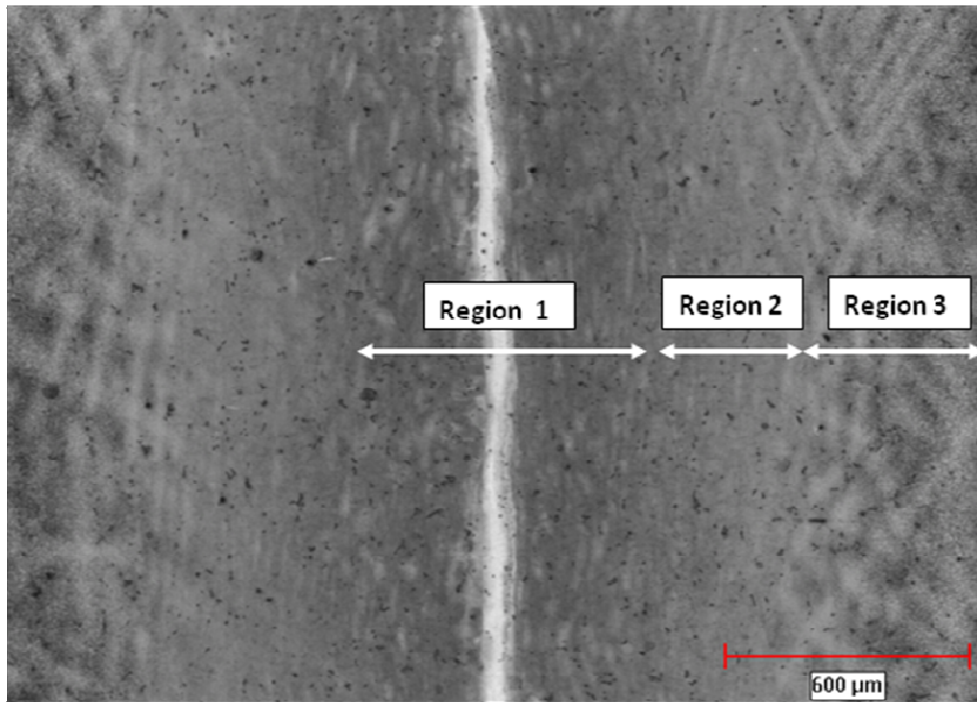


Figure 4 - 4: Optical micrograph showing an overview of three regions characterizing the joint microstructure

(figure 4-1) due to the thermo-mechanical processing that occurred during linear friction welding. SEM microstructure of this region, as illustrated by figure 4-3 and in the higher magnification figure 4-5, revealed that γ' precipitates, including γ - γ' eutectic constituents, completely dissolved during LFW, while MC carbides survived to the weld line. Another microstructural characteristic is the possible occurrence of recrystallization within the weld zone of the linear friction welded IN 738. A recrystallized microstructure along the weld line was previously observed in different Ni-based superalloys welded by frictional processes [72, 87, 89]. It has been suggested that the recrystallization occurs dynamically due to the thermomechanical conditions imposed during friction welding, namely the combination of high strain and strain rates at elevated temperatures. Figure 4-6 shows an optical micrograph of the recrystallized microstructure observed in linear friction welded IN 738. In particular, the maximum amount of plastic deformation would have occurred at the weld line which resulted in the formation of fine fully recrystallized grains. Traversing away from the weld line, the microstructural evolution increasingly exhibited regions of deformed or partially recrystallized grains, such that beyond 300 μm the recrystallization was localized along prior grain boundaries. Overall the observed marked changes in the microstructural characteristics (precipitates, carbides and grain size) are related to the steep gradients in the temperature and deformation conditions within the weld zone.

4.1.3.2 Thermo-mechanically Affected Zone (TMAZ) Microstructure

The thermomechanically affected zone (TMAZ), region 2, which is between 300 μm and 600 μm from the weld line, also exhibited a complete dissolution of the γ' precipitates and γ - γ' eutectic constituents, while the MC carbides remained. That is, the coarse and

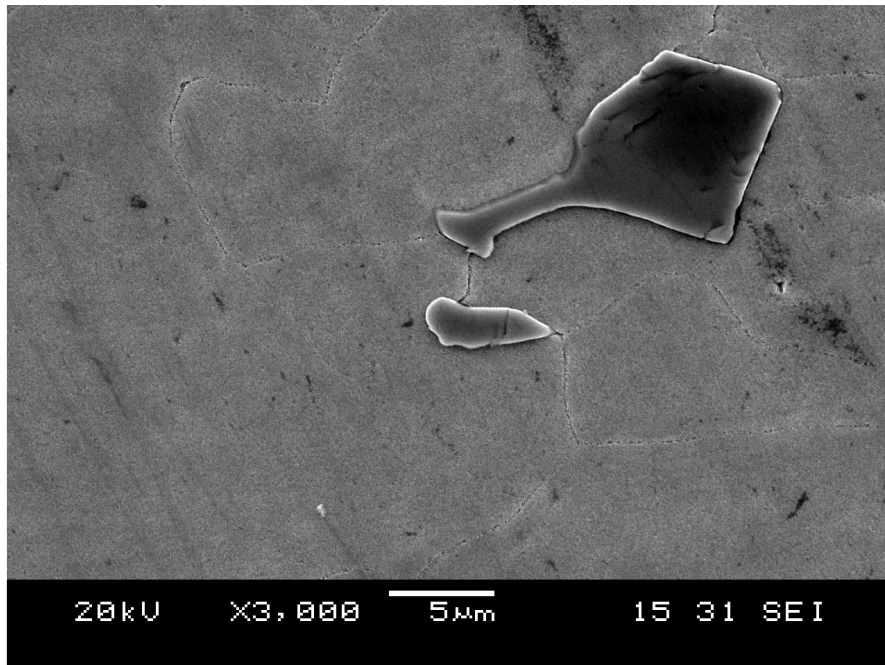


Figure 4 - 5: Higher magnification SEM micrograph of the weld zone, region 1

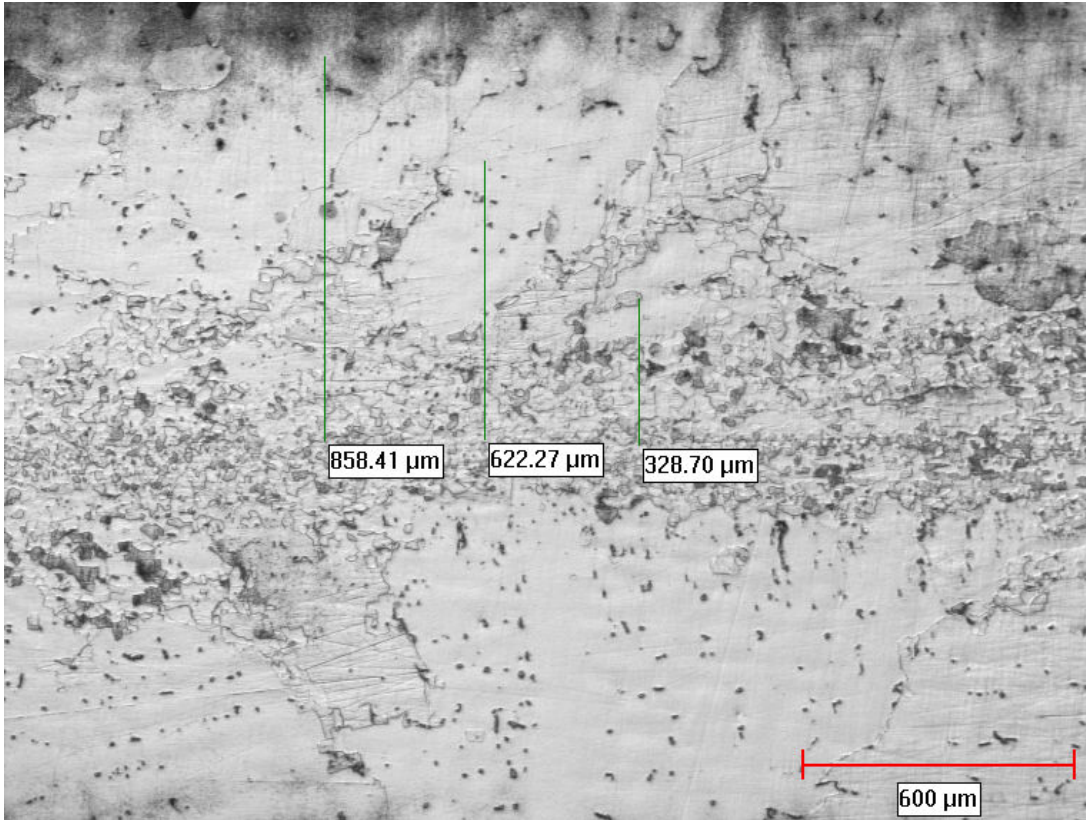


Figure 4 - 6: Optical micrograph showing recrystallization across the joint

secondary γ' precipitates, that were present in the pre-weld SHT IN 738, dissolved completely in both the weld zone and TMAZ, i.e. 600 μm from the weld line on either sides of the joint (figure 4-7). The main microstructural difference between the weld zone and the TMAZ is related to the recrystallization characteristics, in that, fully recrystallized grains formed in the weld zone, while recrystallization in the TMAZ was localized to prior grain boundaries. Higher magnification SEM studies suggested the presence of very fine γ' precipitates in both the weld zone and TMAZ, which formed during cooling of the weld. These very fine γ' particles contributed significantly to an increase in micro-hardness of the material close to the weld line, as indicated in Figure 4-8. Overall, the measurements show an increase in micro-hardness from that of the base material up to distances of about 2 mm from the weld line. The region within 600 μm from the weld line (weld zone and TMAZ), where complete γ' dissolution and reprecipitation of fine γ' particles occurred, correlates with the region where the highest hardness values were recorded. The hardness then decreased gradually with distance away from this region into the base material. These findings are in corroboration with previous work on dissimilar inertia friction welding of two Ni-based superalloys, namely, γ' strengthened alloy RR1000, and γ' and γ'' strengthened superalloy IN 718 [110]. Increase in hardness, due to the re-precipitation of very fine tertiary γ' particles during weld cooling of RR1000, was reported.

4.1.3.3 Heat Affected Zone (HAZ) Microstructure

In the HAZ, region 3, secondary γ' precipitates that were produced by the pre-weld SHT dissolved completely, while the primary γ' precipitates dissolved partially as revealed by the SEM micrograph of figure 4-9. Region 3 differs from regions 1 and 2 in that only a

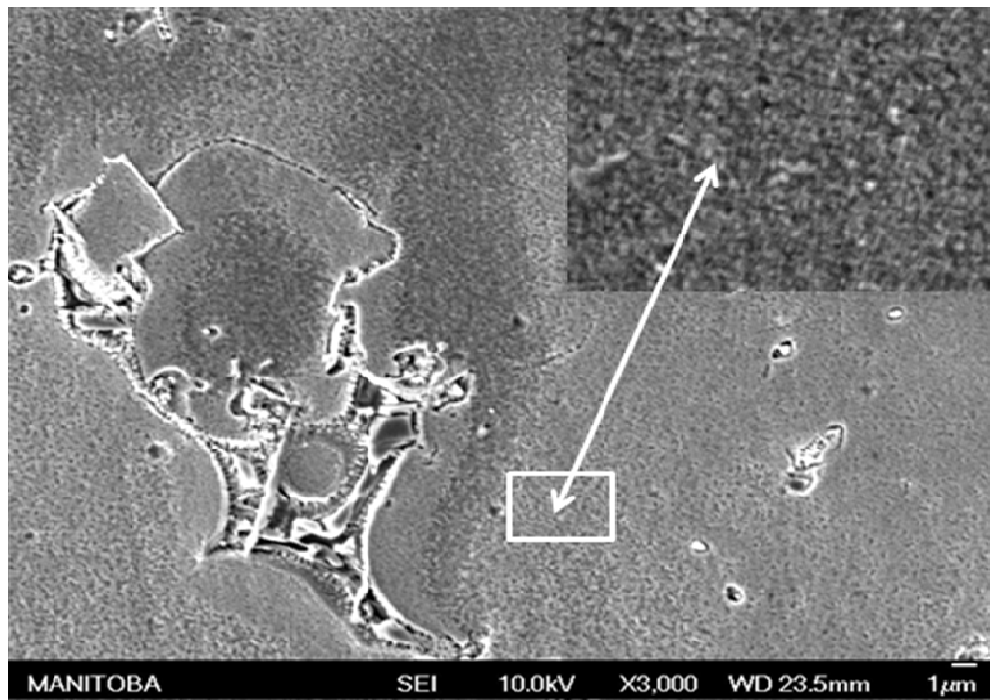


Figure 4 - 7: Auger SEM micrograph taken around 300 µm to the weld line

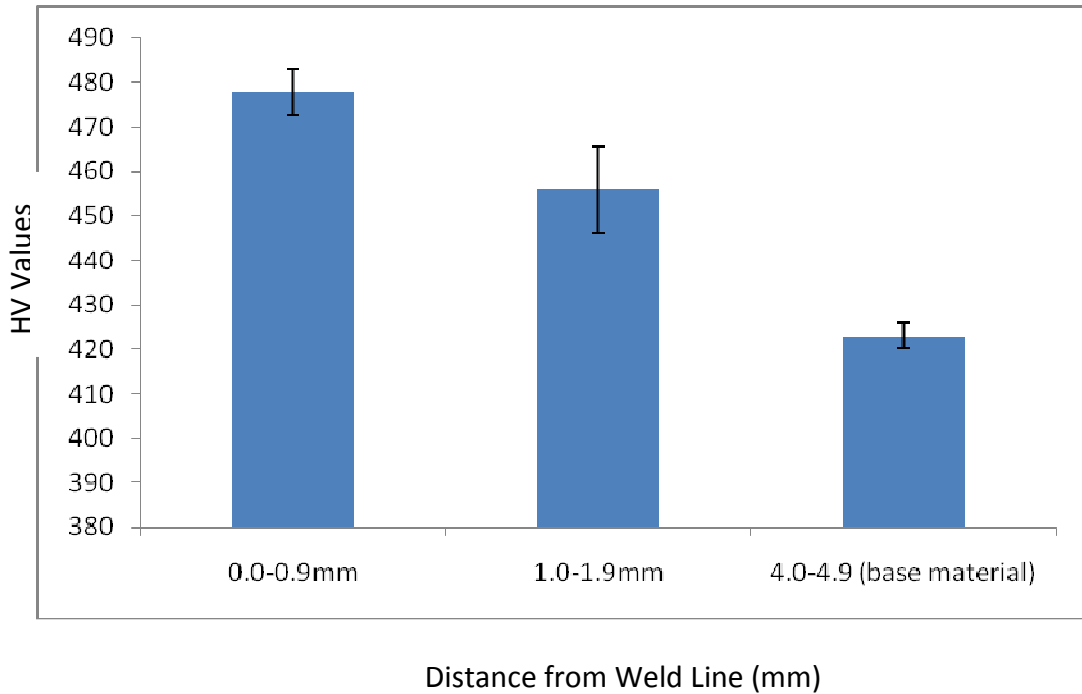


Figure 4 - 8: Micro-hardness values across the welded joint, which are average of values within a distance of 0 to 0.9 mm, 1.0 to 1.9 mm and 4.0 to 4.9 mm from the weld line. The region within the 4.0 to 4.9 mm was the base material.

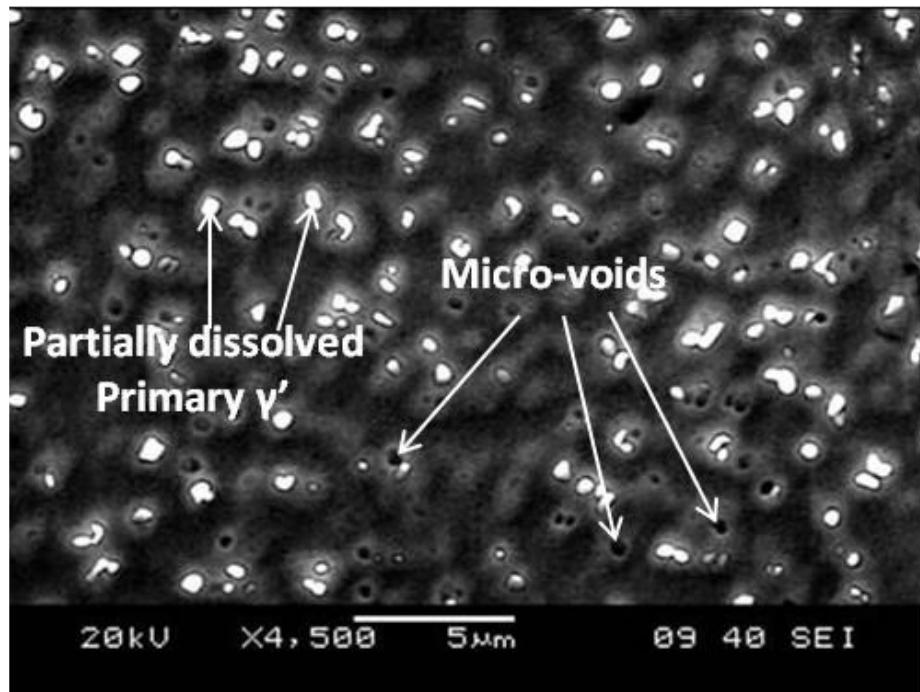


Figure 4 - 9: SEM micrograph of HAZ, region 3

partial dissolution of the coarse primary γ' precipitates was observed, which can be related to the temperature gradient that existed across the linear friction welded joint. No recrystallization was observed in the HAZ.

4.1.4 Intergranular and Intragranular Liquation in the Welded Material

A significant microstructural change that has not been reported to occur in linear friction welded materials is grain boundary liquation. Nevertheless, in the present study, intergranular and intragranular liquation were observed to have occurred in linear friction welded IN 738. Figure 4-10 is a SEM micrograph of the thermo-mechanically affected zone (TMAZ) showing an evidence of grain boundary liquation in the welded material. Evidence of intragranular liquation is also provided by the SEM micrograph of figure 4-11, which revealed the presence of resolidified fine γ - γ' eutectic products that formed from residual liquid during weld cooling. These intergranular and intragranular liquation were observed to be limited to the TMAZ, and were found to be present only in some areas. Evidence of grain boundary and intragranular liquation was not found in the weld zone. The weld zone appeared essentially free from resolidified products and other microstructural features that indicate prior occurrence of liquation reaction. It is a common knowledge that temperature gradient exists across the linear friction welded joint with the highest temperatures existing in the weld zone. The temperature decreases with distance away from the weld line, into the TMAZ and the HAZ, and subsequently into the base material. The existence of temperature gradient across the joint suggests that indications of liquation should be more evident in the weld zone in comparison to the TMAZ but this was not the case. Apart from the effect of temperature on the microstructural changes that occurred in the welded material, another variable that was

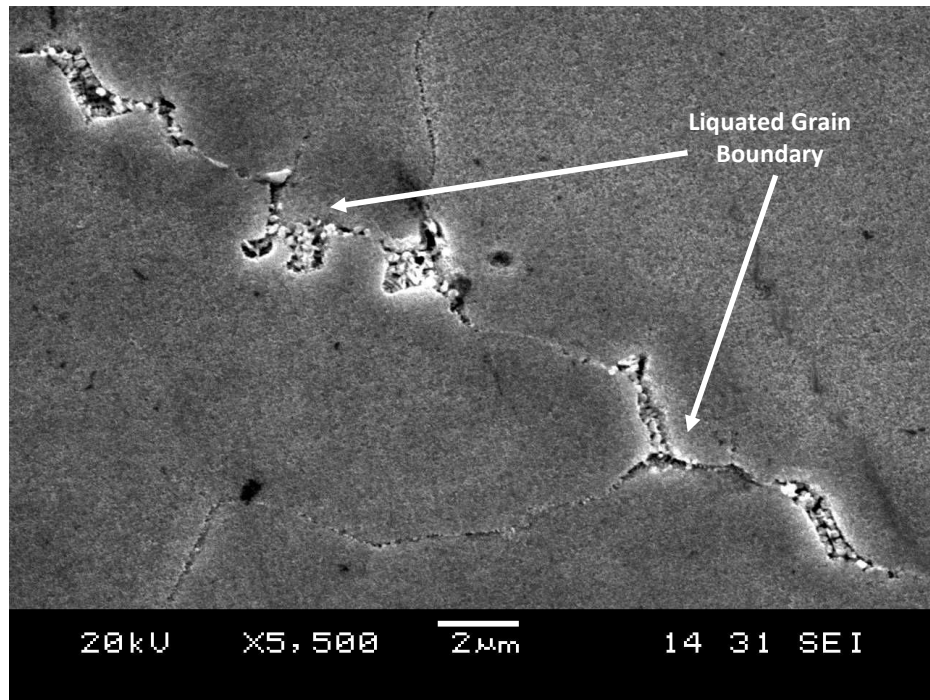


Figure 4 - 10: SEM micrograph showing liquation along grain boundaries of the linear friction welded material

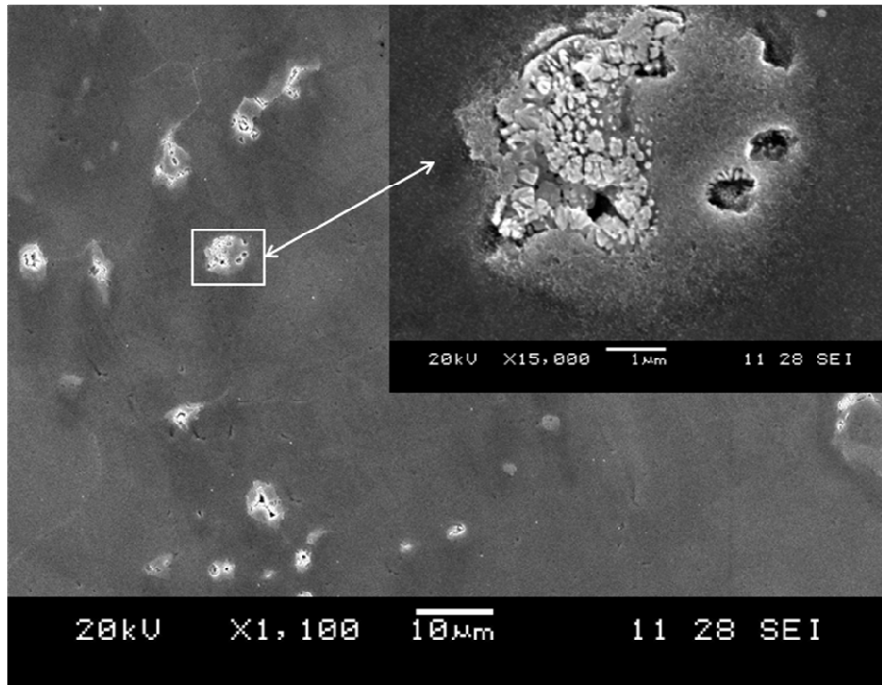


Figure 4 - 11: SEM micrograph of the TMAZ showing intragranular liquation

found to play a significant role in the observed microstructural development in this present work was the imposed external compressive stress.

In order to analyze and decouple the effects of these two variables, namely temperature and imposed stress, Gleeble thermo-mechanical simulation was performed on solution heat treated (SHT) IN 738. The simulation results provided further insight into microstructural developments during linear friction welding of IN 738 as will be discussed in the next section.

4.2 Gamma Prime (γ') Precipitate Dissolution Behaviour

4.2.1. Introduction

Microstructural observations described in the last section suggest that a principal transformation that significantly influenced the microstructural response of IN 738 to linear friction welding process, as has been generally recognized in other γ' strengthened nickel-based superalloys during friction joining [72, 110-112], is the dissolution of the strengthening γ' phase. In addition, γ' dissolution is generally used in theoretical models as an important parameter to predict maximum temperatures that different weld regions experience during friction welding [73, 111]. However, there are two salient factors that are generally neglected in the application of these models which, conceivably, could significantly affect the accuracy of the temperature predictions. Firstly, an exclusive solid-state dissolution of γ' precipitates is normally assumed, which may cease to hold if the particles survive to temperatures where they could react with the surrounding matrix to produce a liquid phase. Secondly, a possible influence of considerable imposed compressive stress, that induces compressive strain in the material being welded, on the degree of particle dissolution is not usually considered. In this present work, the results of

Gleeble simulation experiments performed in order to understand the effects of rapid heating, temperature changes, holding times, and coupled effect of temperature and imposed external stress-induced compressive strain on γ' particles dissolution will be presented and discussed next.

4.2.2 Non-Equilibrium γ' Particle Dissolution under Rapid Thermal Cycle

The dissolution of $\text{Ni}_3(\text{Al,Ti})$, γ' , particles generally requires dissociation of the constituent atoms from the precipitate at the matrix/precipitate interface, followed by their diffusion away from the interface into the matrix. Under an extremely slow heating rate, corresponding to an equilibrium condition, it is expected that, as the temperature increases, the solubility of γ' forming elements in the matrix will increase gradually. In this case, γ' particles will dissolve with increasing solute solubility such that the last remaining γ' particles will dissolve completely, by solid-state dissolution, at the equilibrium solvus temperature of the particles. However, the rapid thermal cycle usually experienced during friction welding departs significantly from equilibrium. Previous studies have suggested that heating rates during friction welding can be of the order of 200 to 300⁰C per second and higher, depending on distance from the weld interface [111]. Under rapid heating, the overall rate of dissolution of γ' particles will occur at a finite rate, which can be controlled by either or both of the dissociation and diffusion processes [40]. An attempt has been made to model particle dissolution under rapid heating conditions by analytical technique based on an isokinetic and additivity concept and also by numerical calculations [113]. The results of the two methods, which were found to be in good agreement, show that the degree of particle dissolution depends on an interplay between the heating rate and the initial particle size. Soucail et al. [111] in a

separate work studied dissolution of γ' phase in a nickel-based superalloy at equilibrium and under rapid heating conditions. Following a different analytical approach developed by Ashby and Easterling [114], they derived a particle dissolution model and verified it with experimental results. Their analytical results, which were reported to be in good agreement with the experimental results, are qualitatively consistent with those of Bjorneklett et al. [113]. They showed that there was a significant departure from equilibrium dissolution behaviour under rapid heating conditions, in that the temperature of complete dissolution of γ' particles increased with increasing heating rate and the extent of the departure was dependent on the initial particle size. The increase in complete dissolution temperature was found to be more pronounced with increase in particle size. An increase of about 120°C in the complete γ' dissolution temperature at a heating rate of 8°C/s was reported for γ' precipitates with an initial size of 0.8 μm . Similar effect of heating rate on γ' solvus temperature has also been observed by DTA studies [115]. Therefore, depending upon the initial particle size and heating rate, limited integrated time available for homogenization by diffusion process during continuous heating can cause γ' precipitate particles in nickel-based superalloys to persist to temperatures well above their equilibrium solvus temperature. The result of the effect of rapid heating on γ' particles dissolution in this present work is presented by the SEM micrographs of Gleeble-simulated materials in figure 4-12. At a fast heating rate of 150°C/second and a holding time of 0.5 seconds, γ' precipitates survived up to temperatures above their equilibrium solvus of around 1160°C. The micrographs shown in figures 4-12a, 4-12b and 4-12c show that the precipitates survived up to 1250°C. The precipitate size also decreased with an increase in temperature. Figures 4-12d and 4-12e

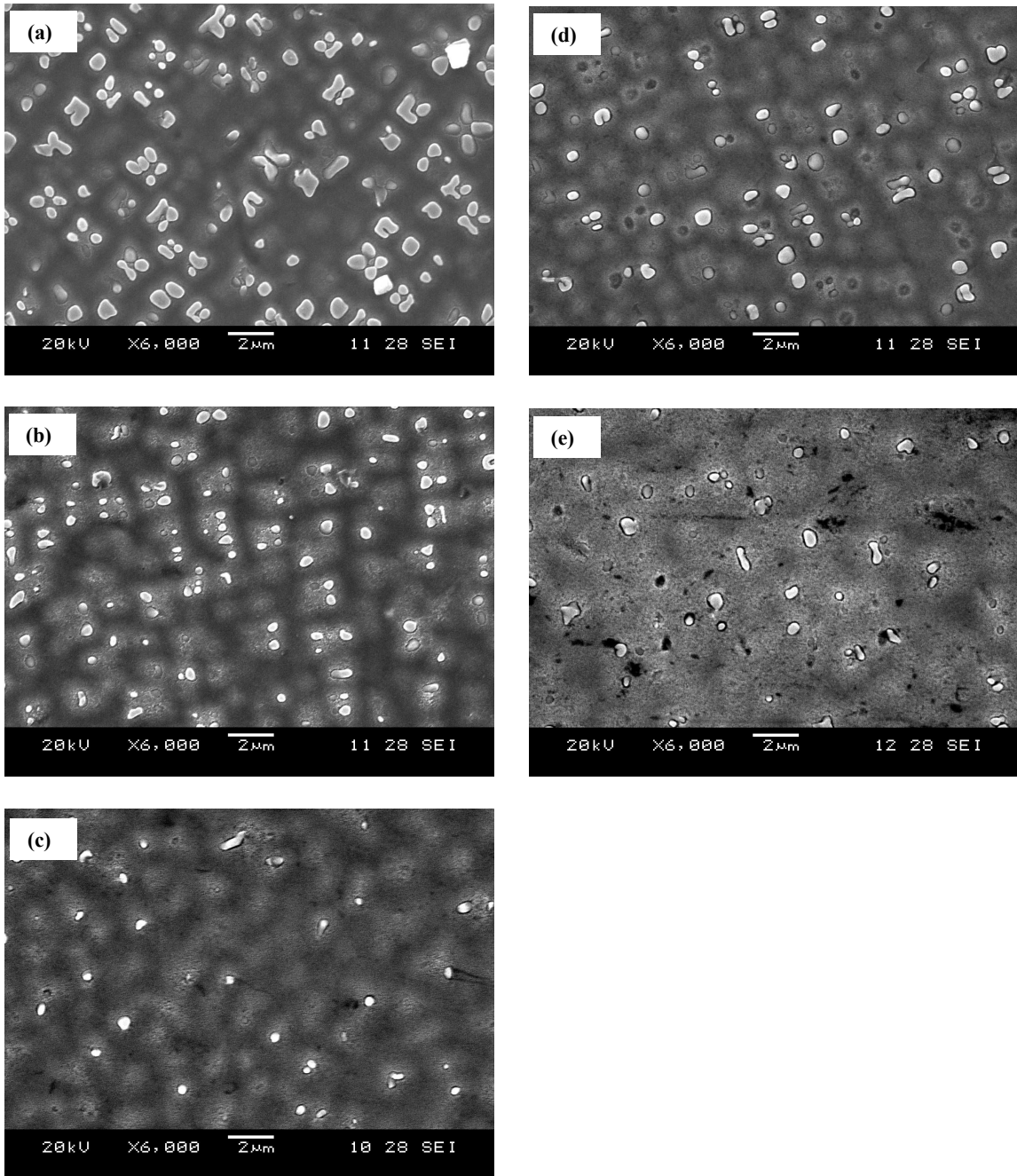


Figure 4 - 12: γ' precipitate dissolution under rapid thermal cycle (heating rate of $150^{\circ}\text{C}/\text{sec}$): 0.5sec holding time at peak temperatures of (a) 1170°C , (b) 1200°C and (c) 1250°C , and (d) 1.5sec holding time at 1170°C (e) 3.5sec holding time at 1170°C , followed by air cooling

also show that the precipitate size decreased with isothermal holding at 1170⁰C. This result is in agreement with studies performed by other researchers [111] on the dissolution of γ' phase in a γ' -strengthened nickel-base superalloy, where, under a rapid heating rate of 300⁰C/s and holding time of 0.5 seconds, the reported solvus of primary γ' particles in the alloy was found to be 1265⁰C instead of 1140⁰C at equilibrium. However, possible consequence of the survival of γ' precipitates to temperatures well above their equilibrium solvus temperature is often neglected.

The dissolution of second phase precipitates during linear friction welding has generally been assumed to occur by a solid-state dissolution process, due to the fact that the peak temperature reached during joining is usually below the equilibrium solidus temperature of the base material. γ' precipitates, in particular, which are the main strengthening phase of precipitation hardened nickel-based superalloys, have been generally reported to undergo solid-state dissolution during friction welding [111]. However, the survival of γ' precipitates to temperatures above their equilibrium solvus under rapid heating during LFW can lead to non-equilibrium phase reactions below the solidus temperature. Notable among these is a non-equilibrium eutectic-type reaction between second phase precipitates and the matrix to produce a metastable liquid through a phenomenon known as constitutional liquation. Pepe and Savage [40] have proposed that existence of second phase intermetallic particles at a temperature where they could react with the matrix by a eutectic-type reaction will result in constitutional liquation. There exists a range of temperature in γ' precipitation-hardened nickel-based alloys within which γ - γ' eutectic reaction occurs, and persistence of γ' particles to this temperature range during continuous heating could result in their constitutional liquation [116]. In IN 738, γ - γ'

eutectic transformation has been reported to occur over a range of temperatures, which could be below 1180°C [17]. In this present work, the results of Gleeble simulation of the welding thermal cycle showed that γ' particles survived well above their solvus temperature to peak temperatures of up to 1250°C. This consequently resulted in their constitutional liquation and subsequent contribution to grain boundary liquation. The occurrence of grain boundary liquation as a result constitutional liquation of γ' precipitates in Gleeble-simulated specimens is illustrated in figure 4-13. The extent of grain boundary liquation increased with increase in the peak temperature from 1170°C to 1200°C as shown in figures 4-13a and 4-13b, respectively. In addition to Gleeble simulations using solution heat-treated materials, some as-cast material was also subjected to linear friction welding thermomechanical cycle. Figure 4-13c shows grain boundary liquation as a result of constitutional liquation of γ' precipitates in cast IN 738 at 1180°C. The observation of grain boundary phases and intragranular phases liquation in the welded material, as earlier explained and presented in figures 4-10 and 4-11, is in agreement with the results of the Gleeble simulation. It is known that a differentially etching thin film connecting γ' particles is an evidence of constitutional liquation [116]. A careful microstructural analysis of the HAZ of linear friction welded IN 738 superalloy revealed that constitutional liquation of γ' precipitates occurred during joining (figure 4-9). Constitutional liquation of γ' particles was observed to have contributed to grain boundary liquation in the welded material and some intergranular regions exhibited liquid film migration features. These observations suggest that the mode of dissolution of γ' precipitates at any location across the welded joint during LFW depends on the peak temperature reached, the heating rate experienced by the alloy at that particular location

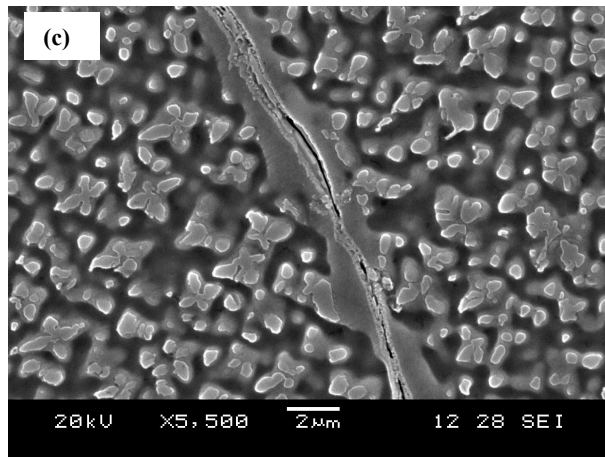
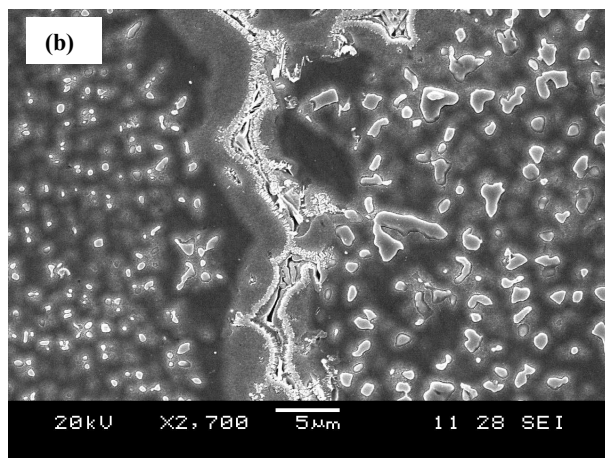
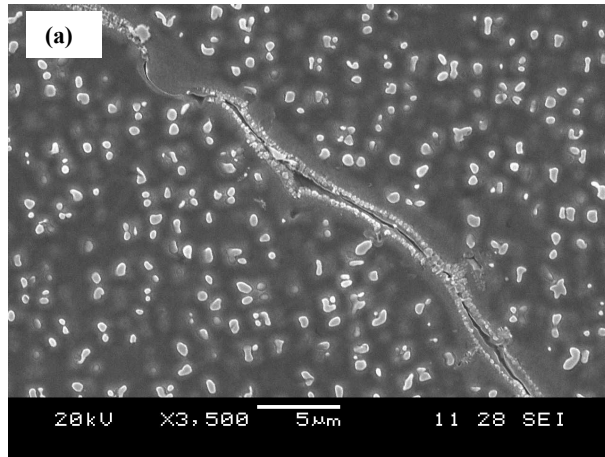


Figure 4 - 13: SEM micrographs showing grain boundary liquation in Gleeble-simulated specimens heated at 150⁰C/sec and held for 0.5sec at (a) 1170°C (b) 1200°C and (c) 1180°C (cast material), followed by air cooling

and the γ' particle size. Far away from the weld interface, where the peak temperature reached during welding was below γ' liquation temperature, the precipitates likely dissolved by solid-state dissolution. However, in regions closer to the weld interface where there was a combination of both rapid heating and higher temperatures, the precipitates dissolved essentially by liquation reaction.

Aside from the thermal effects on γ' precipitate dissolution during LFW, another factor that can significantly influence the degree to which the precipitates dissolved during joining is the imposed compressive stress, which induces compressive strain in the material. Generally, the possible influence of compressive strain on the thermodynamics of precipitate dissolution during friction welding has received little attention and this will be addressed next.

4.2.3 Strain-Assisted Dissolution of γ' Precipitates

Previous reports on the microstructure of friction welded joints have focussed mainly on the effect of temperature on phase reactions. For example, the dissolution of γ' precipitates during friction welding of nickel-base superalloys and the resulting changes in mechanical properties have been explained on the basis thermal cycle alone [110]. Microstructural evolution during friction welding of another structural alloy has also been mainly related to temperatures at which those transformations are expected to occur [92]. In a model developed for the dissolution of γ' precipitates during friction welding of a precipitation-hardened nickel-base superalloy, the solvus temperature and the volume fraction of γ' precipitates were predicted on the basis of dissolution under thermal cycle alone [111]. Though the model was very useful in describing non-equilibrium dissolution behaviour of the precipitates under rapid heating conditions, it did not consider the

possibility of compressive strain aiding the dissolution kinetics of the precipitates. A generally accepted model for the dissolution of spherical second phase particles in binary systems was developed by Whelan [117]. The model was used to evaluate the diffusion flux of solute out of the spherical precipitate of radius R, and assumed the diffusion field around the precipitate to be the same as what would exist if the radius of the particle, and hence the precipitate/matrix interface is fixed at R position. Whelan's model is given by [117]:

$$\frac{dR}{dt} = -\frac{kD}{2R} - \frac{k}{2} \sqrt{\frac{D}{\pi t}} \dots\dots\dots(4.1)$$

D is the diffusivity of solute atoms in the matrix, t is the time taken and k is given by [117]:

$$k = \frac{2(\rho_s - \rho_e)}{(\rho_c - \rho_s)} \dots\dots\dots(4.2)$$

where, ρ_c is the solute concentration inside the precipitate, which is initially in equilibrium with a uniform concentration ρ_e of solute in the matrix and ρ_s is the equilibrium surface concentration at time $t=0$ when the temperature is raised by ΔT . According to Whelan [117], the D/R term on the right hand side of equation 4.1 arises from the steady state part of the diffusion field, while the $t^{-1/2}$ term arises from the transient part. Apart from the assumption of a stationary interface in obtaining the concentration gradient in the matrix, Tundal and Ryum [118] pointed out another important assumption in the model developed by Whelan. The diffusivity, D, was assumed to be independent of concentration. Since most experiments performed to study the dissolution of second phase particles involve only thermal treatments, it can be assumed that solute diffusivity, D, depends mainly on both temperature and concentration

alone. However, during thermal cycle under frictional processes such as obtained in linear friction welding, the thermodynamics of diffusion-controlled phase reactions does not depend on temperature and concentration changes alone but also on the externally stress-induced compressive strain. The model developed by Whelan (equation 4.1) suggests that any factor that can increase the solute diffusivity, D , in the matrix will ultimately increase the dissolution rate.

The diffusivity, D , is temperature dependent, as given by the Arrhenius equation:

$$D = D_o \exp\left(\frac{-Q}{kT}\right) \dots\dots\dots(4.3)$$

D_0 is the pre-exponential factor, Q is the activation energy for diffusion, k is the gas constant and T is the absolute temperature. Generally, more attention has been given to the effect of temperature on diffusion rate such that it is possible to erroneously assume that the activation energy for diffusion at a given temperature is constant. For the vacancy-assisted diffusion, equation 4.3 can be expanded to [119]:

$$D = \frac{1}{6} d^2 Z v \exp\left[\frac{(\Delta S_f + \Delta S_m)}{k}\right] \exp\left[\frac{-(\Delta H_f + \Delta H_m)}{kT}\right] \dots\dots\dots(4.4)$$

Where, d is the inter-atomic distance, Z is the coordination number, v is the vibrational frequency of an atom along its reaction path, ΔS_f and ΔS_m are the vacancy formation and migration entropies respectively, and ΔH_f and ΔH_m are the vacancy formation and migration enthalpies respectively. The first exponent and the parameters before it represent D_0 in equation 4.3, while $(\Delta H_f + \Delta H_m)$ of the second exponent represents the activation energy, Q . The enthalpy change, ΔH , is dependent on both temperature and pressure. Consequently, the activation energy for diffusion, Q , at a given temperature, T , is dependent on pressure. The dependency of Q on pressure implies that the diffusivity,

D, is dependent on pressure. Hence, it is conceivable that kinetics of microstructural transformations in solids that are controlled by atomic diffusion can be affected by both the magnitude and sign of externally imposed stress/strain. Through a rigorous and meticulous analytical study, a relationship between activation energy per unit strain, Q' , and diffusion coefficients under strain, $D(\text{strain})$, and without strain, $D(\text{relax})$ has been given by [120];

$$D(\text{strain}) = D(\text{relax}) \exp\left(\frac{-Q's}{kT}\right) \dots\dots\dots(4.5)$$

where, s is the strain (negative for compression and positive for tension), k is a constant and T is the absolute temperature. It can be seen from equation 4.5 that atomic diffusion can be enhanced by compressive strain and reduced by tensile strain. This has been experimentally confirmed in SiGe material, where diffusion increased under compression but decreased under tension [121]. A similar variation in diffusion was observed in a Cu-Si couple [122] where the application of compressive stress resulted in a significant increase in diffusion.

In the present work, the dissolution of γ' precipitates, which is typically known to be controlled by diffusion of γ' forming elements away from the precipitate/matrix interface, was observed to be significantly enhanced by externally induced compressive strain. In the experiments performed to study the coupled effect of thermal cycle and externally imposed compressive stress on γ' precipitate dissolution in IN 738, two different temperature regimes were considered. In the first regime, the temperatures were below the equilibrium solvus of the precipitates (about 1160°C), where the precipitates are expected to dissolve by solid-state reaction, while the second regime was above the

solvus temperature, where the precipitates will dissolve by liquation reaction. Figures 4-14a and 4-14b show SEM micrographs of Gleeble-simulated materials heated to 1110⁰C at 150⁰C/sec and held for 20.5sec, followed by air cooling. The specimen in figure 4-14a was under thermal cycle alone while the specimen in figure 4-14b was stressed to 20% compressive strain during holding at the peak temperature. The degree of precipitate dissolution in the stressed specimen (figure 4-14b) was greater than that of the specimen under thermal cycle alone (figure 4-14a). A similar result was obtained when the peak temperature was increased from 1110⁰C to 1150⁰C. Figures 4-15a and 4-15b are SEM micrographs of Gleeble-simulated materials heated to 1150⁰C at 150⁰C/s and held for 10.2 seconds, air-cooled. The degree of dissolution observed in the specimen stressed to 20% compressive strain (figure 4-15b) was also observed to be more than that under temperature alone (figure 4-15a).

Above the equilibrium solvus temperature of the precipitate, where γ' liquation was observed to occur, the liquid film produced by reaction between γ' and the matrix was observed to be rapidly eliminated by compressive strain. It is known that non-equilibrium intragranular liquid can isothermally re-solidify through solid-state back-diffusion of solutes away from the liquid phase [123]. The enhanced diffusivity of solute atoms in the matrix by an externally imposed compressive strain, as explained earlier, suggests an increased rate of back diffusion of solutes away from the liquid phase surrounding the precipitates into the adjacent γ matrix, resulting in faster elimination of liquid produced by γ' liquation. Figure 4-16a and 4-16b are SEM micrographs of Gleeble-simulated materials heated to 1170⁰C at the rate of 150⁰C/sec and held for 1.5 sec, followed by air

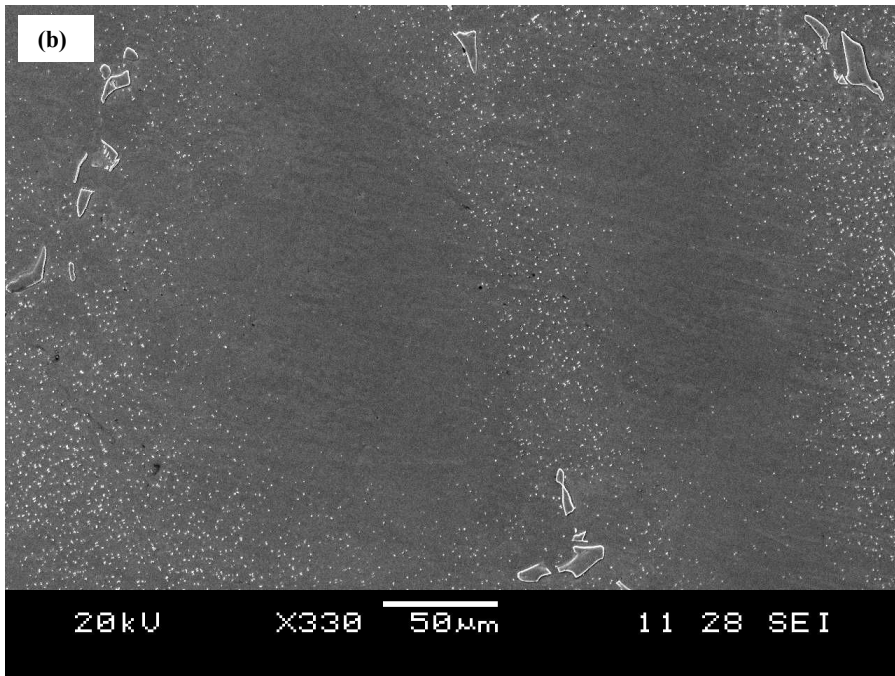
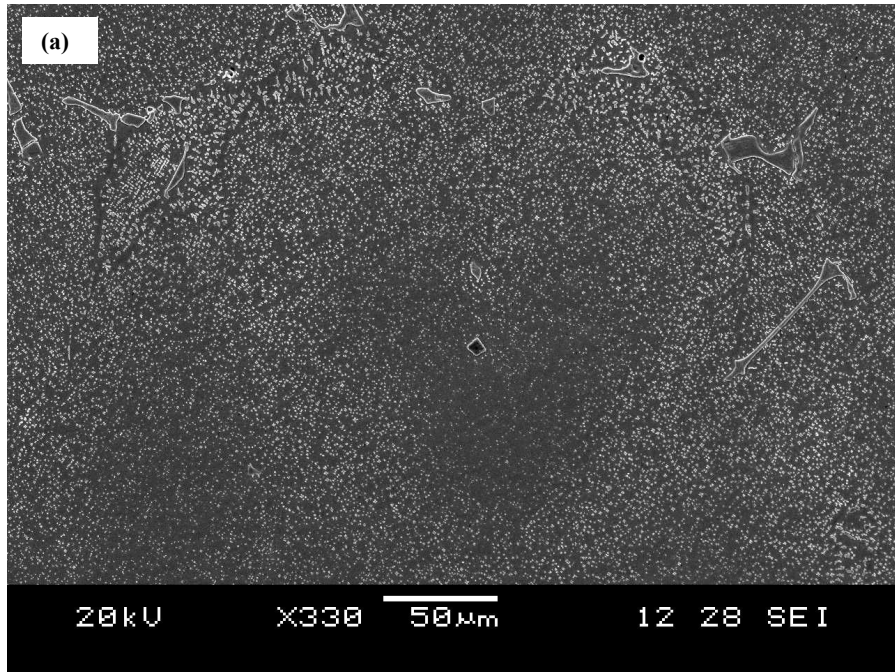


Figure 4 - 14: Specimens heated to 1110⁰C at 150⁰C/s and held for 20.5 seconds, followed by air cooling, (a) thermal cycle alone, (b) strained to 20% length reduction at peak temperature

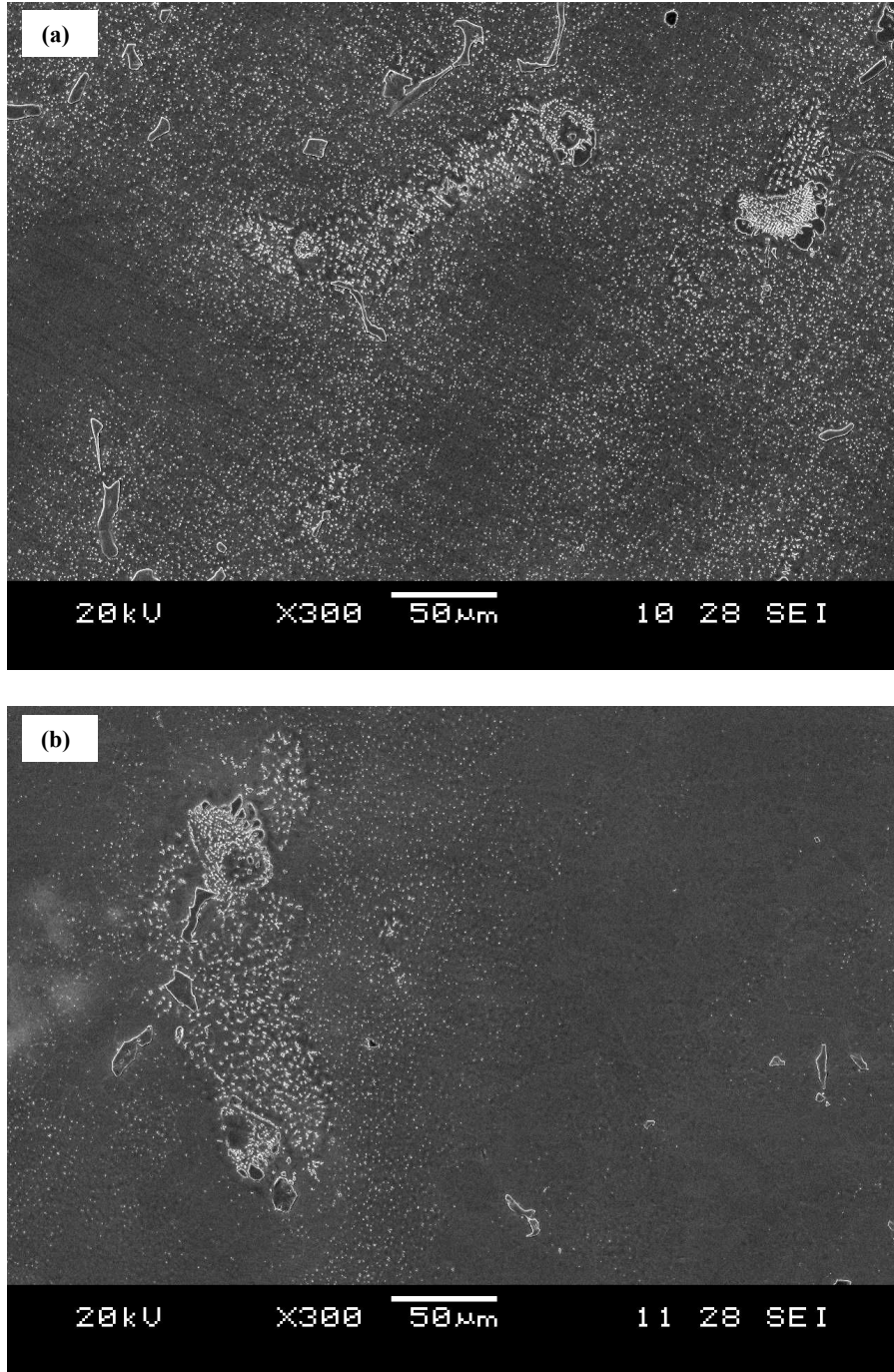


Figure 4 - 15: Gleeble-simulated specimens heated to 1150⁰C at 150⁰C/s and held for 10.5 seconds, followed by air cooling, (a) thermal cycle alone, (b) strained to 20% length reduction at peak temperature

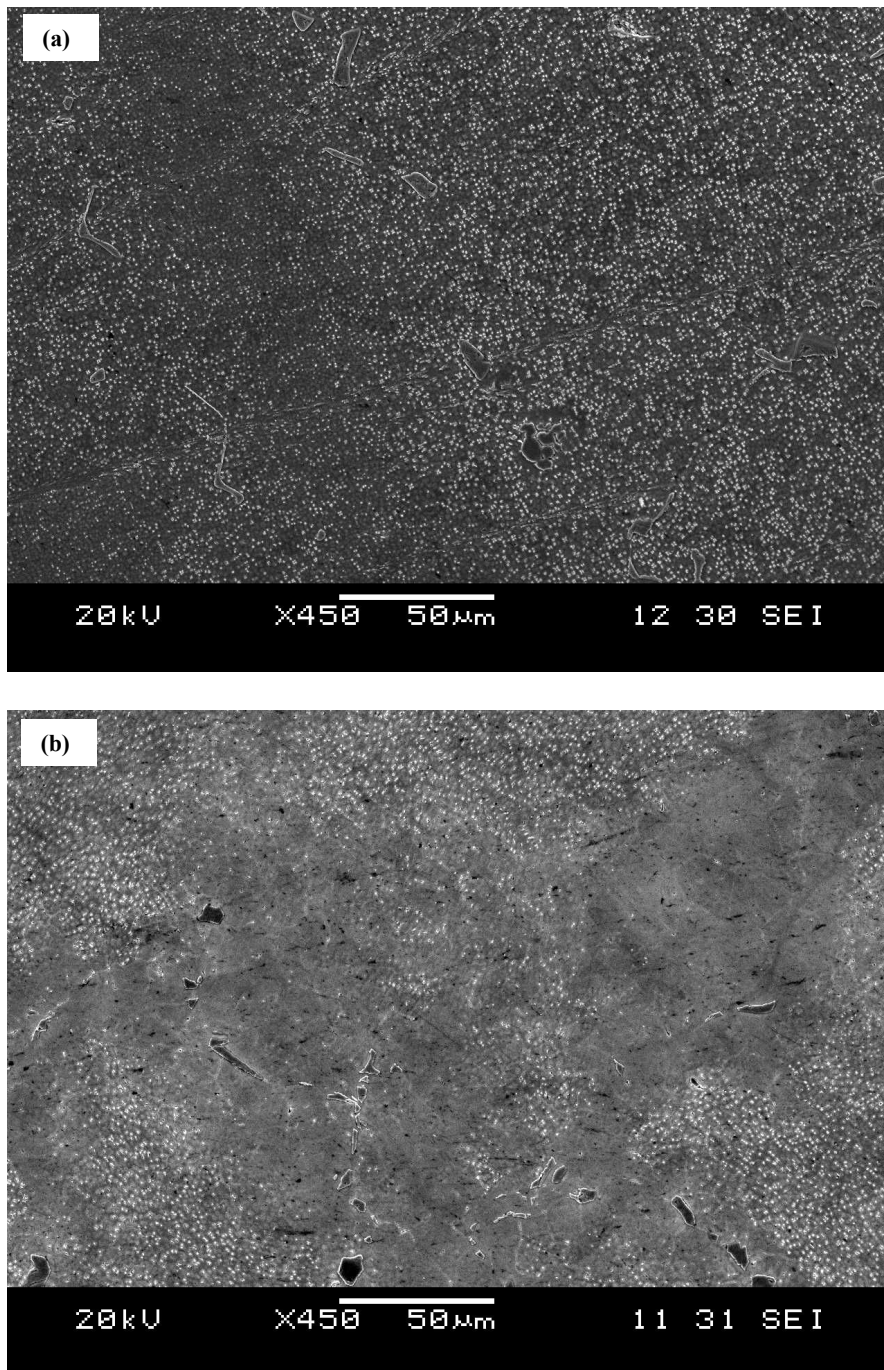


Figure 4 - 16: Gleeble-simulated specimens heated to 1170⁰C at 150⁰C/s and held for 1.5 seconds, followed by air cooling, (a) thermal cycle alone, (b) strained to 20% length reduction at peak temperature

cooling. The degree of precipitate dissolution in figure 4-16b, where the material was stressed to 20% compressive strain at the peak temperature, was greater than that observed in the specimen subjected to thermal environment alone (figure 4-16a). At an increased holding time (3.5 sec) at the peak temperature of 1170⁰C, a region in the material subjected to 20% compressive strain (figure 4-17b) was almost completely devoid of γ' precipitates while the precipitates were not completely dissolved in the material subjected to thermal environment alone (figure 4-17a). Occurrences of strain-enhanced/induced dissolution of second phase particles have been also reported in other alloy systems. In a study of hot deformation behavior of an Al-Mn-Zr alloy, the density of finely dispersed Al₃Zr particles was reported to have decreased during hot deformation due to deformation-induced dissolution [124]. Strain-induced dissolution of GP zones in the Al-Cu-Sn alloy system [125] and of γ' phase in fcc Fe-Ni alloys at low temperatures [126], and cementite decomposition in nanocrystalline pearlitic steels under severe plastic deformation [127], have all been reported.

The possibility of strain-enhanced solute diffusivity and the concomitant strain-enhanced precipitate dissolution, as observed in this present work, suggest that the dissolution of γ' phase in nickel-based superalloys during LFW can be significantly influenced by the compressive stress imposed on the material, especially at the forging stage of the process. As stated earlier, dissolution of γ' precipitates in nickel-based superalloys is commonly used in theoretical models to predict maximum temperature and associated mechanical properties in friction welded materials. The two main observations in this present work, namely, strain-enhanced dissolution and liquation reaction, can significantly increase the rate of dissolution of γ' particles such that the temperature of their complete dissolution

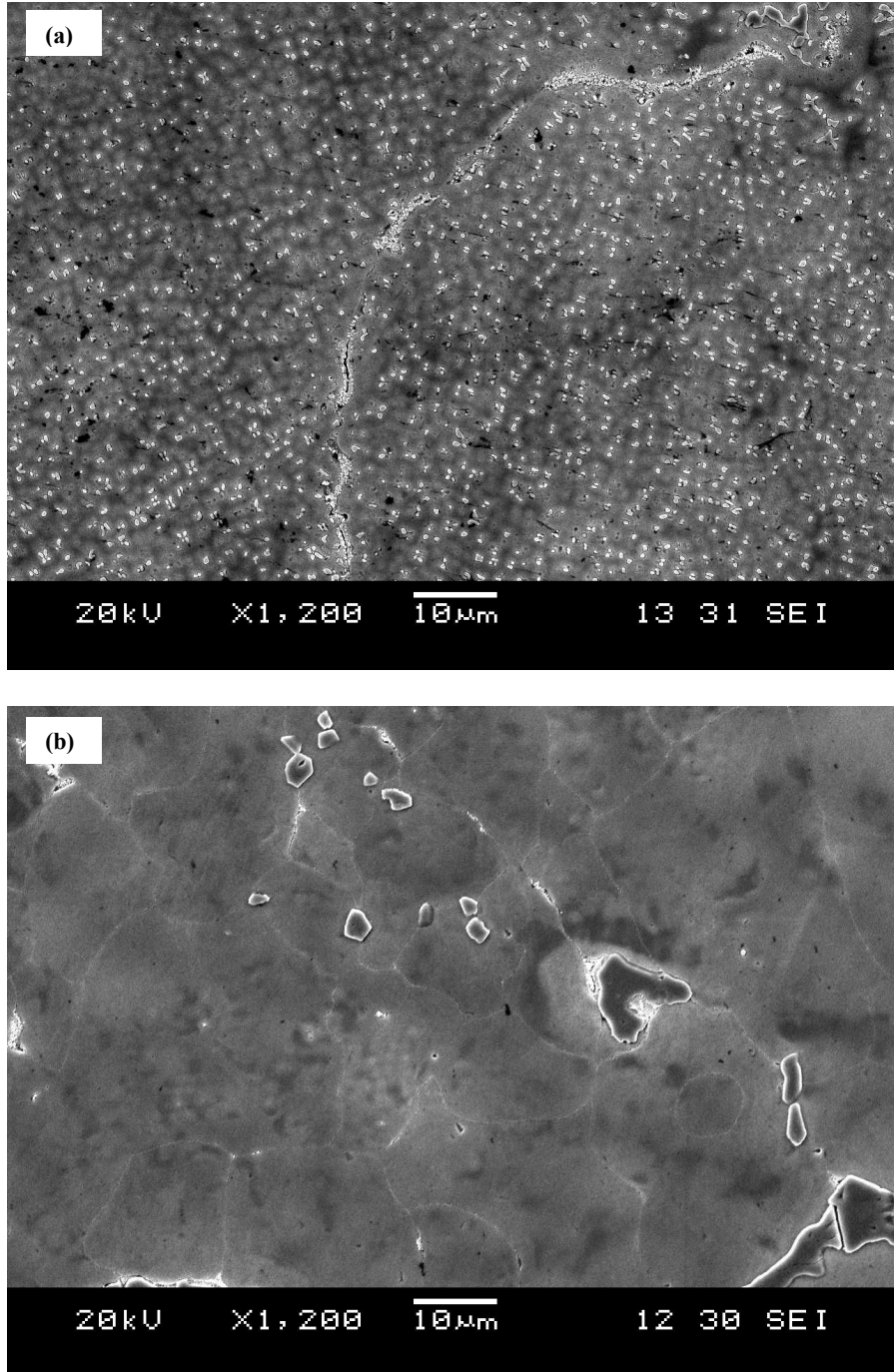


Figure 4 - 17: Gleeble-simulated specimens heated to 1170⁰C at 150⁰C/s and held for 3.5 seconds, followed by air cooling, (a) thermal cycle alone, (b) strained to 20% length reduction at peak temperature

may differ significantly from what is expected on the basis of exclusive solid-state dissolution mode. Hence, proper consideration of strain-enhanced dissolution and liquation reaction of γ' precipitates is paramount to the application of theoretical models to reliably predict temperature and properties in friction welded superalloys.

In contrast to the generally held views and reports, grain boundary liquation can occur during LFW, as discussed earlier. This establishes that the formation of intergranular and intragranular liquid is possible during both conventional fusion welding and friction welding processes, fulfilling an important condition for intergranular liquation cracking in both processes. However, despite the occurrence of intergranular liquation during LFW, grain boundary liquation cracking was not observed, as is usually the case during conventional fusion welding processes. Therefore, lack of cracking during friction welding is not due to lack of liquation, as is generally reported. However, the differences between crack susceptibility during conventional fusion welding and crack resistance during LFW can be related to the externally stress-induced compressive strain during LFW which is, generally, not present during conventional fusion welding. In this present work, the important factors responsible for the preclusion of intergranular liquation cracking during linear friction welding will be discussed next.

4.3 Preclusion of Intergranular Liquation Cracking

4.3.1 The Counter-Crack-Formation Effect of the Imposed Compressive Stress

The presence of a liquid film along grain boundaries is a necessary, but not a sufficient, condition for intergranular liquation cracking, since cracking requires that on-cooling tensile stresses exceed the local strength at one of the solid-liquid interfaces to cause decohesion along the interface [116]. In other words, HAZ liquation cracking requires the

co-existence of both liquated grain boundary and tensile stresses. The generation of tensile stress is critical for the liquation cracking to occur and must be present in the alloy at a temperature where continuous intergranular liquid film persists. Absence of cracking during LFW, as observed in the present work can be partly related to the state of stress within the work-piece during welding. Numerical simulation of the stress distribution in a material subjected to compressive axial loading, similar to that imposed during the forging stage of linear friction welding, has shown that most of the material is under compressive stresses, while tensile stress is mainly localized to regions extruded away from the joint area [128]. This suggests that imposing compressive load during the forging stage of linear friction welding can provide some resistance to crack formation. The counter-crack-formation effect of compressive loading is evident in a reported experimental work where compressive stress did not only result in crack prevention but also caused healing of short cracks in nickel-base superalloy Rene88DT [129]. Compressive stresses mainly dominate the joint area during the forging stage of the linear friction welding process, and the predominance of tensile stresses, which are usually later observed as residual stresses, occurs during continuous cooling after the forging stage. Therefore, despite liquation of grain boundaries by the liquation of grain boundary phases, application of compressive load during the forging stage appears to have contributed to preclusion of liquation cracking in the linear friction welded IN 738 by attenuating the driving force for cracking, which is the presence of tensile stresses during joining. This is supported by the presence of cracks observed in the extruded flash material (figure 4-18), displaced from the joint area under the influence of the compressive force, where the state of stress is expected to be predominantly tensile in

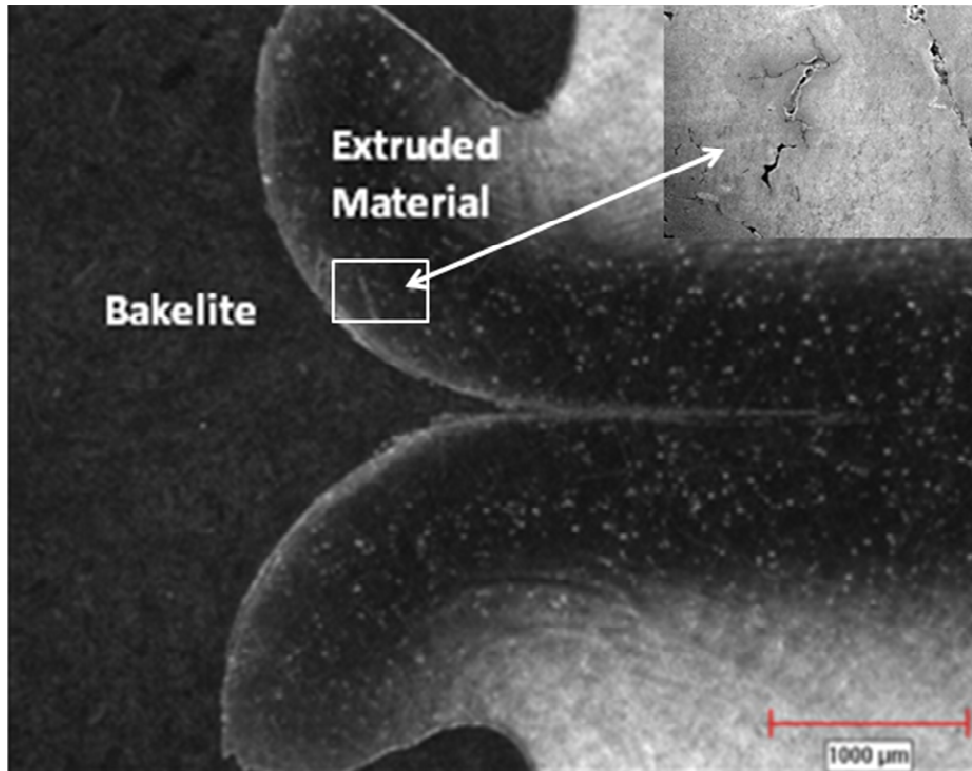


Figure 4 - 18: Optical micrograph of the extruded flash material, with an inset showing cracks in the material where tensile stresses are present

nature during joining. Tensile stresses are indeed generated during friction welding. The occurrence of residual tensile stresses has been confirmed in dissimilar aluminum and titanium friction welds [84], inertia friction welding of nickel-base superalloys [74] and linear friction welding of titanium alloys [93]. Therefore, it is imperative to justify why the material did not crack despite the observed occurrence of liquation and the possibility of tensile stress generation.

4.3.2 Strain-Induced Rapid Solidification and Enhanced Resistance to Cracking

Intergranular liquation cracking during conventional fusion welding processes requires the stability of grain boundary liquid to lower temperatures at which tensile stress generated during cooling could be sufficient to cause microfissuring by decohesion along one of the intergranular solid-liquid interfaces. Any factor that can reduce the stability of grain boundary liquid, such that the liquid does not persist to lower temperatures, will improve material's resistance to weld liquation cracking. It has been suggested that imposed strain on solids can thermodynamically drive a non-equilibrium system towards equilibrium [130]. The stress-induced compressive strain during linear friction welding has a tendency to reduce the stability of both intergranular and intragranular liquid produced during the welding process, by altering the kinetics of the resolidification process. As discussed earlier, the kinetics of thermodynamically driven phase transformations in materials fundamentally involve atomic diffusion, which can be affected by both the magnitude and sign of externally induced strain (equation 4.5).

The dissolution reaction of γ' precipitates, which is typically known to be controlled by diffusion of γ' forming elements away from the precipitate/matrix interface, was significantly enhanced by externally induced compressive strain, as discussed earlier. A

similar observation of increased γ' dissolution under compression has also been reported in another type of nickel-base superalloy [131], indicating that strain-enhanced diffusion is indeed active in this class of materials. The resolidification of metastable intergranular and intragranular liquid produced by the liquation of second phase particles is diffusion-dependent. One way by which grain boundary liquid can resolidify is by solid-state back-diffusion of solute atoms away from the liquid phase into the solid matrix. Back-diffusion of solute atoms has been regarded as one of the components of the resolidification of grain boundary liquid produced by the liquation of second phase particles, which could be appreciable in the time scales encountered during welding [132]. Intragranular liquid formed by the liquation of a second phase can also re-solidify by solid-state diffusion and at a rate determined by the solid-state diffusion [123]. Considering that solute diffusivity can be enhanced under compression, even in superalloys, the effect of imposed stress-induced compressive strain on back-diffusion controlled isothermal re-solidification of intragranular metastable liquid was investigated in this work by Gleeble thermomechanical simulation. Intragranular liquid was produced by non-equilibrium eutectic-type transformation reaction between γ' precipitates and γ matrix by rapidly heating IN 738 superalloy to temperatures above the equilibrium γ' solvus temperature in the alloy ($\sim 1160^\circ\text{C}$) up to 1230°C . It was observed, through the application of different levels of strain at various peak temperatures and holding times, that imposition of compressive strain significantly aided re-solidification of the intragranular liquid. Figure 4-19a shows the Gleeble simulated microstructure of a specimen heated to 1230°C , held for 2.5 seconds without imposed strain and air cooled. For comparison, Figure 4-19b shows the microstructure of a Gleeble specimen heated to 1230°C , held for 0.5 second

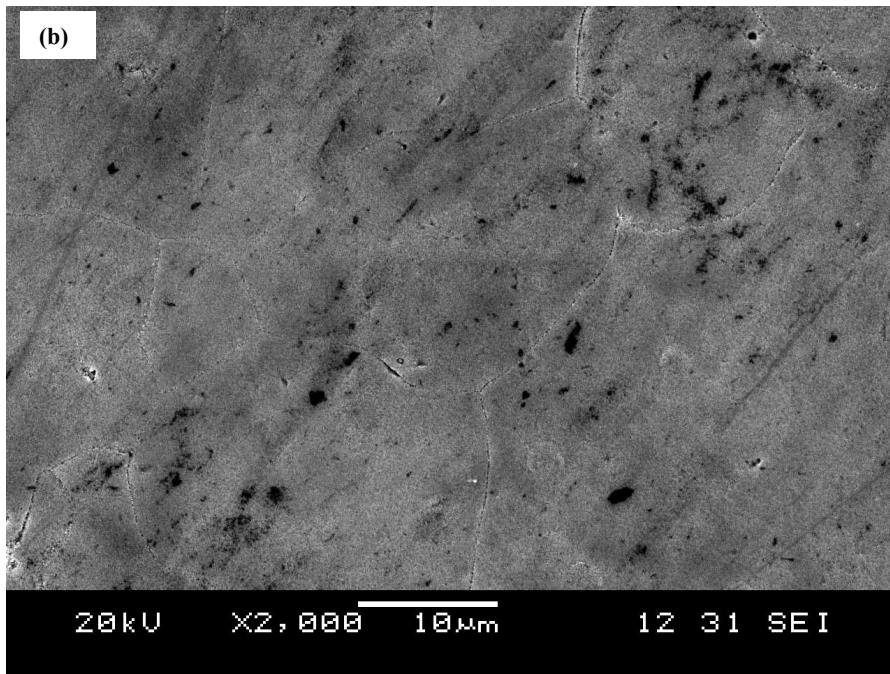
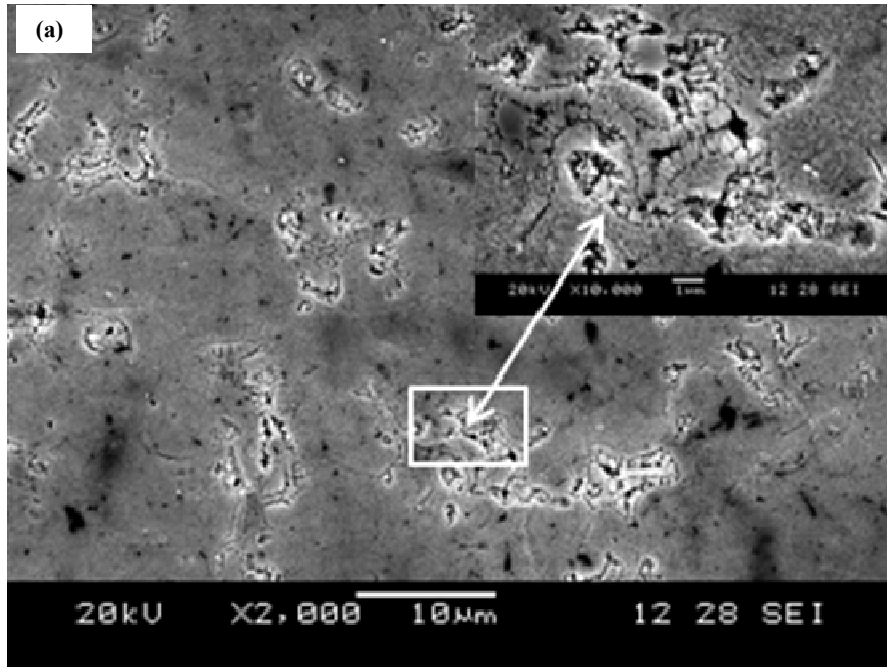


Figure 4 - 19: Gleeble simulated materials heated at $150^{\circ}\text{C}/\text{sec}$ and held for 2.5 sec at 1230°C followed by air cooling; showing (a) intragranular resolidified products under thermal cycle alone (b) absence of resolidified products when 25% length reduction was imposed

and then subjected to 25% compressive strain in 2 seconds followed by air-cooling. The microstructure of figure 4-19a is characterized by fine intragranular γ - γ' eutectic reaction products that formed from liquid during cooling, indicating the stability of liquid to lower temperatures where the resolidification products formed. Whereas, these features were completely eliminated under the influence of an imposed compressive strain, as shown in 4-19b, indicating that complete rapid isothermal resolidification of the liquid took place at a higher temperature due to an enhanced back diffusion. Similar observations were also made when the holding time was increased. Figure 4-20 also shows SEM micrographs of Gleeble-simulated materials at the same peak temperature of 1230⁰C, but after a holding time of 10.5 seconds instead of 2.5 seconds. It is seen that the imposed strain was effective in rapidly resolidifying the liquid by enhanced back-diffusion. It should be added that significant intragranular liquation occurred at 1230⁰C even after the 0.5 seconds holding time that was used prior to the application of strain, as presented in the SEM micrographs of figure 4-21. The liquid formed by rapidly heating the alloy to 1230⁰C persisted during the 2.5 and 10.5 seconds of holding under the application of thermal energy only and subsequently solidified at lower temperatures, during cooling, to produce the observed fine γ - γ' eutectic reaction products (figures 4-19a and 4-20a). Non-equilibrium γ - γ' eutectic solidification is known to take place at low a temperature as 1180⁰C in alloy IN 738 [17]. In contrast, however, the eutectic products were not observed in the specimen subjected to imposed stress-induced compressive strain (figures 4-19b and 4-20b), which can be attributed to enhanced isothermal re-solidification of the intragranular liquid during holding at the peak temperature, due to strain-aided solute back-diffusion. This observation of strain-induced rapid back-diffusion is also supported

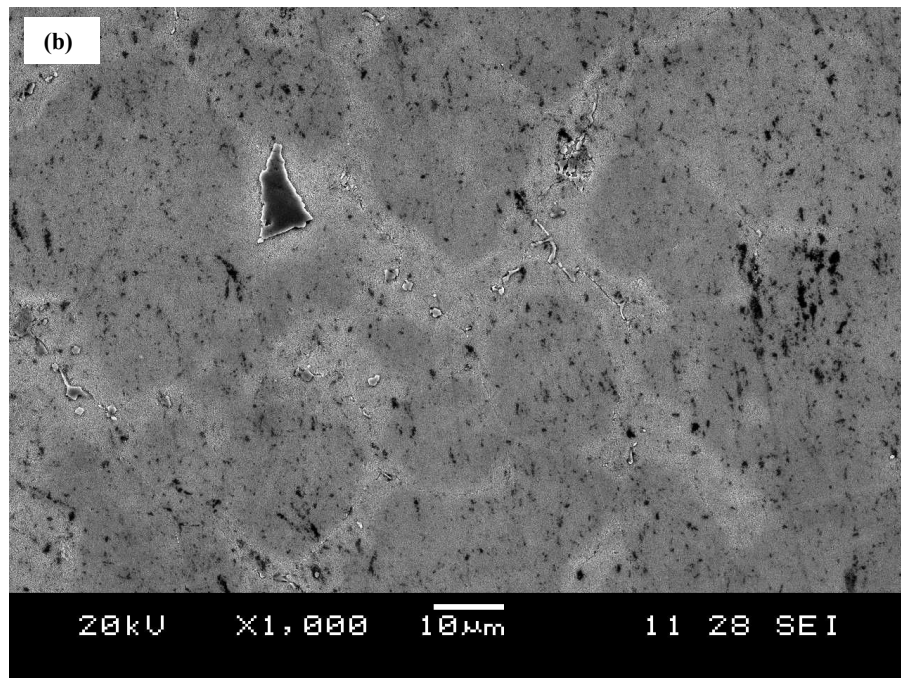
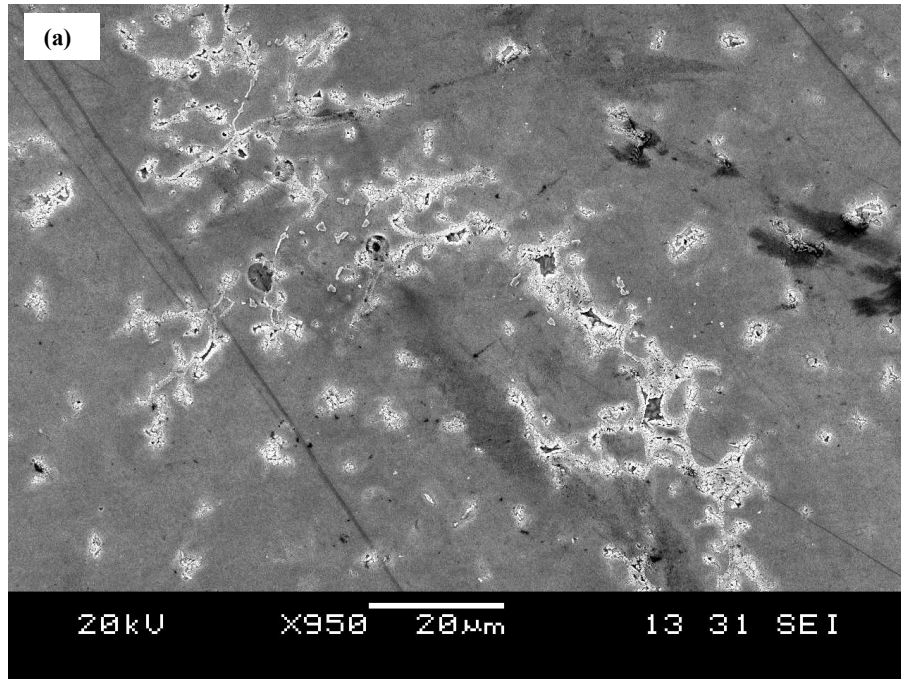


Figure 4 - 20: Gleeble simulated materials heated at 150⁰C/sec and held for 10.5 sec at 1230⁰C followed by air cooling; showing (a) intragranular resolidified products under thermal cycle alone (b) absence of resolidified products when 25% length reduction was imposed

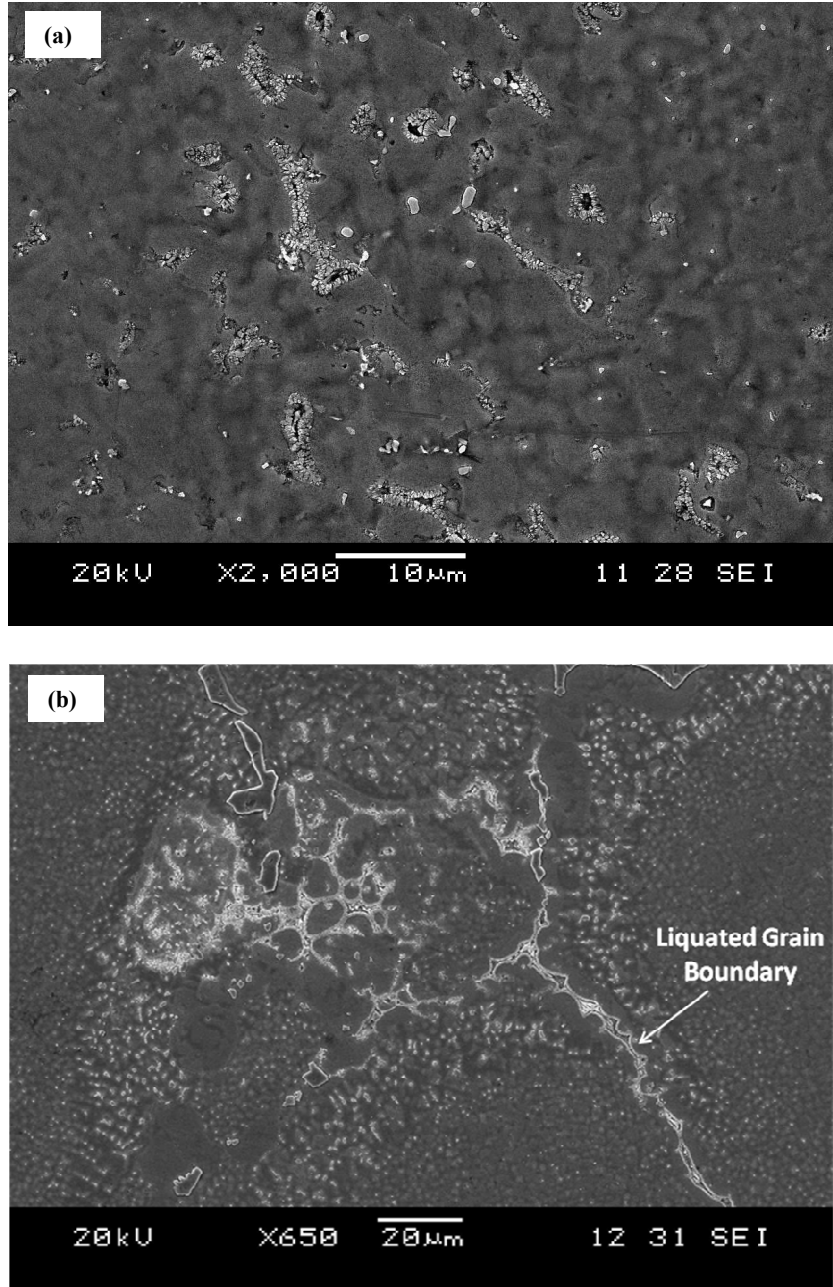


Figure 4 - 21: Gleeble-simulated specimens heated at $150^{\circ}\text{C}/\text{sec}$ to 1230°C , held for 0.5sec and air-cooled, showing (a) intragranular resolidified products and (b) liquated eutectic area and liquated grain boundary

by phase-field simulations by Junjie Li et al [133] where stress-induced increase in diffusivity resulted in enhanced back diffusion.

Aside from back-diffusion, an effective mode through which non-equilibrium grain boundary liquid can rapidly solidify at high temperatures is by intergranular liquid film migration (LFM), which is characterized by a homogeneously alloyed solidified zone produced by the migration process of liquid films [134]. The most widely accepted mechanism that is used in explaining LFM is diffusional coherency strain mechanism [135]. According to this, on introduction of a metastable liquid between two adjacent grains, a rapid equilibration process is set up by lattice solute back-diffusion. This results in composition dependent variation in lattice parameter between solute rich solid layer in contact with the liquid and the matrix well away from the solid-liquid interface. If there is a sufficient size difference between the solute and matrix atoms, coherency strains could develop within the grains due to the lattice mismatch. These strains would cause shifts in the free energy curve of the liquid-solid interface on either side of the film such that the compositions of the liquid and solid at equilibrium will be different at both solid-liquid interfaces. Ojo et al [134] have reported that atomic size mismatch between γ' forming elements and matrix atoms in IN 738 can induce intergranular LFM driven by diffusional coherency strain in the heat affected zone (HAZ) during conventional welding, where no externally applied stress is involved. During LFW, however, imposed stress-induced compressive strain can significantly influence LFM by (i) aiding the initiation stage (ii) increasing the migration velocity and (iii) abetting the sustenance of the process, and these are discussed next.

In situations involving externally applied compressive stress, such as during LFW, the initiation of LFM by generation of coherency strain, which is controlled by lattice solute back-diffusion, can be aided by strain-enhanced diffusivity. Furthermore, analytical modeling of LFM process has showed that the initial migration velocity, v , can be represented by the relationship [123];

$$v = \frac{D_L(\Delta C)}{(C_{L,T} - C_{S,T})\delta} \dots\dots\dots (4.6)$$

where D_L is the diffusivity in the liquid, δ is the initial liquid film thickness, ΔC is the concentration difference across the film, and $C_{L,T}$ and $C_{S,T}$ are the equilibrium concentrations of the solute(s) in the liquid and solid phases, respectively, at the solidifying interface. Fast solidification by LFM process is dependent and controlled by rapid solute diffusional transport within the intergranular liquid film. The liquid state diffusion is primarily driven by solute concentration gradient in the liquid, which is caused by difference in composition of the liquid in contact with the two adjacent strained grains. The difference in the liquid composition, ΔC , arises due to an existence of a differential strain, $\Delta\epsilon$, between the adjacent grains, which causes the liquid composition at equilibrium with the strained solids to differ. According to diffusional coherency strain theory, despite expected generation of similar levels of coherency stress in adjacent grains, owing to symmetrical lattice back-diffusion, $\Delta\epsilon$ does exist between the grains. This is due to difference in the values of crystallographic orientation dependent modulus of elasticity, Y , in the two grains [136]. An increase in $\Delta\epsilon$ will produce a corresponding increase in ΔC , which would imply a higher driving force for LFM, and as

such, any factor that effectively increases the magnitude of $\Delta\varepsilon$ can significantly accelerate the LFM process.

For a given set of Y values in two adjacent grains, the higher the magnitude of stress experienced by the grains, the higher will be $\Delta\varepsilon$. During conventional welding processes, where no externally applied stress is involved, based on coherency strain mechanism, $\Delta\varepsilon$ is generated mainly by coherency strain produced by change in intragranular chemical composition induced by solute lattice back-diffusion. However, during LFW, in addition to diffusional coherency strain that may be present, an externally induced compressive strain, which is generally orders of magnitude higher, is involved. Presence of a relatively large $\Delta\varepsilon$ owing to contribution from the externally applied stress could significantly alter the free energy curves of adjacent grains with respect to that of the liquid phase in between them, to produce a relatively high ΔC , as schematically illustrated in figure 4-22. Ultimately, this would translate to a greater driving force and, concomitantly, a higher LFM velocity, based on equation 4.6, which would result in a larger migrated region relative to a situation under only imposed thermal environment. This factor was investigated in the present work by comparing the size of LFM region in Gleeble-simulated specimens held for the same time period with and without imposed stress. Figures 4-23a and 4-23b show SEM micrographs of specimens simulated without imposed stress while figures 4-24a and 4-24b show SEM micrographs of specimens simulated with imposed stress. The size of migrated region in the specimens simulated under imposed stress, as presented in the SEM micrographs of figures 4-24a and 4-24b, was observed to be considerably larger (>100%) compared to that of the specimen simulated without externally applied stress as shown in figures figure 4.23a and 4.23b,

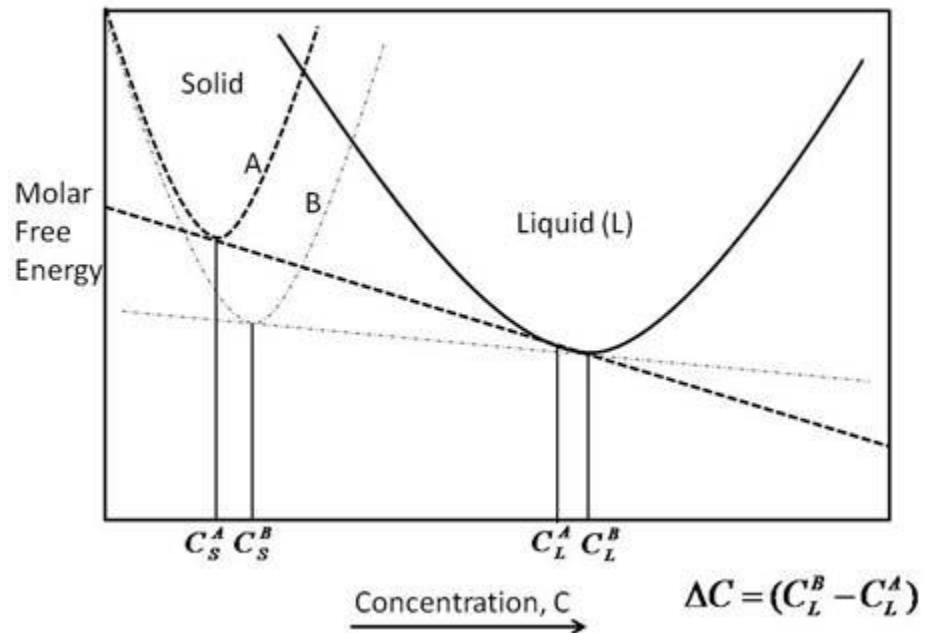
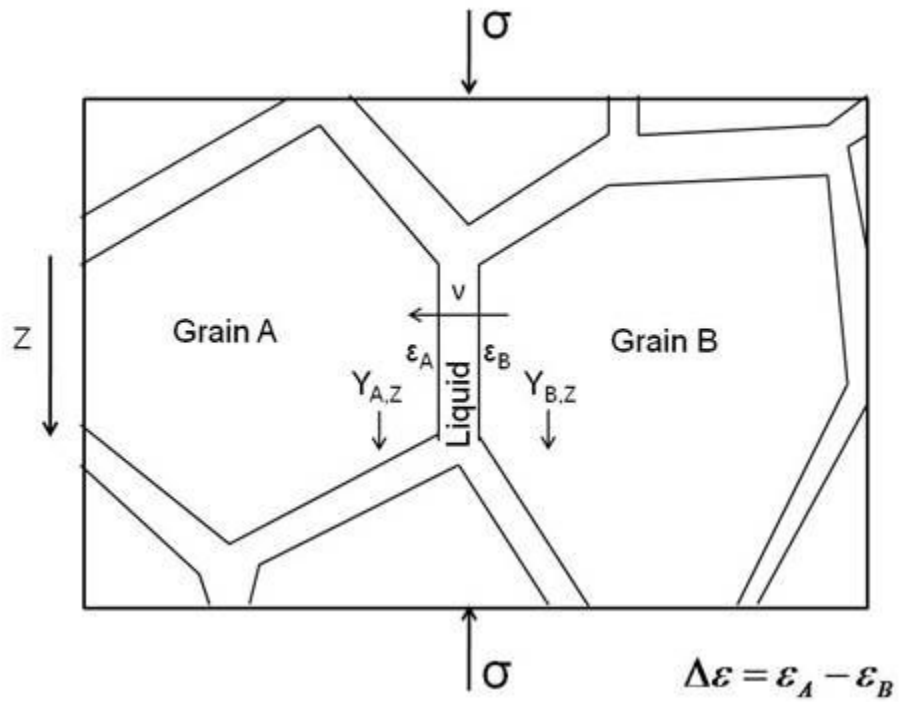


Figure 4 - 22: Schematic diagram showing liquid film between two grains of different orientation-dependent elastic modulus, Y , and the corresponding free energy curves

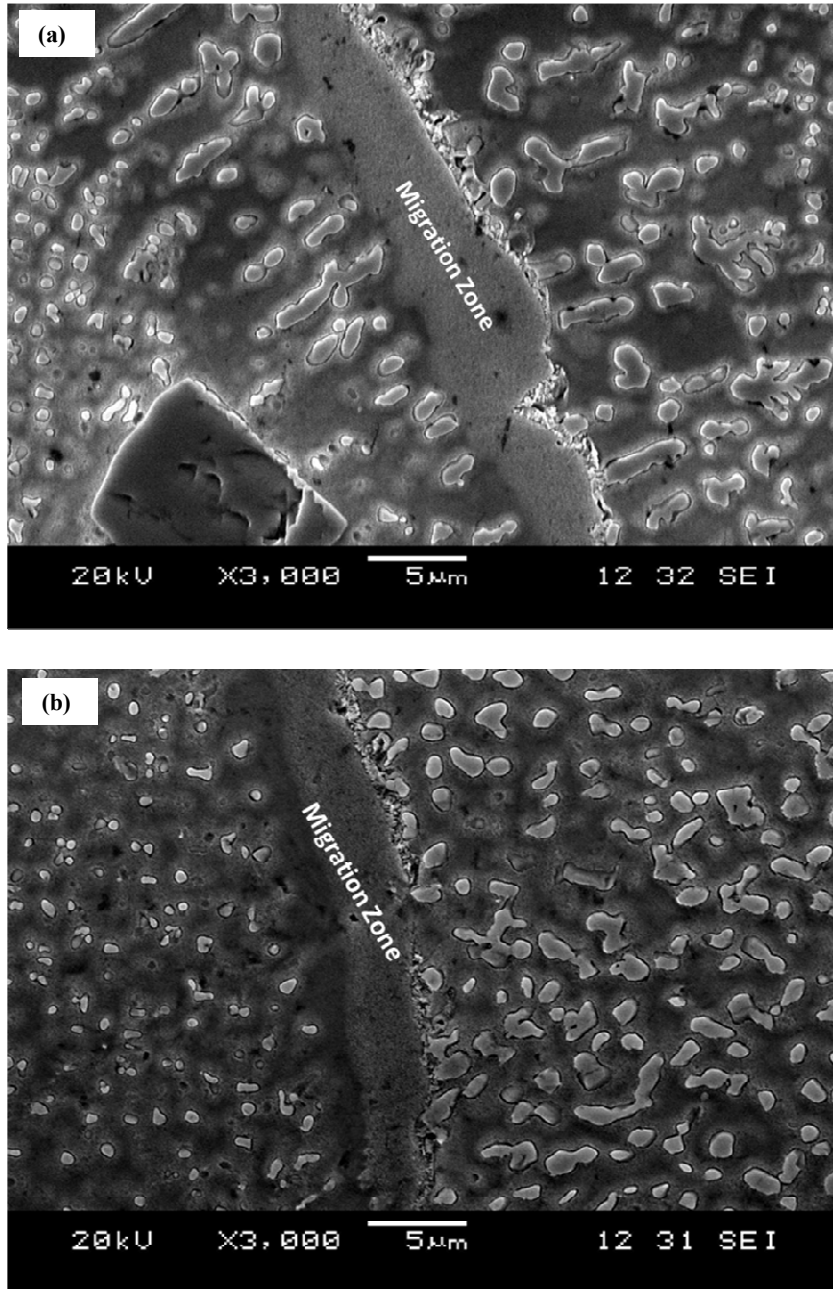


Figure 4 - 23: Liquid film migration (LFM) in Gleebly-simulated specimens heated at 150⁰C/sec and held at 1170⁰C for 1.5sec, followed by air cooling – thermal cycle alone

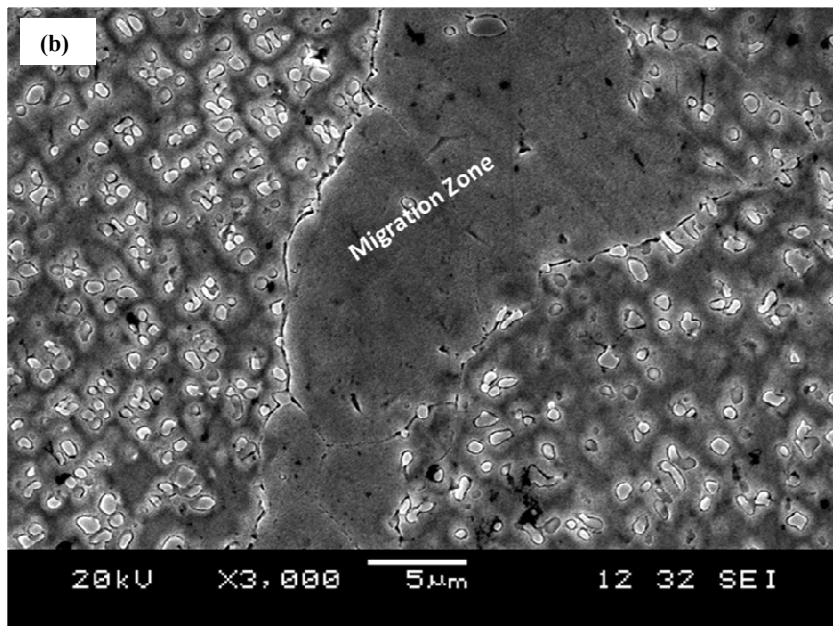
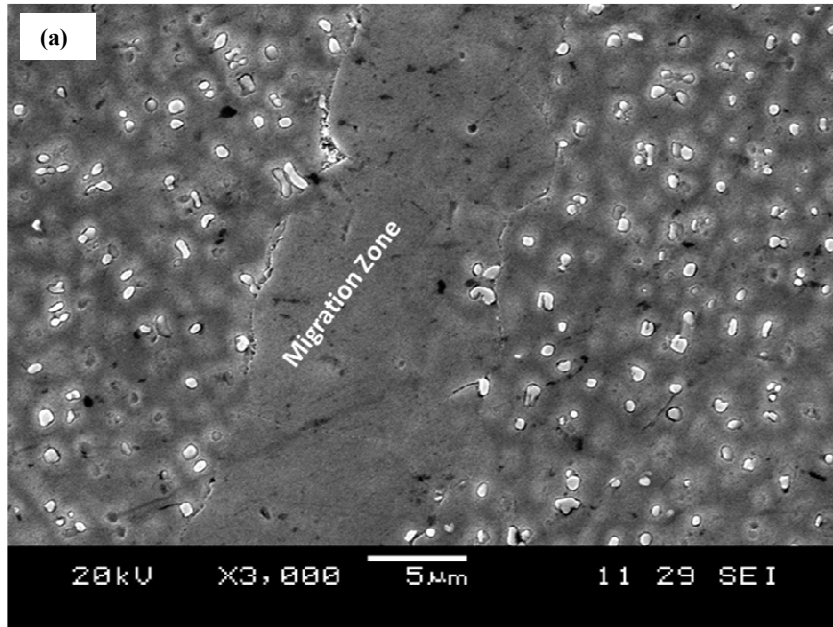


Figure 4 - 24: Figure 4.21: Liquid film migration (LFM) in Gleeble-simulated specimens heated at 150⁰C/sec and held at 1170⁰C for 1.5sec, followed by air cooling – strained to 20% length reduction at peak temperature

which indicates a higher LFM velocity under stress. These observed differences in the sizes of migrated zones in stressed and unstressed samples were consistent throughout all the simulated samples.

One major factor that limits the effectiveness of LFM is significant reduction in its driving force, due to loss of coherency, which could result in immobility of grain boundary film, thus, preventing complete elimination of the intergranular liquid. It has been recognised that coherency strain energy is a function of size of migrated region [137], and Baker et al [123] have suggested that coherency loss in the grain ahead of a migrating liquid film will occur when the effective solute penetration distance, D_s/v , becomes greater than or equal to the critical diffusion distance, L_s , required for the nucleation of misfit dislocations. In situations where an imposed stress is involved, such as during LFW, the associated higher migration velocity, v , could significantly reduce D_s/v , such that the condition of $D_s/v < L_s$ may persist for a longer time to sustain the process by coherency energy. Even in an eventual loss of coherency strain driving force, the $\Delta\varepsilon$ induced by the externally applied stress would serve as an extra source of driving energy to sustain rapid re-solidification of the intergranular liquid through LFM process. In addition, Brechet and Purdy [138] made an important comment on LFM process which is applicable to situations involving discrete liquating particles like γ' precipitates in superalloys. They reported that a complete solidification of grain boundary liquid film would occur only under non-steady state migration process, in which the intergranular liquid is not being constantly supplied with extra solute atoms, such as, from intragranular liquid. The enhanced re-solidification of intragranular liquid under externally imposed stress-induced compressive strain, as observed in the present work,

can shift the process towards such non-steady state condition, where complete solidification of intergranular liquid by LFM is possible.

Microscopy study of LFM region in the present work showed that besides smaller migrated region in the specimen simulated without imposed stress, non-equilibrium re-solidified eutectic products had formed ahead of the migrated zone, as shown in figures 4-23a and 4-23b. This implies that without the application of external stress, the LFM was not effective in completely removing the grain boundary liquid during holding at the peak temperature and the residual liquid ahead of the migrated zone transformed to eutectic products by non-equilibrium solidification reaction during cooling. Similar observation of ineffectiveness of LFM in completely removing intergranular liquid, due to loss of driving energy, resulting in formation of eutectic products and the attendant microfissuring during conventional welding, has been previously reported by Ojo et al [134]. In contrast, however, re-solidified eutectic products were not observed in front of migrated zone in Gleeble simulated specimens subjected to an imposed compressive stress in the present work, as shown in figures 4-24a and 4-24b. This, in addition to a larger migrated zone, indicates that a more sustained LFM under imposed stress was effective in enabling a complete solidification of the intergranular liquid prior to cooling to lower temperatures where eutectic solidification reaction occurs. Therefore, imposed compressive stress enhanced the rapid high temperature re-solidification of intergranular liquid through LFM, which is characterized by a combination of enhanced initiation stage, higher migration velocity and better sustenance. The elimination of both intergranular and intragranular liquid films during linear friction welding of IN 738 was achieved by a combination of solute back-diffusion and liquid film migration (LFM),

which were enhanced by imposed compressive strain. Therefore, contrary to general conception, prevention of weld cracking during linear friction welding cannot be attributed to preclusion of liquation during joining, instead, rapid re-solidification of intergranular and intragranular liquid aided by imposed compressive strain is a key factor that cannot be neglected in the understanding of cracking resistance. Liquid films produced by constitutional liquation of γ' precipitates during rapid heating were effectively eliminated by the imposed stress such that the liquid films did not persist to lower temperatures during cooling.

4.3.3 Comparison of Hot Ductility Behaviour under Compression and Tension

The rapid re-solidification processes reported in the previous section, which seemed to have aided resistance to cracking, were enabled by the occurrence of plastic deformation. Therefore, the effectiveness of imposed compressive stress in aiding rapid solidification is made possible by the fact that a material containing grain boundary liquid can exhibit significant hot ductility under compression. This is in stark contrast to the case under tensile loading, where intergranular liquation produces zero hot ductility. It has been suggested that, according to Gleeble hot ductility testing, a material loses all its ductility when the temperature reaches the on-heating nil-ductility temperature (NDT) and exhibits practically no ductility at all the temperatures above the NDT. Investigations have shown that in a number of different materials, NDT occurs as a result of grain boundary liquation [139]. The temperature range between the liquidus T_L and the NDT represents the on-heating zero ductility temperature range (ZDTR), within which the material exhibits practically zero ductility. The existence of tensile stresses in the material in this temperature range can result in cracking of the material. The alloy recovers its ductility

during cooling from the ZDTR when the temperature is lowered to the ductility recovery temperature (DRT). The temperature range between the on-heating peak temperature T_p and the corresponding DRT during cooling is usually referred to as brittle temperature range (BTR). This temperature range is important in describing the susceptibility of an alloy to HAZ cracking, since tensile strain (or stress) which causes cracking during conventional fusion welding does not generally develop until the weld begins to cool [140]. The results of Gleeble hot ductility testing performed on IN 738 by Ojo et al [116] revealed that the nil ductility temperature (NDT) and the ductility recovery temperature (DRT) of IN 738 were 1160°C and 1000°C respectively. The reported zero ductility temperature range (ZDTR) and the brittle temperature range (BTR), for a peak temperature of 1245°C , were 172°C and 245°C . It was found that the temperature range in which the constitutional liquation of γ' particles was observed was within the on-heating zero ductility temperature range (ZDTR), as determined by the hot ductility tests, and that the on-cooling ductility of the alloy was also significantly reduced due to the on-heating constitutional liquation of γ' particles, as reflected by the substantially lowered DRT compared to the NDT.

In this present work, the hot ductility behaviour of IN 738 under imposed compressive stress contrasts the reported nil ductility temperature (NDT) behaviour. Gleeble thermomechanical simulations of the coupled rapid thermal cycle and imposed compressive stresses reveal that the hot ductility of the alloy was not zero under compression at temperatures in the on-heating zero ductility temperature range (ZDTR) under tension. All Gleeble samples compressed at temperatures above the nil ductility temperature (NDT) exhibited appreciable amounts of plastic deformation despite the

occurrence of constitutional liquation of γ' particles, and the subsequent observation of grain boundary liquation. This is in agreement with previous studies [141, 142] on the deformation of semi-solid materials where appreciably high amounts of deformation were experienced by the material under compression. The liquation cracks observed in Gleeble-simulated specimens were limited to the periphery regions of highly compressed samples, suggesting that tensile stresses would have generated in these periphery regions due to barrelling effects. The presence of cracks at the periphery regions during semi-solid deformation has also been reported [141].

4.4 Other Weld Microstructural Characteristics

The preclusion of weld cracking during linear friction welding of IN 738 in this work, as discussed earlier, is attributed to rapid re-solidification of intergranular and intragranular liquid aided by an imposed compressive stress. This is a key factor that cannot be neglected in the understanding of the cracking resistance. Another major finding was that it is not only the cracking resistance that can be adequately understood by the studying the effect of compressive strain, in fact, microstructural evolution during joining cannot be properly understood without a careful analysis of the coupled thermal and strain effects. This section is devoted to explaining some important aspects of microstructural evolution in IN 738 during linear friction welding, which are considered to be potentially very useful for optimizing linear friction welding of superalloys.

One major constraint to the full understanding of weld zone microstructure in materials joined by frictional processes is the measurement of the actual temperature reached at the weld interface. The knowledge of the actual peak temperature at the weld interface can aid the understanding of microstructural evolution during the joining process. Efforts

have been made to evaluate peak temperatures in friction welds by the use of thermocouples [88, 143]. Though thermocouples make contact with the material at the point where the measurements were made, and their results are often generally acceptable, but they are limited in that they can only measure temperatures at distances away from the weld line such that actual temperature measurement at the weld interface is difficult. The use of thermocouples is mainly applicable to static processes; therefore, it is not well suitable for measuring temperatures at the weld interface of friction welds where dynamic processes take place. Accurate continuous temperature measurement and control during dynamic processes (such as casting, rolling and extrusion) can be achieved by the use of non-contact, optical pyrometry method [144]. This has been reported for measuring peak temperatures in the weld zone during friction welding of a nickel-base superalloy [111]. Nevertheless, optical pyrometry has been reported to be susceptible to fundamental difficulties including: variable emissivity, transmissions from intermediate media acting between the pyrometer and object, reflection of light from external radiation sources, fluctuation of objects within the view of the pyrometer, and other destabilizing factors [144]. Another method involves microstructural study, mainly, the dissolution behavior of γ' precipitates and its use as an input parameter in the development of theoretical models for temperature predictions [73, 111]. Here in this work, an attempt was made to evaluate the peak temperature reached at the weld interface during linear friction welding of IN 738 by using a microstructural approach. This was achieved by a careful correlation of weld microstructures with those of Gleeble thermo-mechanically simulated materials at different temperatures and different amounts of imposed compressive stresses.

Gleeble-simulated materials were analyzed by SEM to determine the simulation conditions that produced a microstructure that correlated with that of the weld zone presented in figure 4-25. After several simulations and microscopy, simulations showed that when the holding time was long, the resultant microstructure was unique and totally different from what was observed in the welded sample. To provide a typical example, the microstructure previously presented in figure 4-20b, where a long holding time of 10.5 seconds at 1230⁰C was used, was characterized by a unique, island-like, feature with a differential etching, whose identity has not been verified. SEM micrographs showing these features at other magnifications are presented in figures 4-26a and 4-26b. They formed throughout the entire compressed sample and were not found to occur when the holding/straining time was short (as in figure 4-19b held for 2.5sec). Though the exact nature of these observed features is not yet identified, they were not observed to be present in the weld zone of the linear friction welded IN 738. Rather, the weld zone microstructure correlated perfectly with the microstructure produced at a shorter holding/straining time at the peak temperature of 1230⁰C. This can be verified by carefully comparing figures 4-19b of the simulated material with figure 4-25 showing the weld zone microstructure. There are indications that both the time spent at peak temperature and the forging time during linear friction welding were not really long, which is in agreement with reports in the literature [108, 143].

In section 4.1, the occurrence of intragranular resolidification eutectic products in the thermo-mechanically affected zone (TMAZ) was reported and presented in figure 4-11. The observation of these resolidified products in the welded material, even after considerable amount of compression during the forging stage of the welding process,

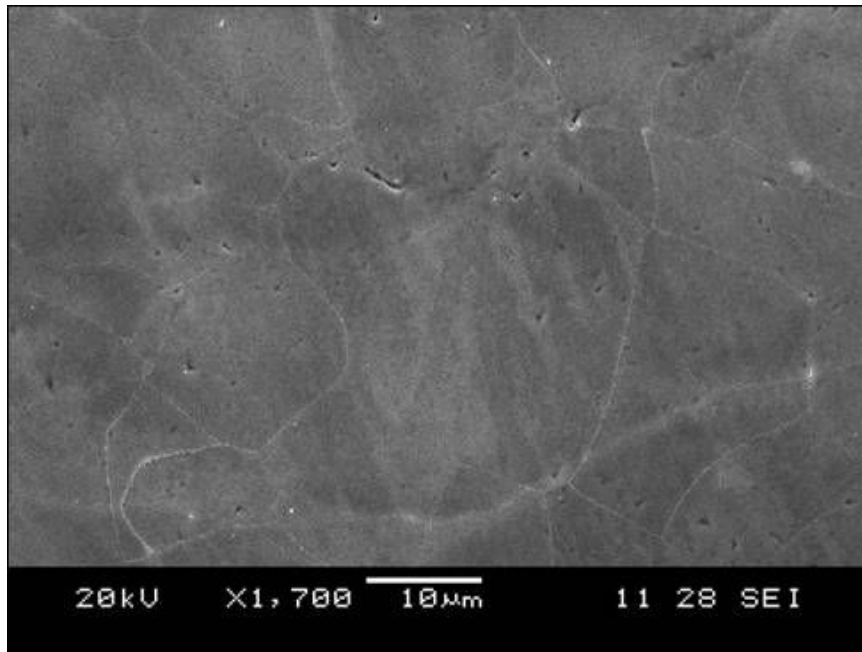


Figure 4 - 25: Weld zone microstructure

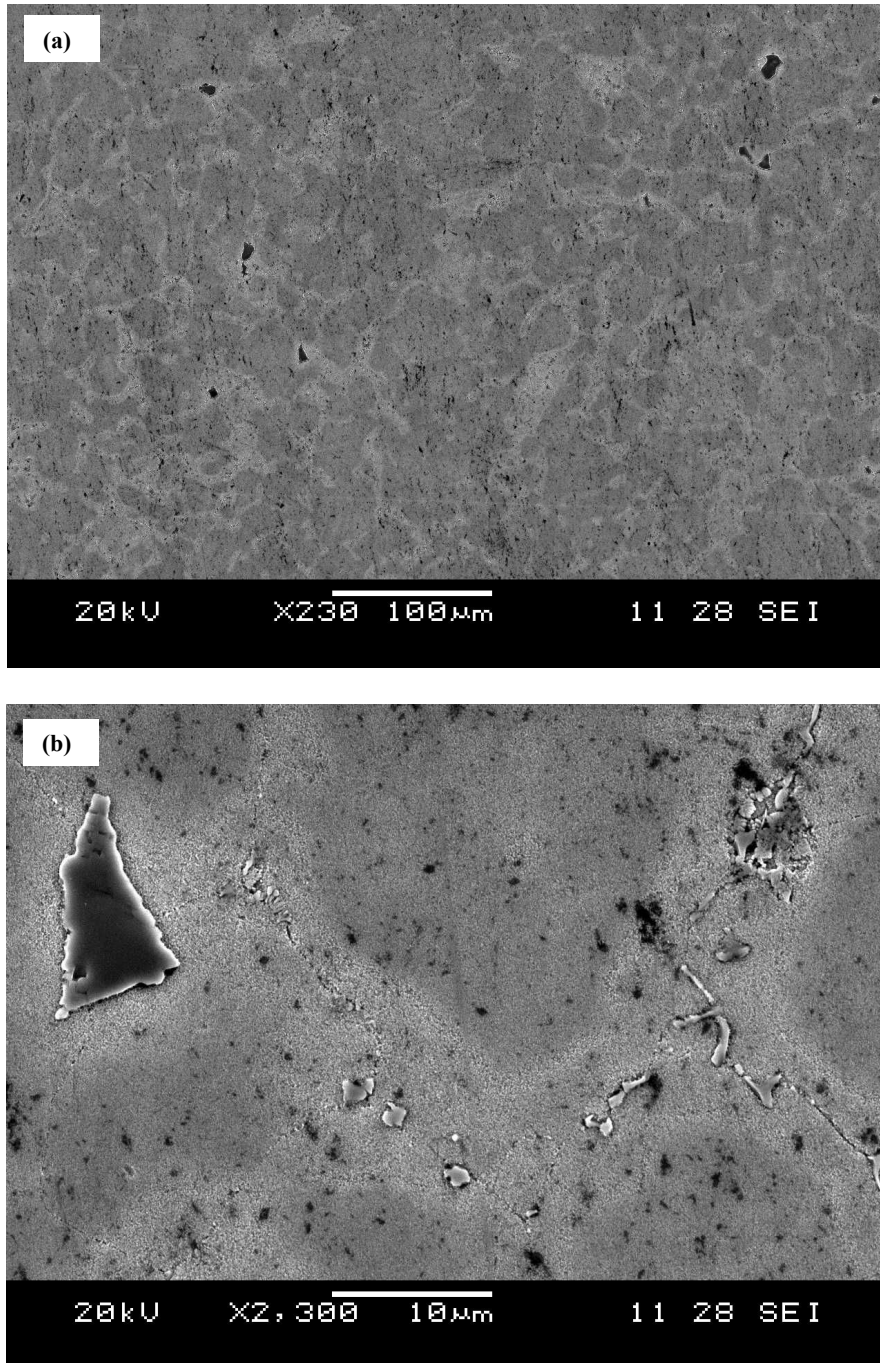


Figure 4 - 26: Gleeble-simulated materials heated at 150⁰C/sec to 1230⁰C, held for 0.5sec, strained to 25% length reduction in 10sec and air-cooled, showing boundary-like features (a) lower magnification (b) higher magnification.

suggests that significant intragranular liquation occurred in this region during rapid heating. It would have been expected, as discussed in section 4.3, that the liquid films that resulted in the formation of these resolidified products should have been rapidly removed by an enhanced back diffusion, but this was not the case. The effectiveness of strain in rapidly re-solidifying the liquid also depends on the amount of strain imposed on the material. Due to strain gradients in the welded material, with a lower level of strain in the TMAZ in comparison to the weld zone, the intragranular liquid films were not completely eliminated during forging which resulted in the formation of resolidified eutectic products by the remaining liquid. This was confirmed in the Gleeble-simulated materials in which an increase in strain reduced the formation of resolidified eutectic products. The result of several simulation experiments in this work revealed that the intragranular resolidified eutectic products formed in IN 738 only when the on-heating peak temperature in the material approached 1230⁰C. Figures 4-27a and 4-27b are SEM micrographs of Gleeble-simulated materials heated at the rate of 150⁰C/second to the peak temperature of 1200⁰C and held for 3.5 seconds and 10.5 seconds, respectively. These show that the grain interiors were essentially free from these resolidified products, even after holding for over 10 seconds. The formation of the intragranular resolidified products actually required increase in peak temperature. At 1230⁰C, however, intragranular resolidified products were observed even after a short holding time. This finding suggests that the temperature in the TMAZ where intragranular resolidified eutectic products were observed was not below a certain temperature range within which the resolidified products were observed in Gleeble-simulated materials under thermal effect alone at short holding times. Therefore, the peak temperature in the TMAZ could

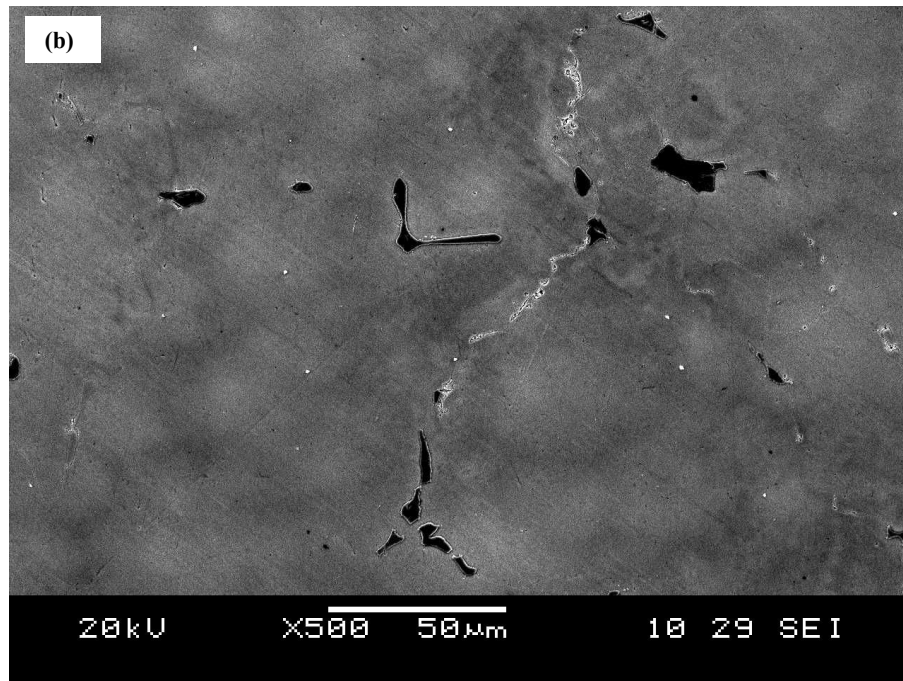
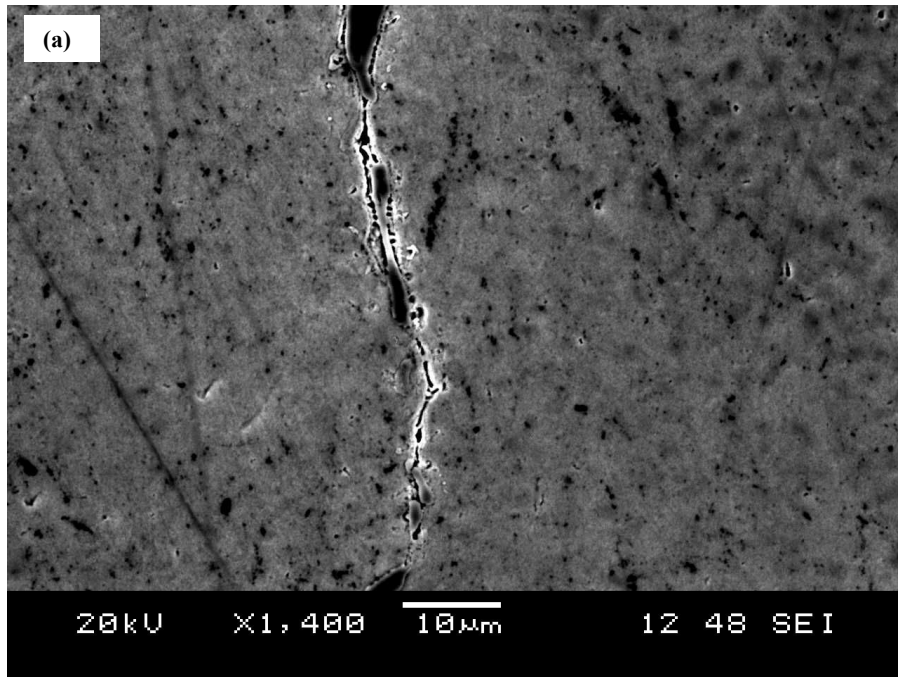


Figure 4 - 27: Gleeble-simulated materials heated at 150⁰C/sec to the peak temperature of 1200⁰C and held for (a) 3.5sec (b) 10.5sec, followed by air cooling

be estimated as being equal to or greater than 1230⁰C in the areas where intragranular resolidified eutectic products were observed. Since the temperature would have been greatest in the weld zone, compared to TMAZ and HAZ, the peak temperature reached in the weld zone during linear friction welding of IN 738 was not less than 1230⁰C. This is in agreement with a recently reported study that showed that peak temperature within the weld zone during friction processing of a material can be up to 0.9–0.97 T_m , where T_m is the melting temperature in Kelvin scale [145]. In addition, pyrometer measurements during friction welding of a nickel-based superalloy, Astroloy, reportedly showed that the weld zone temperature was up to 1280⁰C [111].

Notably, the weld zone microstructure in the linear friction welded IN 738 (Figure 4-25) is not consistent with what is expected at high temperatures (such as 1230⁰C and above) based exclusively on thermal effect. The formation of this type of microstructure cannot be duly explained without considering and incorporating the phenomenon of strain-induced rapid solidification that was observed for the first time in this work. As stated earlier, rapid heating of IN 738 to 1180⁰C and above produces intergranular and intragranular liquation with resultant as-cooled microstructure consisting of re-solidified eutectic products. Nevertheless, such re-solidified eutectic products were not observed within the weld zone in the linear friction welded specimen despite indications that the peak temperature that was reached there was, at least, 1230⁰C during the joining. This can be attributed to rapid re-solidification of non-equilibrium liquid produced on heating to the peak temperature, facilitated by the considerable compressive strain experienced by the weld zone during the welding. The TMAZ (away from the weld interface), which experienced marginal strain compared to the weld zone, contained the re-solidified

eutectic products (Figure 4-11). This is at variance with what is typically observed in conventionally welded materials, in that formation of re-solidified eutectic products normally increases towards the weld zone and is often accompanied by liquation cracking. The disparity can be explained by the absence of an externally applied stress during conventional welding, which is present during linear friction welding.

OIM Study of Recrystallized Grains: In section 4.1, the weld zone microstructure was described as possibly characterized by recrystallization on both sides of the weld interface, which also evolved in such a manner so that the recrystallization was localized along prior grain boundaries in the TMAZ. A higher magnification optical micrograph of the grain structure in the weld zone is presented in figure 4-28. In order to confirm the occurrence of recrystallization during joining, the distribution and character of grain boundaries in the weld zone and TMAZ was determined by using electron back scatter diffraction (EBSD) based orientation imaging microscopy (OIM). The grain boundaries were characterized by studying an important grain boundary structural parameter, which was first proposed by Kronberg and Wilson [146], termed the coincident site lattice (CSL). The CSL classification system is a system in which a three-dimensional lattice is created in the region of interpenetration of lattices of two adjoining grains. The ratio of the volume of the unit cell of the CSL to that of the crystal (the reciprocal density of the coincident sites) is described by the parameter Σ . In a $\Sigma 3$ grain boundary, which is a coherent twin boundary, one-third of the interpenetrating lattice points are coincident, and in a $\Sigma 29$ grain boundary, one-twenty ninth of them are coincident. Therefore, the larger the Σ value, greater is the degree of disorder in a grain boundary. OIM analysis of the linear friction welded joint confirmed that recrystallization actually occurred during

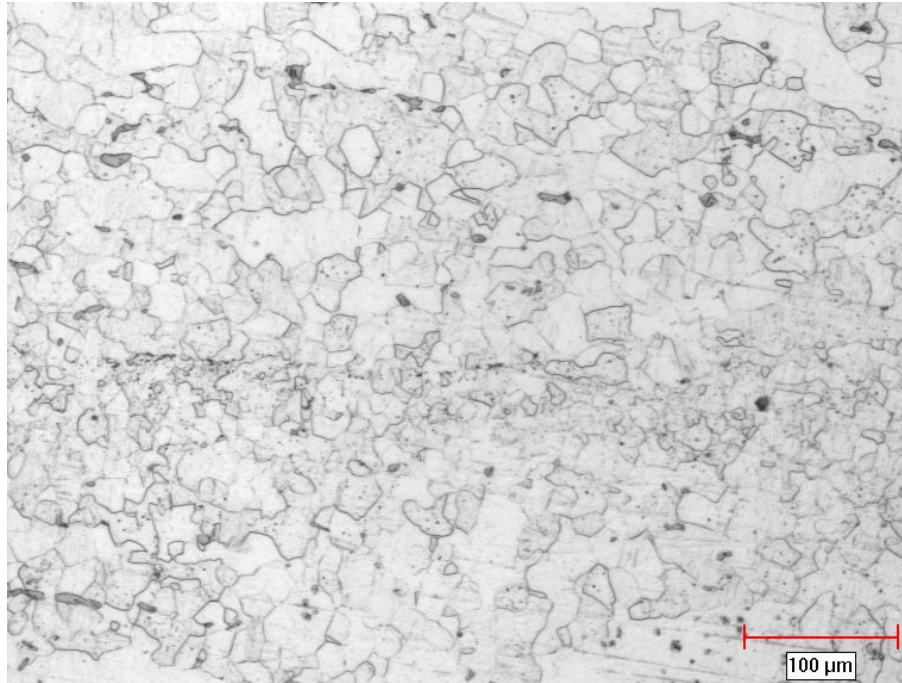
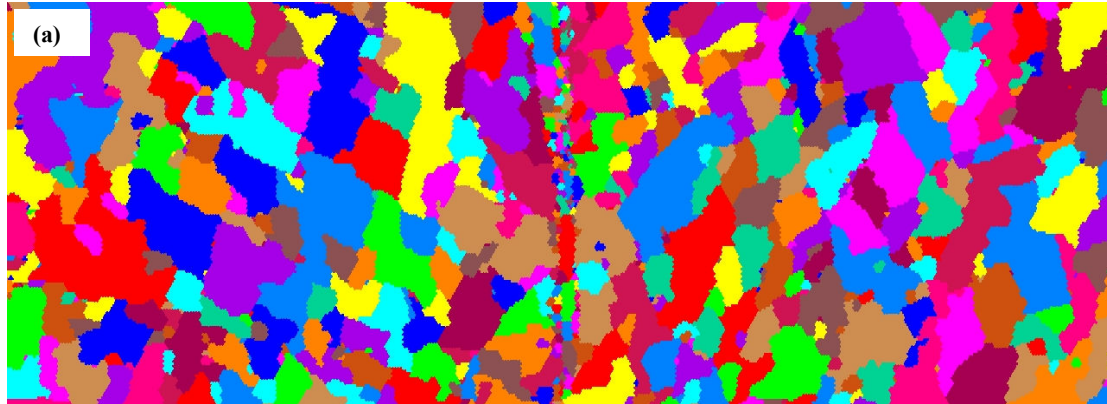


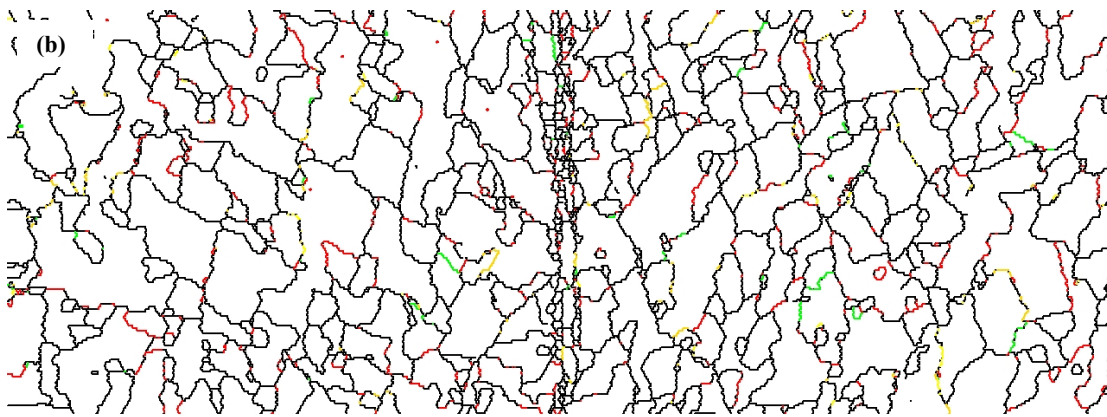
Figure 4 - 28: Optical micrograph showing recrystallization in the weld zone

joining and also revealed the distribution and characters of the recrystallized grains, which had an average diameter of 13.85 μm . Most of the recrystallized grain boundaries had Σ values greater than 29, implying a very high degree of disorder. Figures 4-29a and 4-29b show the distribution of the unique grains that formed on both sides of the weld centerline and the character of the grain boundaries, respectively, with black lines representing grain boundaries of $\Sigma > 29$. An OIM image (figure 4-30a) of a region of transition from the weld zone to the TMAZ confirmed an earlier suggestion that the TMAZ exhibited partial recrystallization such that recrystallization became mainly localized on prior grain boundaries. The character of grains at the transition region is presented in the OIM image of figure 4-30b.

A notable observation about the recrystallization behaviour in the weld zone of linear friction welded IN 738 was the presence of finer (smaller) grains at the weld centerline area (figures 4-29a and 4-29b) compared to other weld zone areas away from the centerline. Based on the theory of recrystallization, there is a temperature range, ΔT , within which recrystallization occurs, and high temperature, high strain and longer holding time within this temperature range favour the formation of grains of larger size, through nucleation and growth processes. It is known that the weld centerline area experienced the highest peak temperature and largest extent of strain during joining. The joint area cools down by the conduction of heat away from regions of higher temperature to regions of lower temperature in the base material. It is therefore reasonable to conceive that the weld centerline area, that experienced the highest temperature, spent a longer time within ΔT , compared to other weld zone areas. Consequently, larger grain size is expected at the weld centerline area of the weld zone due to the fact that it experienced



180.0 μm = 90 steps Unique Grain Color



180.0 μm = 90 steps Boundary levels: 10°

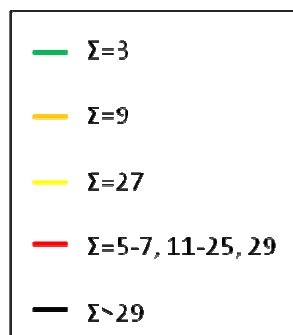


Figure 4 - 29: OIM images showing (a) the distribution of unique recrystallized grains across the weld centerline, and (b) the character of the recrystallized grains

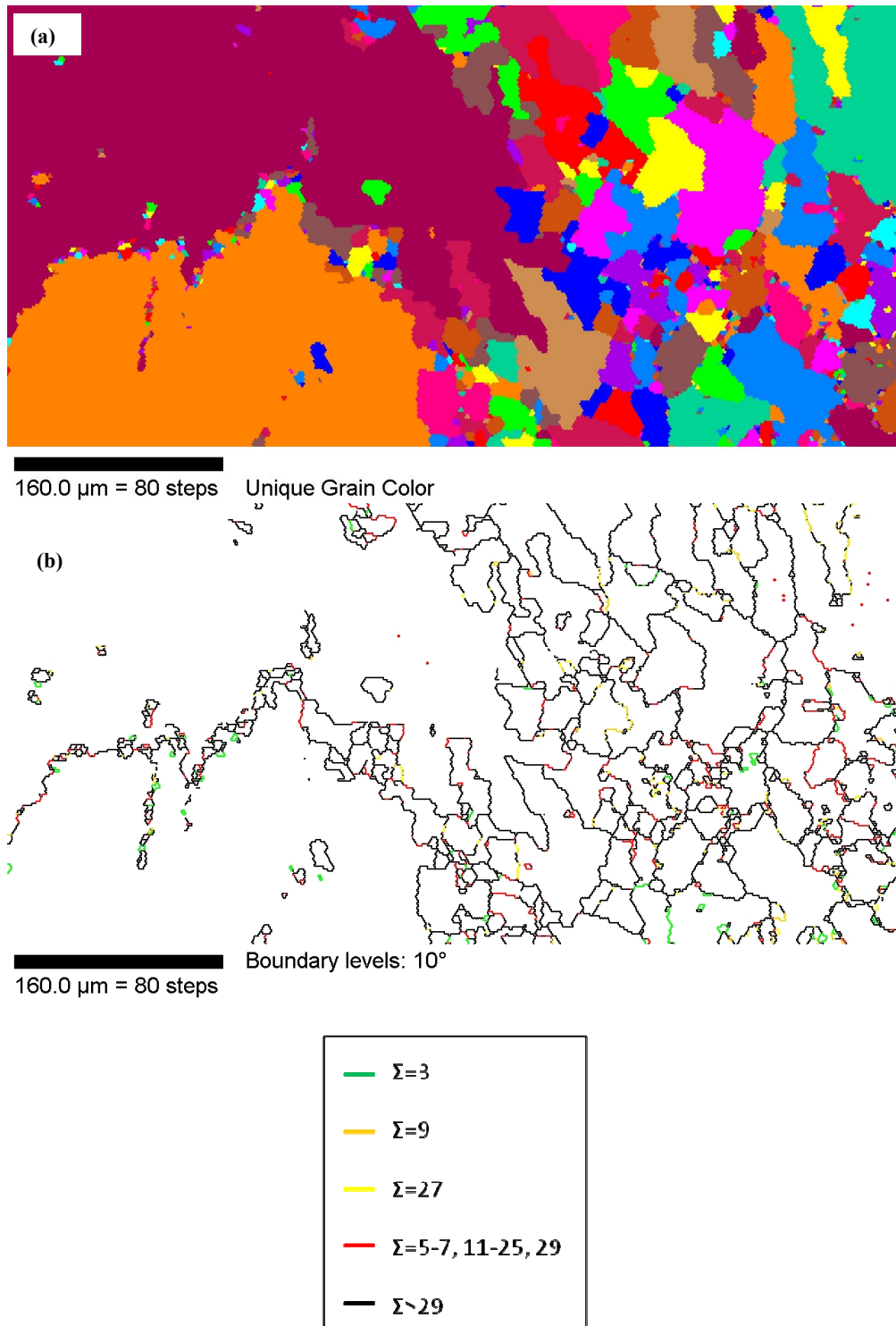


Figure 4 - 30: OIM images showing (a) the distribution of unique recrystallized grains at the transition region between the weld zone and TMAZ, and (b) the character of the recrystallized grains at the transition region

the highest temperature, largest compressive strain and longest time within ΔT . However, the observation of smaller grains at the weld centerline area relative to other weld zone areas is in contrast to this expectation, which suggests that recrystallization during joining cannot be solely explained by classical solid-state recrystallization theory. The observed deviation from the expected behaviour can be related to the liquation–resolidification processes that took place during joining. As previously stated, liquation occurred in these regions during joining. Since recrystallization is generally known to be a solid-state phenomenon, it is conceivable that recrystallization in the liquated regions would have occurred after a complete solidification of the metastable liquid produced in these regions during the joining process. This implies that recrystallization may provide some information about the resolidification behavior in the material. In the region that solidified last, possibly due to the presence of more liquid, recrystallization might have commenced later compared to those regions that solidified earlier due to a relatively smaller amount of liquid. In such a situation, recrystallized grains in the weld centerline area can be smaller than those in other regions. Gleeble simulations showed that the extent of liquation increased with temperature. This implies that the highest amount of liquation would have occurred at the weld centerline area, due to the highest peak temperature, and this weld centerline area could have solidified last compared to other areas in the weld zone. Hence, recrystallization could have started later at the weld centerline area and, thus, with finer grains relative to other regions, as observed by OIM. This observation, which cannot be explained exclusively by solid-state reaction, is consistent with the concepts of non-equilibrium liquation reaction and strain-induced

rapid solidification during linear friction welding as reported and discussed for the first time in this work.

Chapter 5

Summary and Conclusions

Microstructural analysis of linear friction welded IN 738 was carried out. Gleeble thermo-mechanical simulation of the welding process was carried out in order to adequately understand the microstructure of the linear friction welded material. The simulated microstructures correlated very well with actual weld microstructures, and provided an insight into the microstructural evolution during the welding process. The following summarize the results of the study:

1. Linear friction welding produced a sound and crack-free joint in IN 738, an alloy generally considered to be very difficult to weld due to its high susceptibility to heat affected zone liquation cracking during welding.
2. The linear friction welding of IN 738 was accompanied by significant microstructural changes across the joint, including a complete dissolution of the strengthening γ' precipitates within about 600 μm on either sides of the weld line. Very fine γ' particles reprecipitated within this region during weld cooling, which contributed to the increased micro-hardness observed closer to the weld line.
3. In variance to the generally held view and reports, grain boundary liquation occurred during linear friction welding of IN 738. It was observed to occur as a result of non-equilibrium eutectic-type liquation reaction between the main strengthening phase of the alloy, which is γ' precipitate, and the γ matrix of the alloy.
4. The occurrence of intergranular liquation, however, did not result in liquation cracking in linear friction welded IN 738 material, as is the usual case during

conventional fusion welding processes. Therefore, contrary to general conception, prevention of weld cracking during the process is not due to preclusion of liquation during joining.

5. The counter-crack-formation effect of the compressive stress imposed on the material during forging seems to have contributed to the preclusion of liquation cracking by attenuating the development of tensile stresses.
6. Rapid re-solidification of intergranular and intragranular liquid aided by external stress-induced imposed compressive strain is another key factor that provided additional resistance to cracking during joining.
7. The result of this work indicates that the peak temperature reached in the weld zone during LFW of IN 738 was likely more than 1230°C.
8. Complete recrystallization occurred in the weld zone of the welded material. Two regions can be identified in the weld zone – the weld centerline area, where finer grains formed, and the other weld zone areas, where the recrystallized grains were of larger size. The formation of finer recrystallized grains at the weld centerline area, relative to other weld zone areas, is consistent with the concepts of non-equilibrium liquation reaction and strain induced rapid solidification.
9. The understanding of microstructural evolution during linear friction welding requires proper consideration of non-equilibrium liquation reaction and strain-induced rapid solidification concepts discussed for the first time in this work.

Chapter 6

Suggestions for Future Work

1. Post-weld Heat Treatment (PWHT) should be carried out on the linear friction welded IN 738 in order to relieve residual tensile (and/or compressive) welding stresses in the material. Detailed microstructural analysis of the post-weld heat-treated material will be required to understand the microstructural response of the welded alloy to thermal treatment.
2. Mechanical testing of the weld joint should be performed on both the as-welded and post-weld heat-treated materials in order to evaluate the high-temperature mechanical behavior of the linear friction welded IN 738.
3. Since the results obtained in this work were from one pre-weld heat treatment condition (solution heat-treatment), investigation of any variation in material response to the welding process under different pre-weld heat treatment conditions should be performed.

References

- [1] C.T. Sims, N.S. Stoloff, W.C. Hagel (Editors), Superalloys II: High Temperature Materials for Aerospace and Industrial Power, A Wiley-Interscience publication, 1987, p.3
- [2] M. Prager, C. S. Shira, Welding Res. Council Bull, Vol. 128, 1968, pp.1
- [3] E.F. Bradley, Superalloys: A technical Guide, ASM International, Metals Park, OH, 1988
- [4] Alloy IN 738: A Technical Data, INCO, New York, 1 – 11
- [5] G. C. Bieber, R.J. Mihalisin, 2nd International Conference on the Strength of Metals and Alloys, Asilomer, ASM Vol. IV, p. 1031
- [6] W. F. Smith, Structure and Properties of Engineering Alloys, 2nd Ed, New York : McGraw-Hill, c1993, p.504
- [7] A.T. Egbewande, MSc Thesis, University of Manitoba, Canada, 2008
- [8] W. Hoffelner, E. Kny, R. Stickler, W.J. McCall, The Effect of Aging Treatment on the Microstructure of the Ni-base Superalloy IN 738, Z. Werkstofftech Vol. 10, 1979 p. 84
- [9] R.C. Reed, The Superalloys: Fundamentals and Applications, Cambridge University Press, 2006, p. 35

- [10] R.F. Decker, Strengthening Mechanisms in Nickel-Base Superalloys, Climax Molybdenum Company Symposium, Zurich, May 5-6, 1969
- [11] D.S. Paulonis, J.M. Oblak and D.S. Duvall, Trans. ASM, Vol. 62, 1969, p.611
- [12] M.J. Donachie and S.J. Donachie, Superalloys: A Technical Guide, 2nd Edition, ASM International, 2002 p.31
- [13] T.J. Garosshen, G.P. McCarty, Metall. Mater. Trans., Vol. 16A, 1985, p.1213
- [14] W.C. Hagel, H.J. Bettie, Iron and Steel Institute Special Report, London, 64, p.98
- [15] J.S. Zhang, Z.Q. Hu, Y. Murata, M. Morinaga, N. Yukawa, Metall. Mater. Trans., Vol. 24A, 1993, p. 2443
- [16] R. Sallemark, Progress Report 2 Cost 50 Programme Sweden, 1975.
- [17] R. Rosenthal, D.R.F. West, Mater. Sci. Technol., Vol. 15, 1999, p.1387.
- [18] J.M. Larson, Metall. Mater. Trans., Vol. 7A, 1976, p.1497
- [19] H.R. Zhang, O.A. Ojo, M.C. Chaturvedi, Scripta Mater. Vol.58, 2008, p.167
- [20] W.C. Johnson, J.E. Doherty, B.H. Kear, A.F. Giamei, Scripta Metall., Vol. 8, 1974, p.971
- [21] J.E. Doherty, B.H. Kear, A.F. Giamei, C.W. Steinke, "Effect of Surface Chemistry on Grain Boundary Strength", Grain Boundaries in Engineering Materials, Claitor's Publishing Div., 1975

- [22] A.W. Thompson, *Acta Metall.*, Vol. 28, 1975, p.607
- [23] J.W. Schultz, University of Michigan, Uni. Microfilms, Ann Arbor, PhD Thesis, 1965
- [24] D.A. Canonico, W.F. Savage, W.J. Werner, G.M. Goodwin, *Welding Research Council*, 1965, p.68
- [25] O.A. Ojo, PhD Thesis, University of Manitoba, Canada, 2004
- [26] K. Masubuchi, *Encyclopedia of Materials Science and Engineering*, M.B. Bever (Editor), Vol. 7, 1986, p.5280
- [27] O.A. Idowu, PhD Thesis, University of Manitoba, Canada, 2010
- [28] S. Kou, *Welding Metallurgy*, 2nd ed., John Willey & Sons Inc., Hoboken, 2003, p 9.
- [29] *Welding Handbook*, Vol. 3, 7th edition, American Welding Society, Miami, FL, 1980, p.170
- [30] K. Easterling, "Introduction to the Physical metallurgy of Welding", 2nd Edition, Copyright Butterworth-Heinemann, 1992
- [31] K. Masubuchi, *ASM Handbook: Welding, Brazing and Soldering*, Vol. 6, 1993, p.1094
- [32] K. Masubuchi, *Analysis of Welded Structures*, International Series on Materials Science and Technology, Vol. 33, Copyright Pergamon Press Ltd, 1980, p.149

- [33] G.J. Davies, J.G. Garland, *Int. Metall. Rev.*, Vol. 20, 1975, p.83
- [34] D.C.G. Lees, *J. Inst. Metals*, Vol. 72, 1946, p.343
- [35] A.R.E. Singer, P.H. Jennings, *J. Inst. Metals*, Vol. 73, 1947, p. 273
- [36] M.J. Cieslak, *Cracking Phenomena Associated with Welding*, ASM Handbook: Welding Brazing and Soldering, Vol. 6, 1993, p88
- [37] K. Nakata, F. Matsuda, *Trans JWRI*, Vol. 24, 1995, p.83
- [38] R.G. Baker, *Philosophical Transactions of the Royal Society of London, Series A, Mathematical and Physical Sciences*, Vol. 1307, 1976, p.207
- [39] M.C. Chaturvedi, *Materials Science Forum*, vols. 546-549, 2007, p.1163
- [40] J.J. Pepe and W.F. Savage, *Welding J.* Vol. 46, 1967, p.411
- [41] W.A. Owczarski, D.S. Duvall and C.P. Sullivan, *Weld. J.*, Vol. 46, 1967, p.423s.
- [42] B. Weiss, G.E. Grotke and R. Stickler, *Weld. J.*, Vol. 49, 1970, p.471s.
- [43] J.A. Brooks, *Weld. J.*, Vol. 53, 1974, p.517.
- [44] R. Nakkalil, N.L. Richards and M.C. Chaturvedi, *Metall. Mater. Trans. A*, Vol. 24A, 1993, p.1169.
- [45] B. Radhakrishnan and R.G. Thompson, *Metall. Mater. Trans. A*, Vol. 24A, 1993, p.1409.

- [46] K.R. Vishwakarma, M.C. Chaturvedi, in: E.A. Loria (Ed.), *Superalloys 718, 625, 706 and Derivatives 2005*, The Minerals, Metals and Materials Society, 2005, p.637
- [47] O.A. Ojo, N.L. Richards, M.C. Chaturvedi, *Mater. Sci. Technol.* Vol. 20, 2004, p.1027
- [48] O.A. Ojo, N.L. Richards, M.C. Chaturvedi, *Metall. Mater. Transac. A*, 37A, 2006, p.421
- [49] M. McLean, A. Strang, *Metals Technol.*, Vol. 11, 1984, p. 454
- [50] E.D. Hondros, M.P. Seah, in R.W. Chan (Ed): *Physical Metallurgy*, 3rd edition, North Holland, Amsterdam, 1984
- [51] M.P. Seah, E.D. Hondros, *Proc. R. Soc.*, Vol. 335A, 1973, p.191
- [52] D. McLean, in *Grain Boundaries in Metals*, Clarendon Press, Oxford, 1957
- [53] J.H. Westbrook, K.T. Aust, *Acta Metall.*, Vol. 11, 1963, p.1115
- [54] K.T. Aust, R.E. Hanneman, P. Nissen, J.H. Westbrook, *Acta Metall.*, Vol. 16, 1968, p.291
- [55] R.L. Eadie, K.T. Aust, *Scripta Metall.*, Vol. 4, 1970, p.641
- [56] K.T. Aust, *Canadian Metallurgical Q.*, Vol. 13 (1), 1974, p.133
- [57] D.C. Paine, G.C. Weatherly, K.T. Aust, *J. Mater. Sci.*, Vol. 21, 1986, 4257

- [58] X. Huang, M.C. Chaturvedi, N.L. Richards and J. Jackman, *Acta Mater.*, Vol. 45, 1997, p.3095
- [59] L. Karlson, H. Norden, *Acta Metall.* Vol. 36, 1988, p.13
- [60] L. Karlson, *Acta Metall.* Vol. 36, 1988, p.25
- [61] L. Karlson, H. Norden, *Acta Metall.* Vol. 36, 1988, p.35
- [62] W. Chen, M.C. Chaturvedi, *Metall. Mater. Trans. A*, Vol. 29A, 1998, p.743
- [63] J.A. Quimby, *Friction Welding: Present-Past-Future*, ASTME Creative Mfg Seminar, Technical paper No SP65-90, April 1965
- [64] V.I. Vill, *Friction welding of metals*, translated and published by the American Welding Society, 1962
- [65] M.B. Hollander, C.J. Cheng, J.C. Wyman, *Weld. J.*, Vol. 42(11), 1963, p.495s
- [66] C.J. Cheng, *Weld. J.*, Vol. 41(12), 1962, p.542s
- [67] C.J. Cheng, *Weld. J.*, Vol. 42(5), 1963, p.233s
- [68] K.K. Wang, Wen Lin, *Weld. J.*, Vol. 53(5), 1974, p.233s
- [69] D.E. Spindler, "Inertial Friction Welding", Manufacturing Technology, Inc., South Bend, IN 46628 USA, 1978
- [70] "Inertia Welding: Simple in Principle and Application", *Welding and Metal Fabrication*, Vol. 47(8), 1979, p.585

- [71] "Aircraft (Welding of Components)", *Welding Design and Fabrication*, Vol. 53(11), 1980, p.88
- [72] M. Preuss, J.W.L. Pang, P.J. Withers, G.J. Baxter, *Metall. Mater. Trans. A*, Vol. 33A, 2002, p.3215
- [73] M. Soucail, A. Moal, L. Naze, E. Massoni, C. Levailant, Y. Bienvenu, *Superalloys 1992*, The Minerals, Metals and Materials Society, 1992, p.847
- [74] M. Preuss, P.J. Withers, G.J. Baxter, *Mater. Sci. Eng. A*, Vol. 437, 2006, p.38
- [75] K.H.G. Schmitt-Thomas, R. Siede, *The international Conference of Quality and Reliability in Welding*, Hangshou, China, 1984, p.D-8-1
- [76] M. Sahin, *J. Mater. Processing Technol.*, Vols. 153-154, 2004, p.1011
- [77] A.S. Bahrani, *JOM-2 (Joining of Metals)*, Helsingor, Denmark, 15-18 Apr., 1984, p.98
- [78] F.D. Duffin, A.S. Bahrani, *Third Int. Conf. on Advances in Welding Processes*, U.K., 1974, p.228
- [79] F.D. Duffin, A.S. Bahrani, *Wear*, Vol. 26, 1973, p.53
- [80] M. Cocks, *J. Appl. Physics*, Vol. 35, 1964, p.1807
- [81] S.A. Saregin, A.S. Saregin, V.P. Sabantsev, *Svar. Proiz.*, 1979, No 11, p.22
- [82] I.O. Khazanov, N.I. Fomin, *Welding International*, Vol. 6(11), 1992 p.890

- [83] F.D. Duffin, A.S. Bahrani, Metal Construction, 1967, p.267
- [84] Y.-C. Kim, A. Fuji, Sci. and Technol. of Welding and Joining, Vol. 7(3), 2002, p.149
- [85] S. Sundaresan, K.G.K. Murti, Materials Forum, Vol. 17, 1993, p.301
- [86] K.G.K. Murti, S. Sundaresan, Metal Construction, 1993, p.331
- [87] S.V. Lalam, G.M. Reddy, T. Mohandas, M. Kamaraj, B.S. Murty, Mater. Sci. Technol., Vol. 25(7), 2009, p.851
- [88] A. Vairis, M. Frost, Wear Vol. 217 , 1998, p.117
- [89] C. Mary, M. Jahazi, Advanced Engineering Materials, Vol. 10(6), 2008, p.573
- [90] A. Vairis, M. Frost, Mater. Sci. Eng. A, Vol. 217, 1999, p.477
- [91] H.A. Kuhn, R.S. Green, Weld. J., Vol. 70(10), 1991, p.27
- [92] P. Wanjara, C. Booth-Morrison, E. Hsu, M. Jahazi, Proceedings of the 7th International Conference on Trends in Welding Research, Georgia, USA, May 16-20, 2005, p.855
- [93] M. Karadge, P. Frankel, A. steuwer, C. Lovell, S. Bray, P.J. Withers, M. Preuss, Joining of Advanced and Specialty Materials, Mater. Sci. and Technol. (MS&T) 2006: Product Manufacturing, p.35
- [94] H.H. Koo, W.A. Baeslack III, Materials Characterization, Vol. 28, 1992, p.157

- [95] M. Karadge, M. Preuss, P.J. Withers, S. Bray, Mater. Sci. Eng. A, Vol. 491, 2008, p.446
- [96] W.M. Thomas et al., International Patent Application Number PCT/GB92/02203 and GB Patent Application Number 9125978.8 (December 1991), U.S. Patent Number 5,460,317
- [97] B.J. Drucap, W.J. Arbegast, Society of Automotive Engineers, Inc., Paper 1999-01-3432, 1999
- [98] W.J. Arbegast, Hot Deformation of Aluminum Alloys III, TMS (The Minerals, Metals and Materials Society), 2003, p.313
- [99] W.J. Arbegast, 11th Annual Advanced Aerospace Materials and Processes Conference and Symposium, ASM international, Seattle WA, March 14-15, 2000
- [100] W.J. Arbegast, P.J. Hartley, Proceedings of the 5th International Conference on Trends in Welding Research, Pine Mountain, GA, June 1-5, 1998, p.541
- [101] E.D. Nicholas, The 6th International Conference on Aluminum Alloys, ICAA-6, July 5-10. 1998. Toyohashi, Japan
- [102] A.P. Reynolds, T.U Seidel, M. Simonsen, 1st Symposium on Friction Stir Welding, 14-16 June 1999, Rockwell Science Centre, Thousand Oaks, California, USA
- [103] C.J. Dawes, Bulletin Vol. 41 No 4, July/August 2000, p.51

- [104] R.S. Mishra, M.W. Mahoney, S.X. McFadden, N.A. Mara, A.K. Mukherjee, Scripta Mater., Vol. 42, 2000, p.163
- [105] W.M. Thomas, E.D. Nicholas, S.D. Smith, 2001 TMS Annual Meeting and Exhibition, Aluminum Joining – Emphasizing Laser and Friction Stir Welding, New Orleans Feb. 11-15, 2001
- [106] A.N. Davies, “Friction Welding in Aerospace Manufacture”, in: Exploiting Friction Welding in Production, written by The Welding Institute, 1979, p.20
- [107] J.R. Doyle et al, Pratt and Whitney, AWS National Fall Meeting, 6-9 October 1969; also in Welding Journal, Vol. 48(11), 1969, p.514s
- [108] P. Wanjara, M. Jahazi. Metall. Mater. Trans. A, Vol. 36, 2005, p.2149
- [109] A.T. Egbewande, H.R. Zhang, R.K. Sidhu, O.A. Ojo, Metall. Mater. Trans. A, Vol. 40A, 2009, 2694
- [110] F. Daus, H.Y. Li, G. Baxter, S. Bray, P. Bowen. Mater. Sci. and Technol., Vol. 23, 2007, p.1424
- [111] M. Soucail, Y. Bienvenu . Mater. Sci. Eng. A, Vol. 220, 1996, p.215
- [112] O.M. Barabash, R.I. Barabash, G.E. Ice, Z. Feng, D. Gandy, Mater. Sci. Eng. A, Vol. 524, 2009, p.10
- [113] B.I. Bjorneklett, O. Grong, O.R. Myhr, A.O. Kluken, Acta Mater. Vol. 46, 1998, p.6257

- [114] M.F. Ashby, K.E. Easterling, *Acta Metall.* Vol. 30, 1982, p.1969
- [115] D.L. Sponseller, *Proceedings on the Conference on Superalloys. USA*, 1996, p. 259
- [116] O.A. Ojo, M.C. Chaturvedi. *Mater. Sci. Eng. A*, Vol. 403, 2005, p.77
- [117] M.J. Whelan, *Metal Science Journal*, Vol. 3, 1969, P.95
- [118] U.H. Tundal, N, Ryum, *Metall. Mater. Trans. A*, Vol. 23A, 1992, p.433
- [119] A.K. Jena, M.C. Chaturvedi, in: Brendan M. Stewart (Ed), *Phase transformation in Materials*, Prentice-Hall Inc, 1992, p.91
- [120] N.E.B. Cowern, P.C. Zalm, P. Van der Sluis, D.J. Gravensteijn, W.B. de Boer, *Phys. Rev. Lett.* Vol. 72, 1994, p.2585
- [121] P. Kringhøj, A.N. Larsen, and S.Y. Shirayev, *Phys. Rev. Lett.* Vol. 76, 1996, p.3372
- [122] M. Onishi, H. Miura, *Trans. JIM* Vol. 18, 1977, p.107
- [123] S.W. Baker, G.R. Purdy, *Acta Mater.*, Vol. 46, 1998, p.511
- [124] E. Nes, *Metal Science*. Vol. 13(3/4), 1979, p.211
- [125] C.R. Hutchinson, P.T. Loo, T.J. Bastow, A.J. Hill and J. da Costa Teixeira., *Acta Mater.*, Vol. 57, 2009, p.5645

- [126] V.V. Sagaradze, V.A. Shabashov, T.M. Lapina, N.L. Pecherkina, and V.P. Pilyugin, *The Physics of Metals and Metallography*, Vol. 78(6), 1994, p. 619
- [127] Y. Ivanisenko, *Materials Science Forum*, Vol. 539 – 543, 2007, p.4681
- [128] F. Ju, Z. Xa, B.J. Diak, O.A. Ojo, W.D. MacDonald, M. Niewczas. *Magnesium Science and Technology – Automotive Lightweighting*. April 14-17, 2008, Cobo Centre. Detroit Michigan USA. Copyright 2007 SAE International
- [129] X. Zhao, X. Lin, J. Chen, L. Xue, W. Huang. *Mater. Sci. Eng. A*, Vol. 504, 2009, p.129
- [130] J.D. Embury, A. Deschamps, Y. Brechet, *Scripta Mater.*, Vol. 49, 2003, p.927
- [131] D. Shahriari, M.H. Sadeghi, A. Akbarzadeh, M. Cheraghzadeh, *Int. J. Adv. Manuf. Technol.*, Vol. 45, 2009, p.841
- [132] B. Radhakrishnan, R.G. Thompson, *Proceedings of the 2nd Int. Conf. on Trends in Welding Research*, 1989, p.637
- [133] J. Li, J. Wang, G. Yang, *Journal of Crystal Growth*, Vol. 311, 2009, p.1217
- [134] O.A. Ojo, N.L. Richards, M.C. Chaturvedi, *Scripta Mater.*, Vol. 51, 2004, p.141
- [135] M. Hillert, *Scripta Metall.*, Vol. 17, 1983, p.237
- [136] C.A. Handwerker, J.W. Cahn, D.N. Yoon, J.E. Blendell, in: M. A. Dayananda, G. E. Murch (Eds), *Diffusion in Solids: Recent Developments*, The Metallurgical Society, 1985, p. 275

- [137] J.W. Matthews, in: F.R.N. Nabarro (Ed), Dislocations in Solids, vol 2. Amsterdam: North Holland, 1979.
- [138] Y. Brechet, G.R. Purdy, Scripta Metall., Vol. 22, 1988, p.1629
- [139] W. Lin, J.C. Lippold, W.A. Baeslack III, Weld J., Vol. 72, 1993, p.135s
- [140] V.P. Demyantsevich, Weld. Prod., Vol. 14, 1967, p.1
- [141] Y. Lu, M. Li, W. Huang, H. Jiang, Materials Characterization, Vol. 54, 2005, p.423
- [142] D. Zhang, B. Yang, J. Zhang, Y. Zhang, B. Xiong, Trans. Nonferrous Met. Soc. China, Vol. 15, 2005, p.1125
- [143] C. Mary, M. Jahazi, Advanced Materials Research, Vol. 15-17, 2006, p.357
- [144] E. Glasman, R. Goshen, B. Harel, A. Neboshchik, E. Hodos, Aluminium Extrusion, Vol. 2(5), 1997, p.24
- [145] S. Swaminathan, K. Oh-Ishi, A.P. Zhilyaev, C.B. Fuller, B. London, M.W. Mahoney, T.R. Mcnelley, Metall. Mater. Trans. A, Vol. 41A, 2010, p.631
- [146] M.L. Kronberg, F.H. Wilson, Metall. Trans. AIME, Vol. 185, 1949, p.501